

---

**STUDYING MARTIAN DUST DEVILS  
BY APPLYING PATTERN RECOGNITION ALGORITHMS  
TO MULTI-MISSION CAMERA IMAGES**

---

INAUGURAL-DISSERTATION  
ZUR  
ERLANGUNG DES DOKTORGRADES  
DER MATHEMATISCH-NATURWISSENSCHAFTLICHEN FAKULTÄT  
DER UNIVERSITÄT ZU KÖLN

VORGELEGT VON  
**CHRISTINA STANZEL**  
AUS OSTFILDERN

KÖLN 2007

Berichtersteller: Priv.-Doz. Dr. Martin Pätzold  
Prof. Dr. Michael Kerschgens

Tag der mündlichen Prüfung: 29.10.2007

# Abstract

A pattern recognition and classification software was developed to detect dust devils automatically in surface images from Mars. The amount of images taken by spacecraft orbiting Mars is increasing continuously and the expenditure of time is too high to search every image for spatially and temporally highly variable features like dust devils. The pattern recognition method was therefore used to conduct a completely new kind of search for dust devils. Images from the three different Mars missions VIKING, MARS GLOBAL SURVEYOR and MARS EXPRESS can be processed and for the first time automatically scanned for the desired objects. VIKING images including dust devils were used as the database to filter unique dust devil features and the derived parameters built the feature vector. Various classification methods have been tested resulting in a two-layer perceptron (neural network) as the best classifier. Necessary adjustments and increments complete the software so that it can be applied to MARS GLOBAL SURVEYOR Mars Orbiter Camera (MOC), MARS EXPRESS High Resolution Stereo Camera (HRSC) and probably coming images from future missions.

It was shown that the standard dust devil is filtered and correctly classified. The two main features, the bright spot representing the dust column and the shadow, must be filterable from the background. Crater rims and hills are the most false-positive objects.

Three regions, Amazonis Planitia, Syria Planum and Chryse Planitia have been searched for dust devils by applying the software to all HRSC images available for these areas. Together with images where it was known before that dust devils are included, a total of 205 dust devils were analysed. A detailed statistics was prepared listing their diameters and heights, and for the first time the forward speeds of dust devils. The time of day, the season and the locations are noted as well.

The mean diameter is 230 m, the height is 660 m on average. They occur from late morning to late afternoon following the daily insolation. Most dust devils have been observed in spring and summer of the respective hemisphere, but formation in autumn and especially in winter was also seen. Dust devils move with the ambient wind, even at high speeds, which were formerly thought to be the reason that dust devil occurrence is suppressed. The computed speeds can be used as an indirect measurement of the near-surface wind speeds. Dust devils evolve wherever the atmospheric conditions are suitable and are not limited to certain regions or altitudes. A preference for dust devil activity can be seen in the 50° to 60°S latitude range due to the ascending branch of the Hadley circulation. The high frequency of dust devils in the Amazonis Planitia region that was observed before can not be verified so far. The southern part of Chryse Planitia seems to be a region favourably for dust devil formation.

The lifetimes of dust devils are a few minutes but increase with larger sizes and were measured up to 30 min. All derived characteristics were used to compute the dust lifting rates by a typical HRSC dust devil, which resulted in most reliable values between  $9.39 \times 10^{-4}$  to  $2.35 \times 10^{-1}$  kg/m<sup>2</sup>/a. This suggests a significant contribution of dust devils to the dust cycle on Mars. A comparison between dust devils analysed by the rover SPIRIT and those detected by HRSC revealed that most results complement each other suggesting that future dust devil studies should be performed with both methods, from the surface with a lander and with orbiter images.



# Kurzzusammenfassung

Eine Mustererkennungs- und Klassifikationssoftware wurde entwickelt, um Staubteufel automatisch in Bildern der Marsoberfläche zu detektieren. Da die Quantität an Bildern, die Raumsonden aus dem Orbit von Mars aufnehmen, stetig wächst, ist der Zeitaufwand viel zu hoch, um jedes Bild nach räumlich und zeitlich sehr variablen Objekten wie Staubteufeln zu durchsuchen. Aus diesem Grund wurde die Methode der Mustererkennung benutzt, um eine völlig neue Art der Suche nach Staubteufeln durchzuführen. Bilder der drei Marsmissionen VIKING, MARS GLOBAL SURVEYOR and MARS EXPRESS können prozessiert und erstmals automatisch nach den gewünschten Objekten durchsucht werden. VIKING Bilder, die Staubteufel enthalten, wurden als Datenbasis benutzt, um eindeutige Staubteufelmerkmale zu extrahieren und die erhaltenen Parameter bildeten den Merkmalsvektor. Verschiedene Klassifikationsmethoden wurden getestet und ein zweischichtiges Perzeptron (neuronales Netz) erzielte die besten Ergebnisse als Klassifikator. Notwendige Anpassungen und Erweiterungen komplettieren die Software, so dass sie auch auf MARS GLOBAL SURVEYOR Mars Orbiter Camera (MOC), MARS EXPRESS High Resolution Stereo Camera (HRSC) und eventuell noch folgende Bilder zukünftiger Missionen angewendet werden kann.

Es konnte gezeigt werden, dass der Standard-Staubteufel gefiltert und korrekt klassifiziert wird. Die zwei Hauptmerkmale, der helle Fleck, der die Staubsäule darstellt, und der Schatten, müssen aus dem Bildhintergrund herausgefiltert werden können. Kraterränder und Hügel stellen die Objekte dar, die am häufigsten als Staubteufel missklassifiziert werden.

Die drei Regionen, Amazonis Planitia, Syria Planum und Chryse Planitia, wurden nach Staubteufeln durchsucht, indem die Software auf alle HRSC Bilder angewendet wurde, die diese Gebiete abdecken. Insgesamt wurden 205 Staubteufel analysiert, inklusive Staubteufel aus Bildern, von denen schon vorher bekannt war, dass sie welche beinhalten. Eine detaillierte Statistik wurde erstellt, die Durchmesser und Höhen beinhaltet, und ebenso zum ersten Mal die Vorwärtsgeschwindigkeit von Staubteufeln. Die Tageszeit, Jahreszeit und Ort der Staubteufelentdeckungen sind ebenfalls erfasst.

Der mittlere Durchmesser beträgt 230 m, die Höhe ist im Mittel 660 m. Das Staubteufel-Vorkommen richtet sich nach der täglichen Sonneneinstrahlung und beginnt am späten Vormittag und reicht bis zum späten Nachmittag. Die meisten wurden im Frühling und Sommer der jeweiligen Hemisphäre beobachtet, aber ihre Entstehung wurde ebenso im Herbst und speziell auch im Winter gesehen. Staubteufel bewegen sich mit dem Umgebungswind vorwärts, sogar bei hohen Windgeschwindigkeiten, was früher als Hinderungsgrund verstanden wurde, dass Staubteufel sich überhaupt bilden können. Die berechneten Staubteufel-Geschwindigkeiten können als indirekte Messungen der bodennahen Windgeschwindigkeiten gesehen werden. Staubteufel entwickeln sich, wo immer die atmosphärischen Bedingungen günstig sind, und beschränken sich nicht auf bestimmte Gebiete oder Höhenlagen. Ein Vorzugsgebiet für Staubteufelaktivität scheint es allerdings zwischen 50° und 60°S Breite aufgrund des aufsteigenden Astes der Hadley-Zirkulation zu geben. Das zuvor beobachtete häufige Vorkommen von Staubteufeln in Amazonis Planitia konnte bis jetzt nicht bestätigt werden. Der südliche Teil von Chryse Planitia scheint eine Region zu sein, die sich vorteilhaft auf die Entstehung von Staubteufeln auswirkt.

Die Dauer von Staubteufeln beträgt nur ein paar Minuten, wächst aber mit der Größe an und erreichte bis zu 30 min. Alle ermittelten Staubteufel-Merkmale wurden benutzt, um die Staubheberate eines typischen HRSC Staubteufels zu berechnen. Die verlässlichsten Werte ergaben  $9.39 \times 10^{-4}$  bis  $2.35 \times 10^{-1}$  kg/m<sup>2</sup>/a. Dies weist auf einen deutlichen Beitrag zum Staub-Zyklus auf dem Mars durch Staubteufel hin.

Ein Vergleich zwischen Staubteufeln, die vom Rover SPIRIT fotografiert wurden, und denen, die von HRSC gesehen wurden, ergab, dass sich die meisten Ergebnisse ergänzen. Dies impliziert für die Zukunft, dass Staubteufel am besten mit beiden Methoden untersucht werden, von der Oberfläche aus mit einem Lander und mit Bildern aus dem Orbit.

---

# Contents

---

<b>1</b>	<b>Introduction</b>	<b>1</b>
<b>2</b>	<b>Dust Devils</b>	<b>5</b>
2.1	Dust Devil Formation and General Characteristics . . . . .	5
2.1.1	Observations . . . . .	5
2.1.2	Models . . . . .	9
2.2	Dust Devils on Earth . . . . .	12
2.3	Dust Devils on Mars . . . . .	14
<b>3</b>	<b>Missions to Mars</b>	<b>21</b>
3.1	VIKING . . . . .	21
3.2	MARS GLOBAL SURVEYOR . . . . .	22
3.3	MARS EXPRESS . . . . .	23
<b>4</b>	<b>The High Resolution Stereo Camera</b>	<b>25</b>
4.1	Imaging Technique . . . . .	25
4.2	Scientific Objectives . . . . .	26
4.3	The Analysis of Dust Devils in HRSC Images . . . . .	26
<b>5</b>	<b>Pattern Recognition and Classification</b>	<b>29</b>
5.1	Pattern Recognition Systems . . . . .	30

5.2	The Design Cycle . . . . .	31
5.3	Characteristics in Pattern Recognition . . . . .	32
<b>6</b>	<b>Pattern Recognition Algorithms for Martian Dust Devils</b>	<b>35</b>
6.1	Dust Devils in VIKING Images . . . . .	35
6.1.1	The Search for Brightness Maxima . . . . .	37
6.1.2	The Hoshen-Kopelman Algorithm . . . . .	37
6.1.3	Geometry Parameters . . . . .	40
6.1.4	The Search for the Dust Devil Shadow . . . . .	43
6.1.5	The Structure of the Results . . . . .	45
6.2	Adjustment to HRSC Images . . . . .	47
6.2.1	General Configuration . . . . .	47
6.2.2	Illumination Conditions . . . . .	48
6.3	Adjustment to MOC Images . . . . .	50
<b>7</b>	<b>Classification of Detected Patterns</b>	<b>53</b>
7.1	The LNKnet Library . . . . .	53
7.2	Classification of the VIKING Dataset . . . . .	54
7.2.1	Classification of the Dust Devil's Bright Spot . . . . .	55
7.2.1.1	Separation of Data . . . . .	55
7.2.1.2	Normalisation and Feature Selection . . . . .	55
7.2.1.3	Classifier Testing . . . . .	58
7.2.2	Classification of the Dust Devil's Shadow . . . . .	67
7.2.3	Results of the Pattern Classification . . . . .	70
7.3	Classification of the HRSC Dataset . . . . .	72
7.3.1	Adjustments . . . . .	72
7.3.2	Results . . . . .	75
7.4	Classification of the MOC Dataset . . . . .	84
<b>8</b>	<b>Dust Devils: the Scientific Investigation</b>	<b>89</b>
8.1	Spatial and Temporal Distribution . . . . .	89
8.2	Dimensions . . . . .	93

---

8.3	Traverse Velocity . . . . .	94
8.4	Dust Devil Tracks and Lifetime . . . . .	99
8.5	Dust Lifting Rates of Dust Devils . . . . .	102
8.6	Dust Storms and Dust Devils . . . . .	105
8.7	Comparison with SPIRIT Dust Devils . . . . .	107
8.8	Joint MEX-MER Observations . . . . .	110
<b>9</b>	<b>Discussion and Outlook</b>	<b>113</b>
<b>A</b>	<b>Image Identifiers</b>	<b>117</b>
A.1	VIKING . . . . .	117
A.2	MARS GLOBAL SURVEYOR . . . . .	117
A.3	MARS EXPRESS . . . . .	118
<b>B</b>	<b>Hoshen-Kopelman Algorithm</b>	<b>119</b>
<b>C</b>	<b>Classification Results</b>	<b>121</b>
C.1	VIKING Image Analyses . . . . .	121
C.2	HRSC Image Analyses . . . . .	123
<b>D</b>	<b>HRSC Dust Devil Characteristics</b>	<b>127</b>
	<b>Bibliography</b>	<b>133</b>



---

## List of Figures

---

2.1	Wind Speed Structure within a Dust Devil . . . . .	6
2.2	Rankine Vortex Tangential Velocity Structure . . . . .	7
2.3	Terrestrial Dust Devil with Dust Skirt . . . . .	8
2.4	Vertical Slices through Dust Devil Simulations . . . . .	10
2.5	Desert Dust Devil and Dust Devil near Celle, Germany . . . . .	13
2.6	Dust Devil Tracks . . . . .	14
2.7	VIKING Dust Devils . . . . .	17
2.8	SPIRIT Dust Devil I . . . . .	18
2.9	MARS PATHFINDER Dust Devil . . . . .	19
4.1	HRSC Imaging Technique . . . . .	26
4.2	The Parallax Principle . . . . .	27
5.1	The Pattern Recognition System . . . . .	30
6.1	Different Dust Devil Appearances . . . . .	36
6.2	Black and White Dust Devil Image . . . . .	38
6.3	Cluster Size Distribution . . . . .	39
6.4	Best-fit Ellipse . . . . .	40
6.5	Geometry Parameters . . . . .	41
6.6	Histograms of Dust Devil Parameters . . . . .	42

6.7	Shadow Detection . . . . .	43
6.8	Structure of Results . . . . .	45
6.9	Quick-look Plots . . . . .	46
6.10	HRSC Image Strip . . . . .	47
6.11	Illumination Conditions . . . . .	49
7.1	LNKnet Classifier Overview . . . . .	54
7.2	Training File . . . . .	56
7.3	Feature Selection . . . . .	57
7.4	Multi-layer Perceptron . . . . .	58
7.5	MLP Results I . . . . .	59
7.6	MLP Results II . . . . .	60
7.7	MLP Plots . . . . .	61
7.8	KNN Results . . . . .	63
7.9	KNN Plot . . . . .	63
7.10	Committee Results . . . . .	65
7.11	Committee-Gaussian Plots . . . . .	66
7.12	MLP Shadow Results . . . . .	68
7.13	MLP Shadow Plots . . . . .	69
7.14	VIKING Classification Results . . . . .	70
7.15	Shadow Decision Region Plot . . . . .	73
7.16	Shadow Classifier Regions . . . . .	74
7.17	Classification Results Terra Cimmeria Dust Devils . . . . .	76
7.18	Terra Cimmeria Dust Devils . . . . .	76
7.19	Syria Planum Dust Devils . . . . .	77
7.20	Dust Devil and Craters in Chryse Planitia . . . . .	80
7.21	Comparison of HRSC and VIKING Images . . . . .	83
7.22	MOC NA and WA Images . . . . .	87
8.1	Dust Devil Locations . . . . .	90
8.2	SRC Dust Devil . . . . .	93
8.3	Wind Speed Profile . . . . .	95

---

8.4	Stereo Images Thaumasia Planum . . . . .	96
8.5	Arsia Mons Streaks . . . . .	99
8.6	Dust Devils Creating Streaks . . . . .	101
8.7	Dust Devils with Long Shadows . . . . .	102
8.8	Dust Storms . . . . .	106
8.9	SPIRIT Dust Devil II . . . . .	108
B.1	Hoshen-Kopelman Algorithm . . . . .	120



---

## List of Tables

---

7.1	Classification Results of the VIKING Database I . . . . .	71
7.2	Classification Results of HRSC Images . . . . .	79
7.3	Summary of Analysed Regions . . . . .	82
7.4	Classification Results of MOC NA Images . . . . .	85
7.5	Classification Results of MOC WA Images . . . . .	86
8.1	Speeds with and without Parallax . . . . .	97
8.2	SRC Dust Devil Tracks . . . . .	100
8.3	Dust Lifting Rates . . . . .	103
8.4	Comparison of HRSC and SPIRIT Dust Devils . . . . .	109
C.1	Classification Results of the VIKING Database II . . . . .	122
C.2	Amazonis Planitia Orbits I . . . . .	123
C.3	Amazonis Planitia Orbits II . . . . .	124
C.4	Syria Planum Orbits . . . . .	125
C.5	Chryse Planitia Orbits . . . . .	126
D.1	HRSC Dust Devil Characteristics . . . . .	132



---

## INTRODUCTION

---

The atmosphere of a planet is an important factor for possible life and for the planet itself and its development. On Earth, the atmosphere is quite well understood: longtime observations and measurements were conducted, models have been developed and are used for weather forecasting (the most influential aspect of the atmosphere on creatures) and several meteorological satellites observe almost globally our planet and its atmosphere. Such an amount of possibilities to measure data or to follow changes is not possible when exploring other planets in space.

Scientific instruments on board of spacecraft are chosen in such a way as to provide the largest usefulness and to complement each other. For a planet like Mars (consisting of a solid body and an atmosphere) imaging instruments, spectrometers, radars and particle analysers are necessary to investigate the surface and the atmosphere. Mars belongs to the so-called terrestrial planets, whereto Mercury and Venus belong as well. These planets are similar to Earth in their constitution: they consist of solid material, have a similar mass, density and diameter, and have (beside Mercury) also an atmosphere.

People are interested in Mars for a long time, because it is the 'smaller brother' of the Earth. The first spacecraft to Mars were launched in the early sixties, but most of them crashed or did not work to send data back to Earth. The first successful mission was MARINER 4 flying by Mars on July 14 and 15, 1965. From an altitude of 9800 km above the surface 22 images were taken revealing a Moon-like cratered terrain. MARINER 9 reached Mars on November 14, 1971, and surpassed all expectations, transmitting over 7000 images by photographing 80% of the Martian surface. These images showed rather the typical surface character of Mars, including volcanoes, canyons and riverbeds. In 1975, VIKING 1 and 2, each carrying a lander, were launched and reached Mars successfully. For the first time, samples of the soil could be analysed and images from the surface were taken. The first Martian dust devils were seen in these VIKING images [*Thomas and Gierasch, 1985*].

After an absence of about 20 years at Mars, MARS GLOBAL SURVEYOR arrived in September 12, 1997, and has returned more scientific data than all other previous missions combined. The laser altimeter gave the first three-dimensional views of the topography of Mars. Also analyses of the gravity, magnetic fields, thermal properties and surface composition were possible. The next great step was a lander, named MARS PATHFINDER, together with the rover SOJOURNER, sent to Mars in 1996. MARS PATHFINDER transmitted many soil samples as well as meteorological data. Atmospheric vortices assumed to be dust devils have been seen in the temperature and pressure data of the lander [*Schofield et al.*, 1997] and dust devils have been imaged by the camera [*Metzger et al.*, 1999; *Ferri et al.*, 2003].

MARS EXPRESS is in orbit around Mars since December 25, 2003. Along with a particle analyser, several spectrometers, a radar and a radio science experiment, a new imaging technique arrived at the planet. The High Resolution Stereo Camera (HRSC) is able to image the planet with stereo and colour channels. It is intended to map 100% of the surface with at least a resolution of 100 m/pixel, and 1% at about 2 m/pixel with the Super-Resolution Channel (SRC). The resolution and the amount of images improved with the missions during the decades of Mars exploration. While MARINER 9 had the best resolution between 100 and 300 m/pixel imaging 3% of the surface, VIKING already imaged 95% of the Martian surface with 200 m/pixel and was capable to take few images below 10 m/pixel resolution. MARS GLOBAL SURVEYOR provided a range of 1.4 to 10 m/pixel with the Narrow Angle (NA) Camera, and a global coverage at 200 m/pixel resolution with the Wide Angle (WA) Camera. HRSC now fills the gap to provide a high surface coverage of the planet between 10 to 100 m/pixel resolution, with the possibility to image specific targets with SRC at 2.3 m/pixel resolution.

Future missions are planned to be launched for Mars in the next decades, including preparations for further landers and even human exploration. Mars as an Earth-like planet seems to be the best choice to start human exploration in our Solar System. Detailed knowledge of the atmosphere and its impact on techniques and creatures are important for long-term missions. Dust devils are a fundamental part of the Martian atmosphere.

Dust devils are thermally driven atmospheric vortices that are filled with loose material such as sand and dust [*Sinclair*, 1969]. The particles are raised from the surface by the low pressure core within the dust devil, which was found to be a very effective way to move even fine-grained particles [*Greeley et al.*, 2003; *Ferri et al.*, 2003; *Balme and Hagermann*, 2006]. Dust devils are visible by their dust-filled columns. They are seen as bright features illuminated by the Sun and emphasised by an elongated dark shadow. The existence of such atmospheric vortices was predicted for Mars [*Ryan*, 1964; *Neubauer*, 1966; *Gierasch and Goody*, 1973] before they were first detected in VIKING images [*Thomas and Gierasch*, 1985]. Both VIKING orbiters imaged dust devils, and data recorded by the two VIKING landers suggested the passage of several vortices that were likely dust devils [*Ryan and Lucich*, 1983; *Ringrose et al.*, 2003]. Dust devils on Earth and Mars are supposed to form most likely in spring and summer at noon and early afternoon [*Sinclair*, 1969; *Wennmacher et al.*, 1996]. Their size ranged from a few to hundreds of metres in diameter on Earth and Mars, with heights between a few metres (Earth and Mars) and several kilometres (Mars) determined in former studies [*Thomas and Gierasch*, 1985; *Cantor and Malin*, 2003; *Biener et al.*, 2002]. Dust devils may

---

be responsible for the generation of local dust storms [Ryan *et al.*, 1981].

The variety in sizes, the numerous occurrences and the effective dust-lifting ability suggest that dust devils play an important role in the thermal structure of the atmospheric boundary layer of Mars [Zurek *et al.*, 1992]. In addition, the dust column is electrically charged and it is not clearly known what the impacts of these phenomena will be on more complicated techniques and equipments of future lander missions. Dust devils contribute to the Martian weather by dust entrainment, which influences the atmosphere's temperature and leads to surface albedo changes by removing thin layers of dust [Malin and Edgett, 2001]. Dust devil studies on Earth [Ives, 1947; Ryan, 1972; Snow and McClelland, 1990; Metzger, 2003] have been conducted to better understand their dynamics and impact on the atmosphere and climate, especially to then apply the knowledge to Mars. Most investigations concentrated on specific study areas on Mars, extrapolating the spatial and temporal distribution of dust devils to larger regions. Consequently, the full extent of the contribution to the dust budget is poorly known. Additionally, models have been developed and compared [Kanak, 2006] to understand when, where, and under which circumstances dust devil-like vortices may form. Laboratory work [Greeley *et al.*, 2003; 2004; Neakrase *et al.*, 2006] has been conducted to simulate dust flux within dust devils, the directions of movement, and particle lifting under Martian conditions to understand the basic dynamics and characteristics of dust devils. The nearly global coverage of Mars by HRSC will shed light on many of these aspects of dust devils. We will investigate and possibly verify or disprove the temporal and spatial distribution of dust devils as well as their sizes. The dust entrainment will be studied, depending on their lifetime, tracks and motion. The findings will be related to in-situ detections by landers.

The enormous amount of images taken just by the three missions VIKING, MARS GLOBAL SURVEYOR and MARS EXPRESS (more than 300 000 images) shows the necessity of developing a software which searches automatically for dust devils in Martian images. The time spent for searching dust devils will be reduced a lot, when only preselected features must be checked if they are dust devils or not. Pattern recognition and classification seem to be the appropriate methods for searching dust devils, because they are recognisable by a bright spot, which is the dust column reflecting the sun light, and an elongated dark shadow in Martian images. The method of using pattern recognition techniques became more popular in the last years but beside our study only one other work is known which tries to search for dust devils by applying pattern recognition tools [Gibbons *et al.*, 2005].

Chapter 2 introduces dust devils on Earth and Mars and the differences in detail. The three missions to Mars in whose images dust devils were seen and which are used in this work are presented in Chapter 3. Chapter 4 deals with the High Resolution Stereo Camera on board of MARS EXPRESS and how dust devils can be studied using different imaging channels. Chapter 5 introduces pattern recognition and classification. The pattern recognition algorithms and methods developed in this study are presented in Chapter 6, starting with the VIKING database and explaining necessary adjustments to HRSC and MOC (Mars Orbiter Camera on board of MARS GLOBAL SURVEYOR) images. A classification library as well as some of the tested classifiers and the finally used one are described in Chapter 7. The pattern recognition results of images from the three missions VIKING, MARS EXPRESS and MARS GLOBAL SURVEYOR are presented here, too. Chapter 8 deals with the scientific results of the analyses

of HRSC dust devils and the new insights into dust devils characteristics on Mars. Chapter 9 closes with an overall discussion and outlook.

---

## DUST DEVILS

---

In the first section the principles of dust devil formation and their general characteristics are reviewed as they may apply for Earth and Mars, although most of the observations rely on Earth investigations. The second and third sections highlight the differences of dust devils on both planets.

### 2.1 Dust Devil Formation and General Characteristics

#### 2.1.1 Observations

Dust devils form and evolve primarily during unstable temperature stratifications in the surface boundary layer and are not necessarily associated with the highest air temperature. *Ryan* [1972] found that the temperature lapse rate at altitudes between 0.3 and 10 m above the ground is the most important factor for dust devil development, combined with vertical vorticity<sup>1</sup> which provides the initial rotation. *Sinclair* [1969] also showed that a superadiabatic layer leads to an increase in dust devil occurrence. With increasing instability, larger-diameter dust devils are formed as well. The maximum of dust devil activity occurs 2-3 hours before the daily maximum air temperature. However, high surface air temperatures are the second important component for dust devil formation. In the afternoon after the ground has heated up and warmed the air immediately above the surface, warm air rises and horizontal pressure variations are created. Due to the low pressure, particles like sand and dust are lifted and make the air column visible, looking like an inverse cone.

---

<sup>1</sup>Vorticity is a measure for the rotation in a flow field (wind velocity)

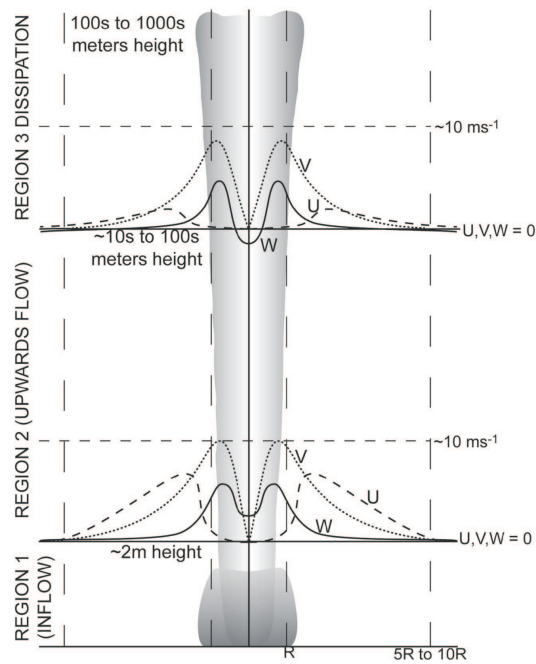


**Figure 2.1:** Generalisation of wind speeds within a dust devil.  $R$  is the radius of the dust column,  $U$ ,  $V$  and  $W$  are the radial, tangential and vertical wind speeds, respectively. Maximum speeds are given as  $\sim 10$  m/s, typical of many dust devils, but can be up to 25 m/s. Adapted from Balme and Greeley [2006].

Carroll and Ryan [1970] showed that atmospheric properties responsible for dust devil initiation may be different from those contributing to the maintenance. The energy for the dust devil is coming from the warm boundary layer air which is continually soaked by the vortex. The raised particles within the dust devil heat additionally by absorbing radiation and strengthen the atmospheric vortex. Thereby, a dust devil can keep itself alive for quite a long time.

Balme and Hagermann [2006] gave evidence of how striking the ‘ $\Delta P$ ’ effect in dust devils is. ‘ $\Delta P$ ’ represents the horizontal pressure difference between the low-pressure centre of the dust devils and the ambient conditions. The lifting effect is greater for smaller particles. The rates of change in pressure seem also to play an important role, suggesting that small dust devils travelling at greatest speeds with a high negative pressure excursion are the most effective dust lifting vortices. This may explain why dust devils consist mostly of smaller particles ( $< 100 \mu\text{m}$ ). If there is no loose surface material available or the soil is only covered with rocks and coarser particles, it is likely that no dust devils will be observed because they are transparent.

The removal of dust can be seen by tracks which are left by dust devils moving forward and lifting dust. This removal leads to an albedo change of the dust devil’s path compared to the surrounding area. The path appears mostly darker because the overlying brighter sand and dust have been removed. The change of albedo seems to be dependent on the thickness of the removed layer.

A source of vorticity seems to be a supplementary element for dust devil formation, although Ryan [1972] rules out vorticity as the only initiator. He saw no correlation between envi-

ronmental vorticity and dust devil frequency and diameter. *Sinclair* [1969] suggests local or natural obstructions as a source of vorticity. He found many dust devils in the lee of small mountains, which are maybe the reasons for vortices embedded in the background flow initialising dust devil activity together with an unstable stratification and strong insolation. Sloping terrains also favour dust devil initiation as well as strong horizontal thermal gradients induced by different types of terrain [*Sinclair*, 1969].

Strong winds may suppress dust devil development because of the vertical mixing in the boundary layer which weakens the superadiabatic lapse rate. Driven by breezes, the vortex moves across the surface, mostly at a few metres per second, and tends to move in the direction of the prevailing wind. They slope with height in the direction of movement because of the wind shear. If there is little or no wind, the topography controls in many cases the trajectory of dust devils [*Ives*, 1947].

Some cases are reported on Earth where dust devils were almost stationary, lasting for several hours [*Ives*, 1947]. Theoretically, a dust devil can exist as long as the energy, the warm surface air, is available and it remains in a favourable environment with loose material. Dust devils tend to last longer with increasing size. *Ives* [1947] gives an estimation of one hour duration for each 300 m of height.

Summer and spring are the preferred seasons for high dust devil occurrence, directly correlated with the stronger insolation in these months and the higher probability of unstable lapse rates. The insolation and the unstable stratification are also the reasons why the daily maximum of dust devil activity is found in the noon and afternoon times. These circumstances do not necessarily exhibit dust devil occurrence in autumn or winter or at other times of the day. The main conditions for dust devil formation, unstable stratifications, sources of vorticity and loose material, can be available at other times as well.

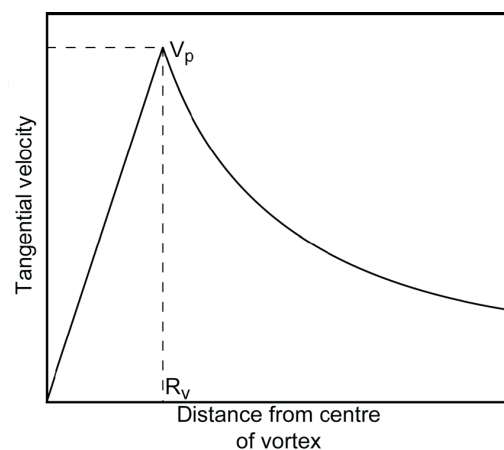


**Figure 2.2:** Rankine vortex tangential velocity structure. Tangential velocity rises as a linear function of radius within the vortex, and decreases as an inverse function of radius outside of the vortex. Tangential velocity reaches a peak  $V_p$  at radius  $R_v$ . Adapted from *Balme and Greeley* [2006].

*Balme and Greeley* [2006] gave a review of the characteristics of dust devils on Earth and Mars presented in dust devil papers in the last decades. The horizontal speed within dust devils has values up to 25 m/s, the vertical wind speed up to 10 m/s (Figure 2.1). Larger dust devils have greater rotational wind speeds and they tend to have also greater vertical

winds [Ryan and Carroll, 1970]. The tangential speed has a maximum at the radius of the dust-laden region and a minimum at the central core and approximates therefore a Rankine vortex (Figure 2.2).

This corresponds with the dust-free core which were seen in most of the dust devils in the studies of Sinclair [1973] and Balme *et al.* [2003a]. This is due to the dynamics within a dust devil, where the inflow occurs in front of and behind the dust devil and swirls up at the radius of the dust devil responsible for the high rotational speeds. A downdraft is established in the core, but only at a higher altitude within the dust devil, whereas there is a vertical velocity of a few metres per second near the ground. This suggests a stagnation point within a dust devil [Balme and Greeley, 2006].

Due to contact, friction and separation between grains within a dust devil, dust devils have electrostatic fields up to 20 kV/m [Farrell *et al.*, 2004]. This effect is known as the triboelectric effect. Farrell *et al.* [2004] explains why dust devils always seem to have negative electric fields: smaller particles tend to become negatively charged and because smaller particles are preferably moved upward compared to larger sand-sized particles, large negative gradients are measured within a dust devil.



**Figure 2.3:** A terrestrial dust devil with a dust skirt seen in Australia (© Inflow Images).

This electric field is driven by two processes: currents by charging grains and the increasing velocity difference because of varying-sized grains at early times [Farrell *et al.*, 2006b]. The growth of such an electric field in a dust devil is dependent on the grain sizes and the ambient atmospheric conductivity. Induced by the changing electric field, also magnetic emissions are measured from a dust devil [Farrell *et al.*, 2006a]. Since Martian dust devils can be much stronger, larger and dustier than their terrestrial analogues, it is assumed that the electric fields will have higher negative values.

The distribution of particles due to their size can also be seen by the ‘skirt’ as Greeley *et al.* [2003] has called it (Figure 2.3). Larger grains remain near the surface and build a dust cloud near the bottom of the dust column due to the centrifugal force which causes them to eject from the real vortex and return to the surface. The particles which go in suspension are dust-like particles [Greeley *et al.*, 2004].

## 2.1.2 Models

Models were often used to simulate convective patterns in the boundary layer, vertical vortices, however, which have formed in these simulations have not been mentioned explicitly. *Kanak* [2006] did a review of simulations of the turbulent convective boundary layer, not including simulations of individual vertical vortices. Hence, the ambient conditions which are responsible for dust devil-like vortex formation can be seen and retrieved from these simulations.

Surprisingly, no mean horizontal wind was necessary for the vortex formation in the terrestrial simulation of the convective boundary layer of *Kanak et al.* [2000]. First it was thought that some source of wind shear is required for vertical vortices to form. Vortices were identified at the vertices of the cellular convective patterns, seen at the lowest level of the simulations as well as at higher levels [*Kanak et al.*, 2000]. *Fiedler and Kanak* [2001] showed that tilting of horizontal vorticity above the surface into the vertical can be assumed as the source of vertical vorticity. *Kanak et al.* [2000] proposed another mechanism to obtain vertical vorticity in the absence of mean wind. Convective-cell circulations create azimuthal horizontal vorticity rings which are strongest near the updraught/downdraught intersections. Due to the inflow the vorticity rings may be advected toward the updraught regions. Here, also the gradients of vertical velocity are the largest [*Kanak et al.*, 2000].

The question if the simulated dust devil-like vortices are similar to real dust devils on Earth has been answered by *Kanak* [2005a]. The concurrence with dust devil observations is quite well, only the simulated pressure excursions are weaker than observed.

The features like diameter, wind speeds and pressure excursions of the simulated Martian vortices in the work of *Rafkin et al.* [2001] and *Michaels and Rafkin* [2004] are in very good agreement with Martian dust devils. One dust devil was tilted with height as it is seen in many observations. An ambient background wind profile was provided in *Rafkin et al.* [2001] as a source of vorticity, that might aid in the development of dust devils. In *Michaels and Rafkin* [2004] a background wind of 5 m/s was used for the simulations. The effect of this wind was seen in early times but the heating of the surface by insolation preponderated in the afternoon. Dust devils developed at the vertices of convective cell patterns like in the terrestrial simulations [*Kanak et al.*, 2000].

*Toigo et al.* [2003] get the same location of dust devil development in their study. They have added different wind profiles to analyse the effect of wind shear. Dust devils developed in the ‘no wind’ case and in the case with the ‘highest wind speed’ (Figure 2.4). Otherwise the wind shear had a delaying effect on the formation of dust devil-like vortices. *Toigo et al.* [2003] suggest as well that dust devil formation will not be prevented although vorticity is not present in the mean wind field. They support the idea of *Kanak et al.* [2000] that the development of dust devils appear primarily from the convergence of environmental vertical vorticity into the updraught regions. And this vorticity is generated from the tilting of horizontal vorticity into the vertical [*Toigo et al.*, 2003]. The dust devil characteristics of this simulation are also in agreement with Martian observations.

The previous discussed simulations are very complex and try to model the Martian boundary layer processes as closely as possible. *Kanak* [2005b] wanted to know which are the mini-

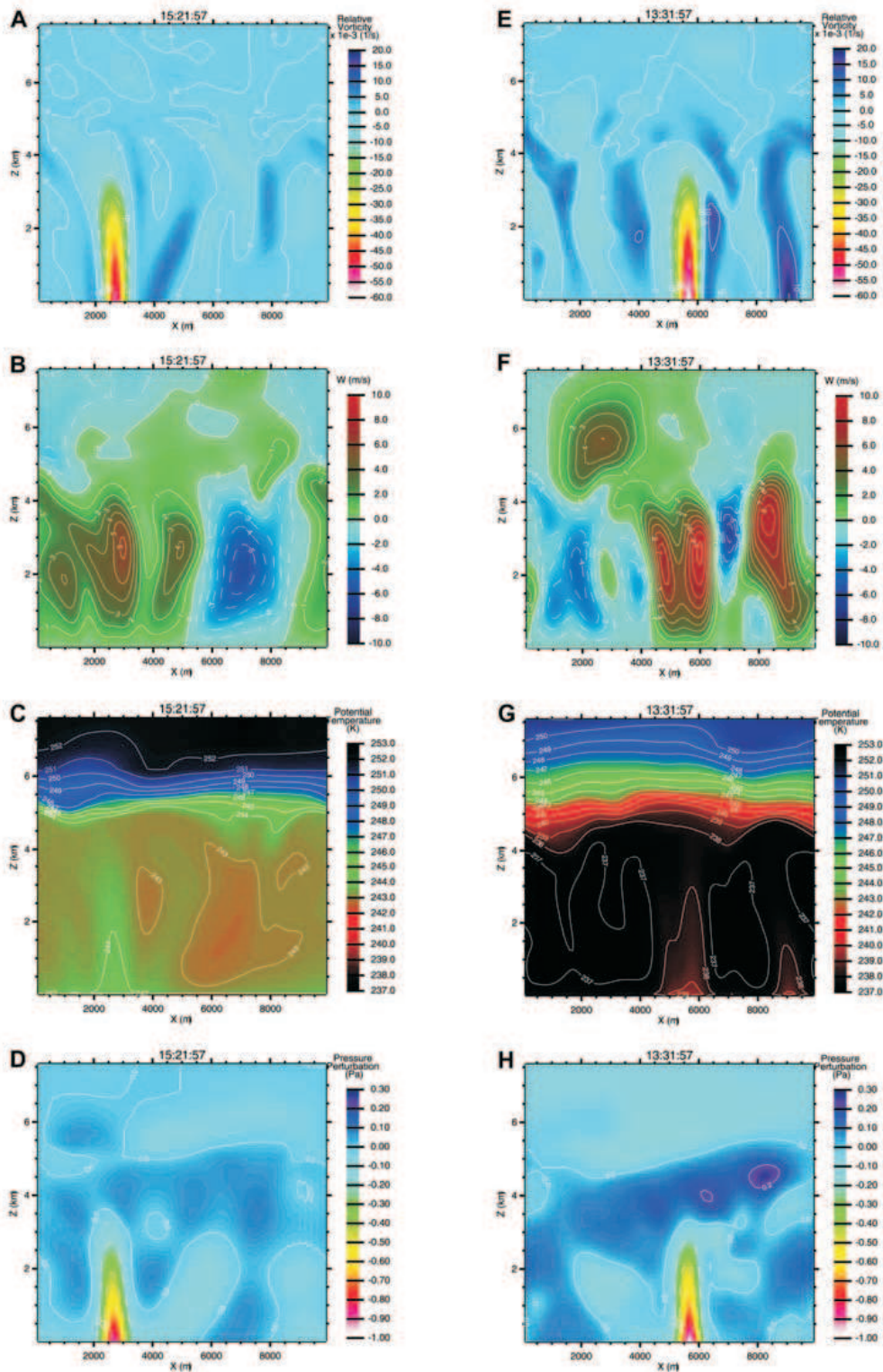


**Figure 2.4:** Vertical slices through the centre of the two dust devils seen in the simulations of Toigo et al. [2003]. The model domain size is 10 km ( $x$ -axis) by 7.5 km (left  $y$ -axis). Figures A-D refer to the no wind simulation, figures E-H refer to the high wind simulation. A and E: Vertical vorticity. The dust devils are seen as very large negative vorticity spikes. B and F: Vertical wind. The dust devils represent the locations of largest vertical velocity. C and G: Potential temperature. The dust devils stand out as large positive potential temperature differences from the background. D and H: Pressure perturbation (difference from background pressure). The dust devils are low-pressure cells. Adapted from Toigo et al. [2003].

imum dynamical and physical processes for the formation of Martian dust devils. It was shown that the absence of surface inhomogeneities and radiative processes and simpler parameterisations do not exclude dust devil formation. The solutions, however, were very sensitive to the initial thermal profile. Also in this case, dust devil parameters fit the observation values.

The review of *Kanak* [2006] shows, that in all simulations, independent of differences in the initial conditions and experimental designs, dust devil-like vortices developed. Necessary conditions seem to be convective patterns (due to insolation or unstable stratification) and vertical vorticity (mostly gained from tilted horizontal vorticity). Dust was not present in the simulations, therefore it is not known if the developed vortices are really dust devils, or just invisible dust devil-like vortices without any dust entrainment into the atmosphere.

In contrast to the models presented so far, which deal with the simulations of the convective boundary layer, *Rennó et al.* [1998] proposed a simple scaling theory for dust devils on Earth to estimate their potential intensity. Based on the assumption that dust devils are heat engines, they were able to develop a theory to calculate the pressure depression (intensity), wind velocity and diurnal variation. The heat input to a dust devil is the sensible heat flux, the output is in the form of thermal radiation by air parcels [*Rennó et al.*, 1998]. They conclude that the pressure drop from the radius to the core of the dust devil is proportional to the net heat input. The water vapour content is neglected since most of the heat input in a dust devil is sensible heat flux which underlines its character in contrast to tornadoes or waterspouts. Therefore, the radial pressure drop can be used as a degree of the dust devil intensity. The intensity depends as well on the thermal gradient from outside of the dust devil to the centre, which leads to the conclusion that dust devils are more likely to form where large horizontal thermal gradients occur.

To summarise, the intensity of a dust devil ( $\Delta p$ ) depends on the surface pressure, the vertical thermodynamic efficiency (pressure thickness of the convective layer or vertical temperature gradient), the dissipation of energy (friction), and the horizontal thermodynamic efficiency (horizontal temperature gradient) [*Rennó et al.*, 1998].

From this theory also the tangential velocity can be estimated assuming that a dust devil is cyclostrophically balanced. This derivation suggests that the wind speed around a dust devil does not explicitly depend on its size, but maybe indirectly through the horizontal thermodynamic efficiency. The radius depends on the thermodynamics and the initial angular momentum of the air parcels, which means higher wind speeds are responsible for larger dust devils. The theory is tested by using common values for surface temperature and pressure and parameters for dry air. The derived values of the model for the pressure excursion ( $\Delta p$ ), tangential ( $v$ ) and vertical velocity ( $w$ ) are in good agreement with observational data of dust devils on Earth.

*Rennó et al.* [2000] tested this scaling theory also for Martian dust devils using MARS PATHFINDER lander data. The observed lander data of pressure and wind speeds belonging to passages of potential dust devils are consistent with predictions of the model. Therefore the model gives simple explanations of general characteristics of both terrestrial and Martian dust devils, showing that the intensity of convective vortices is only a function of the thermodynamic properties of their environment [*Rennó et al.*, 2000].

## 2.2 Dust Devils on Earth

Preferable areas for dust devils on Earth are arid regions with strong insolation and where, of course, loose material is available. Given that, it is not surprising that most of the terrestrial dust devils are seen in desert plains (Figure 2.5a). Dust devil studies have been almost exclusively conducted in deserts to guarantee a high occurrence of these vortices for statistical purposes. If the atmospheric conditions are suitable, dust devils may also be seen in regions affected by civilisation (Figure 2.5b).

The diameters of terrestrial dust devils range between a few metres and 100 m. The majority have diameters between 1 and 15 m. The height is between a few metres and over 1 km. *Balme and Greeley* [2006] report from their review of several dust devil studies that about 50% of the dust devils are 3-50 m high. Also larger dust devils with heights over 2 km can be observed. The larger a dust devil is the longer its duration. They exist for some seconds up to 20 minutes, the majority have a duration of 1-4 minutes [*Sinclair*, 1969]. Observations were reported where dust devils lasted more than one hour [*Ives*, 1947].

Spring and summer seem to be the preferable seasons for high dust devil activity according to the atmospheric conditions which are necessary for dust devil development. Occurrence is not excluded in autumn and winter times, but less reported since most dust devil studies have been performed in summer times. The diurnal variation corresponds to the insolation and when superadiabatic lapse rates occur. Dust devil activity starts in the morning around 1000 to 1100 hours, peaks at 1300 to 1400 hours, and vanishes after 1600 to 1700 hours. This pattern of diurnal distribution is independent of the diameter size of dust devils but smaller dust devils tend to peak a little earlier than the larger ones [*Sinclair*, 1969]. The explanation is that it takes some time to establish a superadiabatic lapse rate through a broader layer of the atmosphere, and then it is possible that dust devils can extend their heights. Smaller dust devils have a higher frequency than larger ones. *Sinclair* [1969] reports that roughly 56% of the observed dust devils had medium sizes of 3-15 m in diameter. The mean activity is among 0.11 and 767.33 dust devils per day and square kilometre for different dust devil investigations [*Balme and Greeley*, 2006].

The general wind speed structure outside and within a dust devil is illustrated in Figure 2.1 (page 6). For terrestrial dust devils the horizontal wind speed is typically  $<25$  m/s, whereas the tangential speed component  $v$  can be up to 20 m/s, normally between 5-10 m/s, and the radial velocity  $u$  is almost zero within a dust devil. The vertical wind speed  $w$  is  $<10$  m/s.

Dust devils move forward with the ambient wind speed and have translational speeds of a few metres per second. *Snow and McClelland* [1990] reported an average speed of 4 m/s in their survey and suggest that dust devil speeds greater than about 11 m/s are due to measurement errors. *McGinnigle* [1966] state forward speeds of about 5 m/s for the observed dust devils all moving in the same direction, underlining the assumption of movement with the ambient wind.

Temperature excursions range from one to several Kelvins when comparing the temperature in the centre of dust devils (warmer) to the outside (colder). A difference of even 22 K was measured with a high sampling sonic anemometer (*Metzger* [1999] in *Balme and Greeley* [2006]). The peak pressure excursions measured in dust devils are normally a few hectopas-

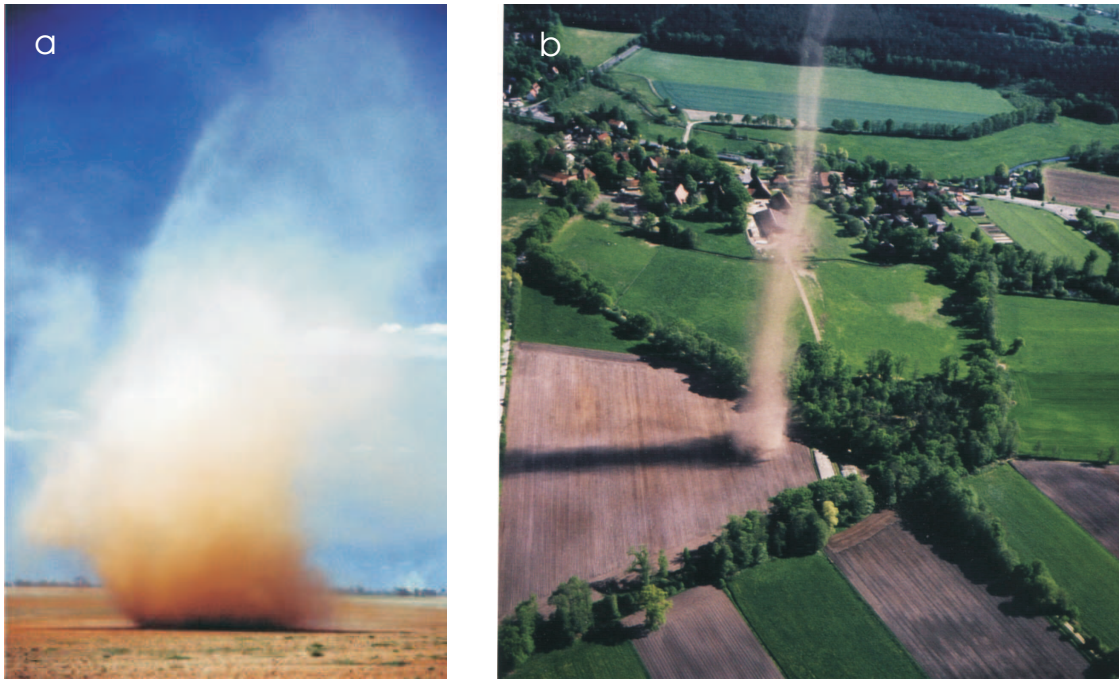


**Figure 2.5:** a) A broad desert dust devil in Australia. No clear defined column is seen (© Inflow Images). b) A terrestrial dust devil over an agricultural field near Celle, Germany. In the upper part of the dust column the dust-free inner core is seen (© Herbert Hoinkis).

calcs, some measurements revealed a  $\Delta p$  of -10 to -15 hPa.

*Balme and Hagermann* [2006] demonstrated how efficient this  $\Delta p$  effect is in dust lifting from the surface. Especially the suspension of smaller particles in the air is possible by dust devils and may lead to an interference of air quality. *Greeley et al.* [2003] simulated dust devil lifting of particles with various sizes and with different ambient pressures. They confirmed that dust devils are more efficient at entraining particles into the atmosphere than wind speeds alone. The preliminary laboratory results of *Neakrase et al.* [2006] of dust removing rates by dust devils ( $1.0 \times 10^{-5}$  to  $3.0 \times 10^{-2}$  kg/m<sup>2</sup>/s) overlap quite well with field data of *Metzger* [1999] ( $0.6 \times 10^{-3}$  to  $4.4 \times 10^{-3}$  kg/m<sup>2</sup>/s) reported in *Balme and Greeley* [2006]. This suggests the removal of several kilogrammes of material by a dust devil which exists for about 20 minutes, indicating that much more can be removed by long-lasting large dust devils. Dust devils play an important role in transporting dust into the atmosphere and may have an impact on air quality in regions of high occurrence.

Lifting dust leads to track generation at the ground. Only two sources for dust devil tracks on Earth can be found despite several dust devil studies on different continents. *Rossi and Marinangeli* [2004] report dust devil tracks in the Ténéré Desert, Niger, using satellite data. These tracks have very low preservation potential and disappear quite fast. This could be the reason for the poor observations of tracks on Earth and that dust devil studies are normally grounded. The terrestrial tracks are similar to Martian dust devil tracks in their morphology, however, the Ténéré tracks have greater lengths and higher frequencies. No seasonal dependence is seen in this dataset [*Rossi and Marinangeli*, 2004].

The second source is an image (Figure 2.6a) taken in New Mexico, USA, long ago in 1959, which shows bright dust devil tracks. The passage of some dust devils disturbed the desert

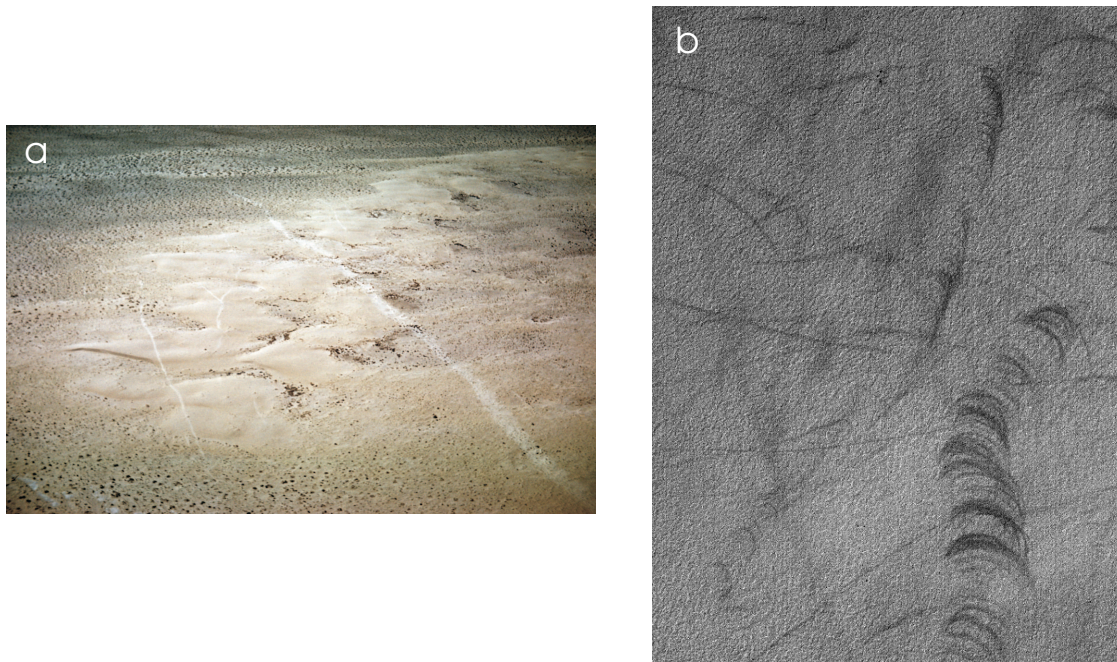


**Figure 2.6:** a) Bright dust devil tracks on dunes northeast of Sheep Springs, New Mexico, USA (© Louis J. Maher, Jr.). b) Martian dust devil tracks near  $62.6^{\circ}\text{S}$ ,  $271.0^{\circ}\text{E}$ , imaged in local summer (© NASA/JPL/Malin Space Science Systems; MGS MOC Release No. MOC2-1571).

surface removing material which covered probably the fine sand of the dunes creating this time bright tracks.

Although dust devil studies on Earth [Ives, 1947; McGinnigle, 1966; Sinclair, 1969] have been done long before dust devils have been seen for the first time on Mars, the interest strongly increased after their detection in Martian images. Understanding their formation, development and characteristics would help to improve the knowledge of the Martian atmosphere and especially the dust cycle, which is the dominant meteorological factor in the Martian weather.

## 2.3 Dust Devils on Mars

Before Martian dust devil features are discussed and presented in detail, the atmosphere of Mars is briefly introduced in the current state and the differences to the Earth's atmosphere are highlighted.

### The Atmosphere of Mars

Mars has a very thin atmosphere. The pressure at the surface constitutes just about 6.7 hPa, or 0.67% of that on Earth [Schofield *et al.*, 1997]. This is equivalent to a pressure found about 35 kilometres above ground level on Earth. The surface gravity acceleration is roughly one third of the Earth's. The major atmospheric components are Carbon Dioxide ( $\text{CO}_2$ , 95.32%), Nitrogen ( $\text{N}_2$ , 2.7%), Argon (Ar, 1.6%), Oxygen ( $\text{O}_2$ , 0.13%) and Carbon Monoxide (CO,

0.08%). Water (H<sub>2</sub>O, 0.03%) plays only a minor role in the atmosphere, and liquid water can not exist for long on the Martian surface because of the thin atmosphere. It is only present as water ice below the CO<sub>2</sub> ice caps at the Martian poles or in subsurface reservoirs. In local summer when the CO<sub>2</sub> ice is melting and reentering the atmosphere, water ice is exposed. Also CO<sub>2</sub> and H<sub>2</sub>O haze and clouds can be seen in images. The factor water which has the most important function in Earth's weather, is replaced by the dust on Mars.

Much of the Martian surface is covered with dust. Despite the thin atmosphere, winds can raise dust or, if the winds are weak, dust devils will entrain dust into the atmosphere. Approximately  $2 \times 10^{-2}$  kg/m<sup>2</sup>/a of dust is removed from the surface to support the observed atmospheric haze [Pollack *et al.*, 1979]. This value is confirmed by observed dust settling rates found with the MARS PATHFINDER rover SOJOURNER [Rover Team, 1997]. It is expected that dust devils and dust storms account for a large amount of this airborne dust. If winds are strong, they can cause regional dust storms, which sometimes become global. The preferred season for dust storms is southern summer, because the southern hemisphere is tilted towards the Sun when Mars is closest to the Sun. Since the orbit of Mars has a higher eccentricity than the Earth's orbit, this results in greater heating and stronger trade winds.

Trade winds are produced by the Hadley circulation, similar to the Earth's driving forces. Two Hadley circulations, one on each hemisphere, are established at the equinoxes. During summer/winter times, one large Hadley cell is established crossing the equator. The warm air rises in the respective summer hemisphere, moves towards the winter hemisphere, descends and cooler air moves back to the summer hemisphere at lower altitudes. The wind speed is usually below 10 m/s, but can rise to 30 m/s in dust storms.

The global annual average temperature at the surface is about -60°C. The diurnal temperature range is between -90 and -10°C measured in 1 m height with MARS PATHFINDER [Golombek *et al.*, 1999]. Fluctuations up to 20°C are possible in the morning due to the warming of the surface and the consequential convection. The range of surface temperatures is between -133 and +27°C [Kieffer *et al.*, 1992]. There is one major difference between the two climates of Earth and Mars because of the lower temperatures and the high concentration of CO<sub>2</sub>: the pressure decreases globally by about 30% every winter, because a large amount of CO<sub>2</sub> condenses around the poles. This results in two pressure maxima and two minima every Martian year [Kieffer *et al.*, 1992]. At the edge of the polar caps strong winds are predicted due to temperature gradients which may favour the development of dust devils and dust storms.

In several boundary layer studies for Mars the question is addressed if the similarity theory of Monin and Obukhov [1954] can be applied to Mars as well. Larsen *et al.* [2002], Tillman *et al.* [1994] and Määttänen and Savijärvi [2004] showed by testing the similarity parameterisation with MARS PATHFINDER and VIKING data, that the turbulent Martian atmospheric boundary layer generally obeys the same similarity laws, although the diurnal stability variations on Mars are quite strong even compared to Earth's desert conditions. The main differences can be related to the low air density (0.02 kg/m<sup>3</sup>) of the Martian atmosphere. The effect of the atmospheric heat flux is reduced due to the low air density and the nearly complete absence of water vapour. This increases the temperature variations and the near-surface vertical temperature gradient, leading the diabatic heat flux to higher values than on Earth [Larsen *et al.*, 2002]. A deeper boundary layer height is the consequence. Since wind speeds are similar

to Earth's, the main force is the temperature or the radiative balance. *Tillman et al.* [1994] estimated the turbulent daytime boundary layer height between 3.5 and 9.1 km for different surface roughnesses using data from the VIKING Lander 2 Meteorology Instrument System for selected sols (1 sol = 1 Martian day). *Larsen et al.* [2002] found a height of 6.3 km for an unstable case which fits the MARS PATHFINDER data better than a lower boundary layer height. They suggest that the boundary layer height may rise up to the atmospheric scale height (11 km) on Mars.

## Martian Dust Devil Characteristics

It was assumed and predicted that dust devils may exist on Mars as well [*Neubauer*, 1966; *Gierasch and Goody*, 1973], before they have been seen for the first time in VIKING images by *Thomas and Gierasch* [1985] (Figure 2.7). The number of detections increased a lot when the MARS GLOBAL SURVEYOR Mars Orbiter Camera (MOC) started to work, showing dust devils with greater details in the high-resolution images [*Malin and Edgett*, 2001]. Not only snap-shots but the motion of dust devils can be seen with the MARS EXPRESS High Resolution Stereo Camera (HRSC) [*Stanzel et al.*, 2006; 2007]. Dust devils were noticed in in-situ measurements of meteorological parameters done with the two VIKING landers [*Ryan and Lucich*, 1983; *Ringrose et al.*, 2003] and the MARS PATHFINDER lander [*Schofield et al.*, 1997]. Images of dust devils from the surface were obtained with MARS PATHFINDER [*Metzger et al.*, 1999; *Ferri et al.*, 2003] and the Mars Exploration Rover SPIRIT [*Greeley et al.*, 2006] (Figure 2.8).

Martian dust devils can be considerably larger than their terrestrial analogues. They are frequently a few kilometres high and hundreds of metres in diameter [*Thomas and Gierasch*, 1985]. Larger dust devils were much easier to detect in early observations of orbiters which had a lower resolution than cameras of today can provide. With increasing resolution much smaller dust devils were detected. The lander SPIRIT imaged even dust devils with less than 10 m in diameter [*Greeley et al.*, 2006]. Martian dust devils have a larger range of size compared to dust devils on Earth, transporting dust into even higher altitudes.

The lifetime of dust devils on Mars can generally not be measured since dust devil duration is mostly longer than the possible observation (in most cases just one image). Estimations of the duration became only possible with the orbiter MARS EXPRESS [*Stanzel et al.*, 2007] and the lander SPIRIT [*Greeley et al.*, 2006], using the forward speed and the covered distance of the detected dust devils. SPIRIT observations revealed 0.3 to 32.3 min of minimum lifetime. Minimum lifetime means for the lander images that the dust devil already existed when the first image of the image sequence was taken or it probably existed further after the last image was taken. SPIRIT could also image full cycles of some dust devils showing lifetimes between 0.7 and 11.5 min. Since the observed dust devils are smaller ones, a longer duration of dust devils up to several hours can be expected as for dust devils on Earth.

Most dust devil observations are reported between late morning (~1000 hours) and late afternoon (~1700 hours) following the same diurnal activity and probably the same rules as dust devil activity on Earth. The peak activity is mostly seen after noon [*Greeley et al.*, 2006].

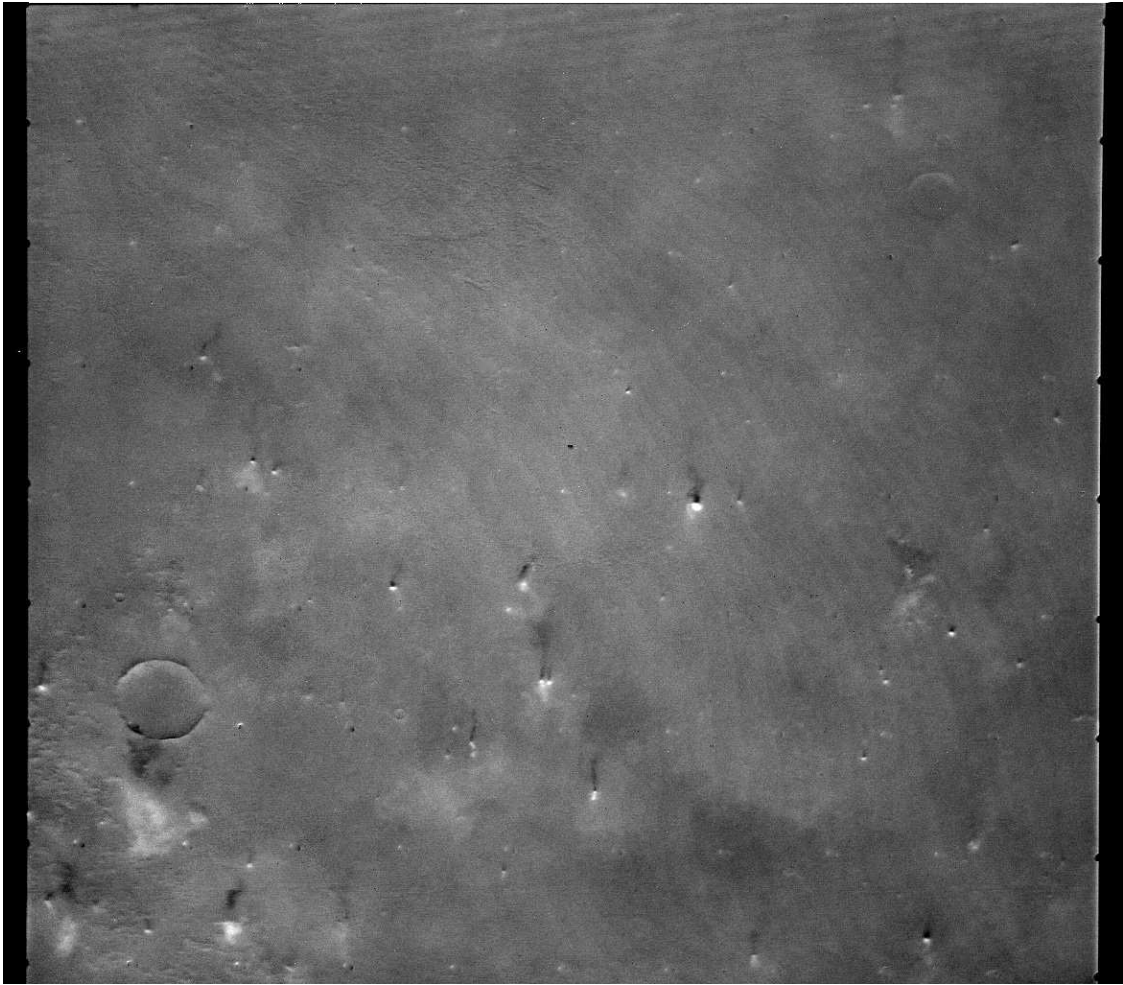


**Figure 2.7:** VIKING image (image-id f034b01<sup>1</sup>) with many dust devils seen in Amazonis Planitia (image centre at 36.8°N, 206.9°E) taken on September 13, 1976.

The seasonal activity of Martian dust devils follows the maximum insolation [Ryan and Lucich, 1983; Thomas and Gierasch, 1985] so that most dust devils are seen in local spring and summer. Mars is closest to the sun when the southern hemisphere is tilted towards the sun, leading to higher insolation. Whelley and Greeley [2006] note that this is also the reason why the southern summer Hadley cell is more energetic than the northern summer Hadley cell. And if the atmospheric energy is related to dust devil activity, this would lead to more dust devils in the southern than in the northern hemisphere as well.

Generally, dust devils should evolve wherever the atmospheric conditions are suitable and lifting material is available. The altitude seems to play no role for dust devil development. Dust devil streaks were found at the summit of Olympus Mons which is 27 km high [Malin and Edgett, 2001], and in low-level plains such as the Hellas Basin (9 km deep) [Balme et al., 2003b]. Previously, it was thought that dust devils would develop more often in lowlands because of the higher pressure which makes it more easy to lift smaller particles. The low-pressure cores of dust devils, however, seem to be effective enough to lift dust even in the thin atmosphere on the high volcanoes on Mars.

Some studies showed that certain regions seem to be more favourable for dust devil develop-

---

<sup>1</sup>See Appendix A for image identifiers

ment than others. *Fisher et al.* [2005] analysed nine different regions located on both hemispheres. They have found many active dust devils in Amazonis Planitia but much less in the other regions. Especially the Casius region revealed no single active dust devil but many



**Figure 2.8:** A dust devil seen from the surface with the Mars Exploration Rover SPIRIT at Sol 486, taken at 11:55 local solar time. Adapted from *Greeley et al.* [2006].

tracks. The reason may be that some regions are more dusty than others, so that the removal of a thin layer of dust by the passage of a dust devil does not lead to a change in the albedo. This does not explain, however, why regions with many dust devil tracks, and therefore many active dust devils which created these tracks, show no single or much less active dust devils. Since tracks remain mostly for one year, the possible reason is that the analysed images are taken at a time where no active dust devils occur but the tracks are still seen before they are covered by settling dust.

*Whelley and Greeley* [2006] compared regions with the same thermal inertia, a parameter indicating if a region is rich in dust, and noted that there must be yet another factor than the surface dustiness for the latitudinal distribution of dust devil tracks. The ascending branch of the Hadley cell is located where the heating is the greatest. This leads to a deeper convective layer and higher thermodynamic efficiency. More solar heating reinforces atmospheric instability and horizontal temperature gradients which are two important factors for dust devil occurrence [*Sinclair*, 1973; *Rennó et al.*, 1998; 2000]. Dust devil tracks had the highest density between 50° and 60°S in the work of *Whelley and Greeley* [2006], who analysed MOC images. The high dust devil track abundance in the Hellas Basin and Argyre Planitia found by *Balme et al.* [2003b] complements these results, strengthening the assumption that the location of the ascending branch of the Hadley cell is a place where dust devil formation is supported by the local atmospheric conditions.

Investigators select usually certain regions analysing all images covering these areas to determine the frequency of dust devils. Either active dust devils are counted or dust devil tracks (Figure 2.6b, page 14). This poses the question if dust devil tracks can be used as a proxy for active dust devils, since not all dust devils create streaks or the surface is too dusty so that the removal of a small amount of dust does not create a track. Additionally, dust devil tracks last longer than active dust devils do, so it is not well known in which time frame the tracks have been created. They tend to fade within one year [*Malin and Edgett*, 2001; *Balme et al.*, 2003b], usually evolving during the dust devil seasons spring and summer, and vanishing during autumn and winter because of dust deposition. Dust devil tracks can therefore be used to determine the frequency of dust devils. At least they are an good approximation for the occurrence of dust devils within one year.

*Balme et al.* [2003b] analysed dust devil tracks in Argyre Planitia and Hellas Basin and found an average dust devil track density of 0.81 tracks/km<sup>2</sup> for Argyre and 0.47 tracks/km<sup>2</sup> for Hellas within one Martian year. The peak value is 2.7 tracks/km<sup>2</sup> in spring for Argyre,

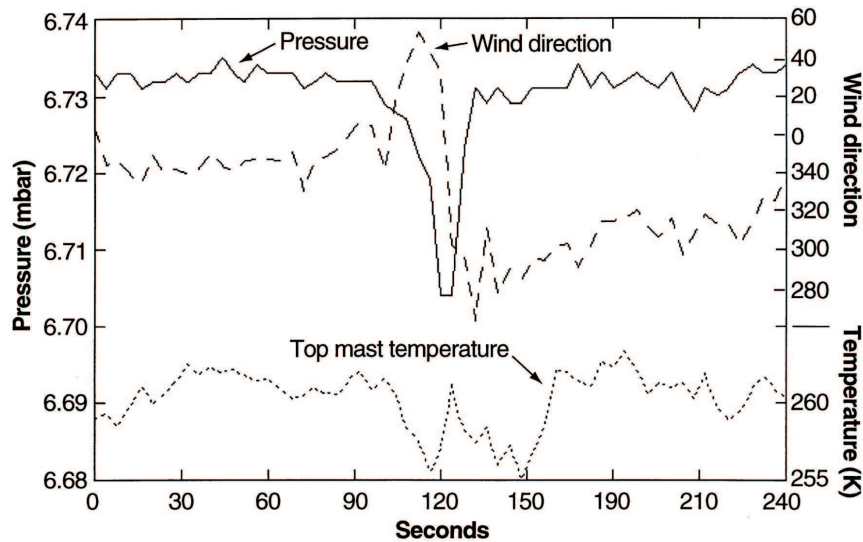


**Figure 2.9:** Pressure, wind and temperature changes associated with a dust devil passing through the Pathfinder landing site. Adapted from Schofield *et al.* [1997].

and 2.1 tracks/km<sup>2</sup> in summer for Hellas. The frequency is almost zero throughout the winter for both areas. Active dust devils and dust devil tracks have been analysed by Fisher *et al.* [2005] revealing a peak value of 0.0025 dust devils/km<sup>2</sup> in summer in their seasonal study of dust devil frequency in Amazonis Planitia. In good agreement with the results of Balme *et al.* [2003b] are the analysed data of Whelley and Greeley [2006]. They counted 2.4 tracks/km<sup>2</sup> in summer in Argyre Planitia. Combining several investigated areas depending on if they are located on the northern or on the southern hemisphere, reveals an average density of 0.6 tracks/km<sup>2</sup> in the southern hemisphere in contrast to 0.06 tracks/km<sup>2</sup> in the northern hemisphere. This shows again the effect of the greater insolation on dust devil formation. The value of dust devil density in Amazonis by Fisher *et al.* [2005] is lower for this reason as well, but also because active dust devils are less seen than their corresponding tracks.

With the image sequences of the SPIRIT lander, first observations of dust devil density became possible from the surface. Greeley *et al.* [2006] found 50 active dust devils/km<sup>2</sup>/sol. This means that dust devils are much more common than previous analyses have shown. However, it has to be kept in mind, that these SPIRIT dust devils are mostly much smaller (10-20 m in diameter) than dust devils which can be detected in orbiter images. Smaller dust devils or tracks cannot be resolved because of the limited resolution of the images.

Knowing the frequency of dust devils and the dust flux from one dust devil, the total amount of dust which is transported into the atmosphere by dust devils can be estimated and compared to the atmospheric dust settling rate. Greeley *et al.* [2006] give dust fluxes of  $3.95 \times 10^{-9}$  to  $4.59 \times 10^{-4}$  kg/m<sup>2</sup>/s for one dust devil, yielding in a dust load of 19 kg/km<sup>2</sup>/sol or  $1.3 \times 10^{-2}$  kg/m<sup>2</sup>/a with 50 active dust devils/km<sup>2</sup>/sol. Balme *et al.* [2003b] calculated a range of  $3 \times 10^{-6}$  to  $3 \times 10^{-3}$  kg/m<sup>2</sup>/a for analysed dust devil track densities in Argyre Planitia and Hellas Basin. With a global dust settling rate of  $2 \times 10^{-2}$  kg/m<sup>2</sup>/a [Pollack *et al.*, 1979] these results show that dust devils can contribute significantly to the dust loading of the atmosphere but may still not be responsible for the main part of dust entrainment into the atmosphere from the surface.

The MARS PATHFINDER and the two VIKING landers with their meteorological equipment have been the only possibilities on Mars to measure dust devil characteristics in-situ. Analysing the VIKING data revealed a horizontal wind speed of 42 m/s in 1.6 m height during the passage of vortices [Ryan and Lucich, 1983]. Ringrose *et al.* [2003] reanalysed VIKING lander 2 data and found wind speeds of up to 46 m/s at this height for vortices which passed directly over the instruments. Since the radial velocity  $u$  is almost zero within dust devils, these high values correspond to the tangential wind speed component  $v$  and seem to be higher than for terrestrial dust devils (<25 m/s). Estimations for the vertical velocity  $w$  within dust devils were done for the first time by using image sequences from the SPIRIT rover by following dust clots which were transported upwards by the dust devils [Greeley *et al.*, 2006]. The results range from 0.1 to 10.4 m/s with an average speed of 1.8 m/s, similar to speeds measured within dust devils on Earth.

As for terrestrial dust devils, it is assumed that dust devils on Mars move with the ambient wind at a few metres per second (<5 m/s [Metzger *et al.*, 1999]). This is indeed the case for most of the dust devils, some exceptions show speeds up to 20 m/s [Greeley *et al.*, 2006]. It is thought that high wind speeds suppress dust devil activity.

The rise in temperature was measured to be 5-6 K with VIKING and MARS PATHFINDER during dust devil passages. Balme and Greeley [2006] state in their dust devil review that these values are maybe underestimating the real conditions, since the sample rates of the measurements were not as high as during some terrestrial field studies.

Pressure drops associated with dust devils were also possible to detect in the meteorological data collected by MARS PATHFINDER because of the sufficient sample rate. Schofield *et al.* [1997] give peak values of 0.01-0.05 hPa for the decrease in pressure taking usually less than one minute (Figure 2.9).

The rise in temperature (0 to +6 K) and the decrease in pressure (-0.01 to -0.05 hPa) seen in data collected on Mars and associated with the passage of dust devils is much less than measurements of terrestrial dust devils have shown in some cases (temperature +22 K, pressure -10 to -15 hPa). For the temperature excursion, this can be partly referred to the low sampling rate, the low measuring height of mostly about 1 m and that only some of the dust devils are crossing with their centre of core over the measuring instruments on Mars. Pressure drops are usually 0.2-1.5 percent of the ambient pressure of the respective planet and are therefore consistent for terrestrial and Martian dust devils. Meteorological characteristics of Martian dust devils should have the same order of magnitude of values as dust devils on Earth or even higher because of their larger sizes.

---

**MISSIONS TO MARS**

---

In this chapter those Mars missions are briefly introduced, whose images have been used and analysed with the pattern recognition and classification software developed in this study.

**3.1 VIKING**

The VIKING mission was composed of two spacecraft, VIKING 1 and VIKING 2, each consisting of an orbiter and a lander. The primary mission objectives were to obtain high resolution images of the Martian surface, characterise the structure and composition of the atmosphere and surface, and search for evidence of life. VIKING 1 was launched on August 20, 1975 and arrived at Mars on June 19, 1976. The first month of observations was devoted to surface imaging to find appropriate landing sites for the VIKING landers. On July 20, 1976 the VIKING 1 lander separated from the orbiter and touched down at Chryse Planitia (22.48°N, 310.03°E). VIKING 2 was launched September 9, 1975 and entered Mars orbit on August 7, 1976. The VIKING 2 lander touched down at Utopia Planitia (47.97°N, 134.26°E) on September 3, 1976. The orbiters imaged the entire surface of Mars at a resolution of 150 to 300 m/pixel, and selected areas at 8 m/pixel. The lowest periapsis altitude for both orbiters was 300 km. The VIKING 2 orbiter was powered down on July 25, 1978 after 706 orbits, and the VIKING 1 orbiter on August 17, 1980, after over 1485 orbits. The VIKING landers transmitted images of the surface, took surface samples and analysed them for composition and signs of life. They studied the atmospheric composition and meteorology and deployed seismometers. The VIKING 2 lander ended communications on April 11, 1980, and the VIKING 1 lander on November 13, 1982, after transmitting over 1400 images of the two sites.

The results from the VIKING experiments gave the first realistic view of Mars. Volcanoes, lava plains, immense canyons, cratered areas, wind-formed features, and evidence of sur-

face fluids are apparent in the orbiter images. The planet appears to be divisible into two main regions, northern lowlands and southern cratered highlands. Superimposed on these regions are the Tharsis and Elysium bulges, which are high-standing volcanic areas, and Valles Marineris, a system of giant canyons near the equator. Measured temperatures at the landing sites ranged from  $-123^{\circ}\text{C}$  to  $-23^{\circ}\text{C}$ , with a variation over a given day of 35 to 50 K. Seasonal dust storms, pressure changes, and transport of atmospheric gases between the polar caps were observed. More than 50000 images have been returned to Earth from both, the orbiters and landers.

Each VIKING orbiter was equipped with two identical vidicon cameras, called the Visual Imaging Subsystem (VIS) with camera A or B. Five colour filters could be applied to the camera or a clear position (no filter) could be chosen. The raw data are radiometrically and geometrically not corrected. A full-resolution, uncompressed VIKING orbiter image consists of an array of 1056 lines with 1204 samples per line. There are only 1182 valid samples in each line. The extra 22 samples in each line consist of dark bands on the left and right edges of each image, produced by an opaque mask located at the front of the vidicon (see Figure 2.7, page 17). Each dark band is approximately 11 samples wide, although the exact width varies from image to image.

## 3.2 MARS GLOBAL SURVEYOR

The MARS GLOBAL SURVEYOR orbiter is one of the oldest Mars spacecraft and it has studied the red planet for nearly a decade. MARS GLOBAL SURVEYOR was the first successful NASA mission launched to Mars since the VIKING mission in 1976 and arrived at Mars on September 11, 1997 (September 12, UTC). After the aerobraking phase MARS GLOBAL SURVEYOR circled in a polar orbit (travelling over the north pole to the south pole and back to the north pole) once every two hours, twelve times a day, collecting global ‘snapshots’ from 400 km above the Martian surface. The additional sun-synchronous orbit has the advantage to analyse images of different times with the same illumination conditions which rules out artefacts or misinterpretations because of the illumination. The disadvantage of the sun-synchronous orbit is that no diurnal cycle can be observed, since the local time is 1300-1500 hours for all acquired MOC images. MARS GLOBAL SURVEYOR has been able to characterise the topography, gravity, magnetic fields, thermal properties, surface composition and atmosphere of Mars. In its extended mission principal goals were the continued weather monitoring and the imaging of possible landing sites. More than 250000 images have been returned to Earth. The spacecraft went silent in November 2006 after a wrong command was uploaded. Communication could not be reestablished since then.

MOC is a line-scanning camera. It takes one line at a time building the images while moving around the planet. MOC took a daily wide angle (WA) image of Mars similar to weather photographs of the Earth with a blue or red filter, and narrow angle (NA) images. These NA images have a resolution of 1.5 to 12 m/pixel and are greyscale images. The red and blue WA images provide the context for the smaller images with  $\sim 240$  m/pixel resolution, and daily global mapping images with 7.5 km/pixel. The size of the images can differ and may range

from  $2.8 \text{ km} \times 2.8 \text{ km}$  to  $2.8 \text{ km} \times 25.2 \text{ km}$  for NA images with 1.4 m/pixel resolution due to the available internal digital buffer memory. With a resolution of 11 m/pixel the images can be much longer, ranging up to  $2.8 \text{ km} \times 500 \text{ km}$ .

The images are available as raw images, which can be decompressed via delivered software. Otherwise the images are unprocessed (no radiometric or geometric correction) and uncalibrated. Due to the observation geometry and the fact that the camera is a line-scanning instrument, it is possible that the images have to be flipped left-to-right before processing or applying any illumination depending angle.

### 3.3 MARS EXPRESS

MARS EXPRESS got its name because of the rapid development time and the relatively short cruise time of about seven months to Mars. It is the European Space Agency's (ESA) first planetary mission. After launch on June 2, 2003, MARS EXPRESS arrived at Mars on December 25, 2003. MARS EXPRESS consisted of one orbiter and one lander named Beagle 2, which was separated successfully before orbit insertion of the orbiter. Unfortunately, communication could never be established after the supposed landing, so the lander mission failed due to a possible crash on the surface. The spacecraft has a highly elliptical orbit with a closest approach to the surface (pericentre) of 258 km. The quasi-polar orbit (inclination of  $86.35^\circ$ ) can be optimised for the scientific objectives, such as the pericentre is moved over the surface from the poles to the equator investigating the regions at different local times and seasons. During the prime mission, approximately three orbits per sol were conducted and the spacecraft returned every eleventh orbit to the same pericentre place but slightly shifted in longitude and latitude. Currently, MARS EXPRESS is in its first extended mission (end on October 31, 2007) and will likely perform a whole second one. The resonant orbit of MARS EXPRESS will therefore be changed at the end of 2007 from 11:3 to 18:5, which means five orbits per day and the same site after 18 days.

The orbiter provides an excellent global coverage of the planet, in particular of the surface, subsurface and atmosphere. The scientific objectives are the global colour and stereo high-resolution imaging, the global infrared mineralogical mapping of the surface, the radar sounding of the subsurface structure down to the permafrost, the global atmospheric circulation and mapping of the atmospheric composition, the interaction of the atmosphere with the surface and the interplanetary medium, and, using radio science, to infer information on the atmosphere, ionosphere, surface and interior [*Chicarro et al.*, 2004].

The scientific instruments on the orbiter include:

- an energetic neutral atoms analyser (ASPERA)
- a super/high-resolution stereo colour imager (HRSC)
- a radio science experiment (MaRS)
- a subsurface-sounding radar/altimeter (MARSIS)
- an infrared mineralogical mapping spectrometer (OMEGA)
- an atmospheric Fourier spectrometer (PFS)
- an ultraviolet and infrared atmospheric spectrometer (SPICAM)

The properties of HRSC and its images will be explained in detail in the next chapter.

---

## THE HIGH RESOLUTION STEREO CAMERA

---

### 4.1 Imaging Technique

HRSC is a line-scanning instrument like MOC with nine CCD detectors mounted in parallel in the focal plane. The unique feature is its capability to obtain from nine channels almost simultaneously image data of the same site at high resolution. The nine detectors include three stereo, four colour and two additional channels for photometric purposes (Figure 4.1a), giving a total of five stereo channels with different phase angles. Any time-dependent variations of the illumination and the observational atmospheric conditions are avoided [Neukum *et al.*, 1998]. A line is imaged on the planet's surface perpendicular to the ground track of the spacecraft, resulting in an image swath during orbital motion. There are no gaps between adjacent lines. HRSC is operated in individual imaging sequences, where a typical sequence consists of nine independent images covering almost the same area, when the illumination conditions are sufficient for 4 to 30 min [Neukum *et al.*, 1998]. The size of an image strip is defined by the number of pixels per line and the image acquisition duration. The image width depends on the spacecraft altitude whereas the length is limited only by the spacecraft memory resources. The super-resolution channel (SRC) will serve as a nested super-resolution image in the middle of the HRSC image swath providing surface features at even greater detail. Single SRC images or also contiguous image strips can be done [Neukum *et al.*, 1998].

The multi-sensor concept of HRSC implies a phase angle between the different line sensors. The angle between the nadir (ND, vertical downward looking) channel and the two other stereo channels (S1 forward and S2 backward looking) is  $18.9^\circ$ . This technique permits stereo reconstruction by digital processing and rectifications, followed by the generation of digital terrain models. The ND channel has in general the highest resolution of 12.5 m/pixel for the whole image strip. The best resolution is of course given at the pericentre, and with increasing

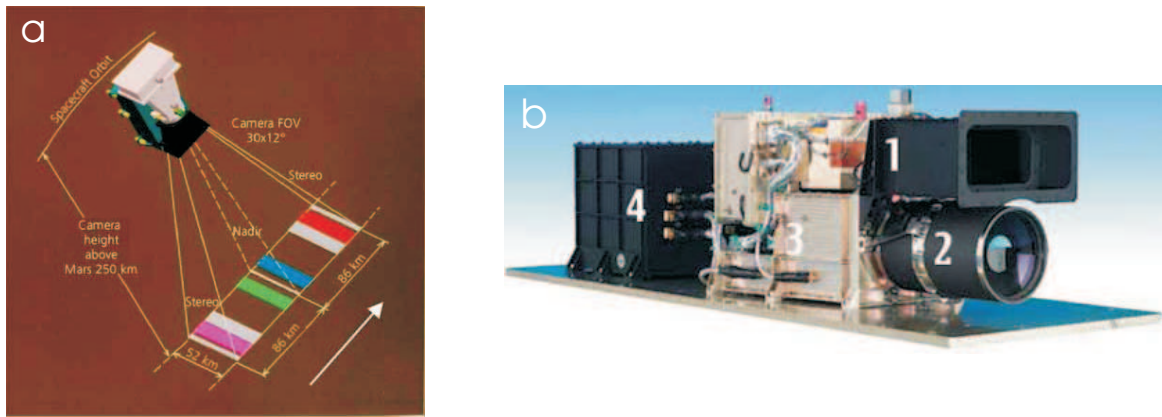


**Figure 4.1:** a) The HRSC operating principle and the viewing geometry of the individual sensors showing the footprint of three stereo, four colour and two photometric lines. b) The HRSC flight model. 1: HRSC, 2: SRC, 3: Frame Structure, 4: Digital Unit. Adapted from Neukum *et al.* [2004].

altitude of the spacecraft the resolution will decrease. The images are therefore rescaled to the best resolution for the whole image, but there is still the quality of the decreasing resolution with increasing distance from the pericentre. S1 and S2 images have usually a resolution of 25 m/pixel.

## 4.2 Scientific Objectives

It is intended to cover 50% of the Martian surface at a spatial resolution of  $\leq 15$  m/pixel, and more than 70% can be observed at  $\leq 30$  m/pixel during the prime mission (one Martian year) [Neukum *et al.*, 2004]. HRSC (Figure 4.1b) closes therefore the gap between medium- to low-resolution images like the VIKING images and the very high-resolution MOC images. Studies on HRSC images include the evolution of the surface in general, the morphology and topography, atmospheric phenomena and atmosphere-surface interactions, as well as the Martian moons Phobos and Deimos and the support for future lander missions.

The high resolution mapping helps to create geological maps in great detail. Stereo imaging and processing give an impression of the topography and digital terrain models are determined. Multispectral data derived from the four colour channels allow to classify the terrain and interpret the mineralogical composition. Atmospheric corrections can be done using the colour and multi-phase images [Neukum *et al.*, 2004]. Additionally, small changes of variable atmospheric features like dust devils or clouds can be tracked using the images of the same site but slightly shifted in time.

## 4.3 The Analysis of Dust Devils in HRSC Images

The search for dust devils is done using so-called Level 3 image data. These images have been radiometrically and geometrically corrected in order to remove compression or transmission effects or effects due to the orbital motion. Laboratory or in-flight calibration data together

with attitude data of the spacecraft are used for the correction. The output are rectified map-projected images in which the Mars Orbiter Laser Altimeter (MOLA aboard MARS GLOBAL SURVEYOR) topography data has been used.

The ND and the stereo channels have usually the best resolution of 12.5 and 25 m/pixel, respectively. Dust devil characteristics like the diameter and the shadow length, from which the height is calculated knowing the solar incidence angle, are retrieved from the ND channel because of the best available resolution. If the dust devil can be identified in the other stereo channels as well and it is moving, the travelled distance can be calculated. This is also the method to exclude small bumps or hills, which can be misinterpreted as dust devils, but do not move. The movement is also the reason why dust devils cannot be displayed properly in an anaglyph (three-dimensional image) because the dust devils appear as smeared objects. Dust devils are sometimes seen when they just develop or break down between two image acquisitions.

Level 2 images (geometrically not corrected but radiometrically) have to be used to get the time (Earth time) when a dust devil was imaged. The dust devil has to be identified, independently of the identification in Level 3 data, and referred to a certain line in these Level 2 data. The time when this line was imaged can be read out from the binary prefix of the image file. The forward speed of a dust devil can therefore be computed for the first time as an analogue for the wind speed using the distance and the time difference between two dust devil positions imaged by different sensors.

Knowing the exact time when a dust devil was captured by the camera is also important for the correct calculation of the solar incidence angle. Since the HRSC images are long strips, this angle changes sometimes significantly from the start to the end of the imaging time. The exact angle provides the best estimation for the dust devil's height. Other important features for dust devil statistics are the time (local time and season) and the coordinates (latitude and longitude) when the dust devils occurred.

HRSC orthoimages are Level 4 or so-called higher level products. They are generated by rectifying the stereo and colour images to a newly derived HRSC digital terrain model (DTM) based on the former Level 2 stereo images. This time the images are not map-projected to the MOLA topography but to the new HRSC DTM. These Level 4 data should be more precise with a better quality than the former Level 3 data.

Orbits containing dust devils have been processed up to Level 4 on our own, since this product was not intended for delivery to the HRSC team at the beginning of the mission,

only the relevant software. Analysing the dust devils in these higher level images revealed totally different coordinates compared to the formerly derived Level 3 coordinates. This is due to the fact that dust devils as a vertical extended feature are regarded as small hills during DTM generation and mislead to a false topography. Map-projecting the Level 2 image to this

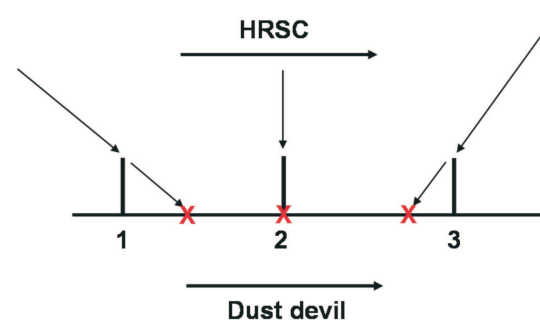


**Figure 4.2:** The principle of the parallax problem. More details in the text.

newly derived DTM leads to false coordinates. Level 3 images have therefore to be used for dust devil investigations.

The S1 and the S2 channel view the surface at an angle of  $18.9^\circ$ . If features are not at the surface or have a vertical extent (like dust devils), they will be reflected at a different location than they really are. Figure 4.2 shows the principle of the parallax error. The dust devil is moving from point 1 to 3. HRSC is flying in parallel. First, the forward looking channel images the dust devil. The top of the dust devil will appear in the image at the red cross, the foot point is seen in the image at the right position. At the second position, it is copied correctly by the ND channel. At the third position the top of the dust devil is again reflected at the wrong position. The dust devils appear to be stretched in the two stereo channels and there is a mismatch in the covered distance and the derived speed (if measured at the top of a dust devil). If HRSC is flying parallel to the dust devil motion, the distance is shorter; flying anti-parallel results in a larger distance. Additionally, there is also a parallax due to the width of the line sensors depending on the distance from the dust devil to the centre of the image swath. The contribution of this parallax error is almost negligible compared to the other along track error. These parallax effects were taken into account when discussing the speed results of the analysed dust devils detected in HRSC images (see Chapter 8, [Stanzel *et al.*, 2006]).

---

## PATTERN RECOGNITION AND CLASSIFICATION

---

In this brief chapter the principle and some characteristics of the pattern recognition and classification method are explained which is used to extract dust devils from Martian images.

Human beings are doing pattern recognition and classification all the time. If they read a text or greet a friend in the street, it depends on how their pattern recognition is working to identify characters or human faces properly and to classify them as a specific word or a known person. These are two examples of the field of problems where artificial pattern recognition can be addressed:

- visual quality control and production monitoring
- character recognition and automatic document evaluation and processing (address reader, signature authentication)
- speech and music identification
- medical computer-aided diagnosis
- satellite and aerial photographs (remote sensing)
- biology (monitoring cell growth, blood cell analysis)
- crime investigation (fingerprints, face recognition)

Classification is an independent part of the pattern recognition system but is often included when speaking of pattern recognition. The assignment of the complex automatic recognition of any kind of objects by human beings to a computer is the goal of artificial pattern recognition and classification. The human beings are able to filter the important information out of a large amount of data the eye is providing to the brain and also to save it, thus a recognition is possible. A pattern recognition system is therefore very helpful to identify the temporal and spatial variable dust devils in Martian images whereof more than 300000 are available.

## 5.1 Pattern Recognition Systems

### Sensing and Segmentation

The input to a pattern recognition system is often given as the product of a transducer like a camera or a microphone. The images or the audio files have then to be processed. The limitations of such a transducer (noise, resolution, etc.) may have an impact on the extraction of features and the pattern recognition results. The next step is the segmentation of the patterns we are interested in (Figure 5.1). This includes the problem of recognising if there is a target pattern at all or just the background given. Also subsets or supersets can complicate the segmentation of the target pattern. Regardless of the origin of the patterns, they can all be represented as vectors of multiple dimensions. These vectors are the input for the classifier.

### Feature Extraction

The boundary between feature extraction and classification can be arbitrary: an ideal feature extractor would make the job of a classifier trivial; on the other hand, an omnipotent classifier

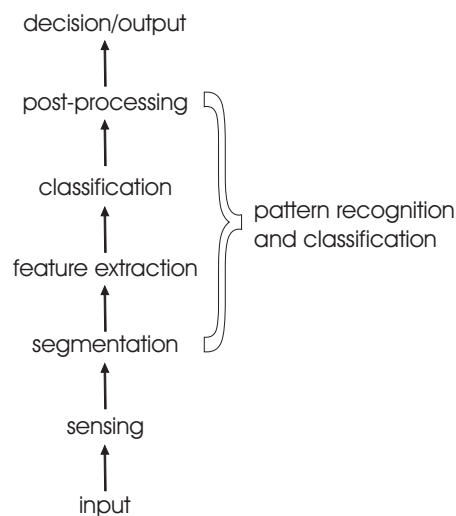


**Figure 5.1:** Pattern recognition systems can be partitioned into several steps. A sensor converts physical inputs into signal data. The segmentor isolates objects from the background. The feature extractor measures object properties and the classifier assigns the sensed object to a category. A post processor can overwrite the decision due to other considerations. Adapted from Duda et al. [2001].

features for classification. Various techniques can be used to select the most valuable features from a larger set of candidates.

does not need the help of a feature extractor [Duda et al., 2001]. Practical rather than theoretical reasons will let us distinguish and evolve appropriate tools.

The extracted features of an object should be recognised by similar values of measurements representative for this group but different for objects of another category. This leads to distinguishable values for different categories which should be invariant to irrelevant transformations of the input. That is in particular the translation, rotation or size of the target pattern. In general, features that describe properties like shape, colour and many kinds of texture are invariant to translation, rotation and scale.

A more or less domain specific problem for pattern recognition is the deformation of a pattern (hand recognition in different positions) or the rate at which a pattern occurs (speech recognition). A good knowledge of the problem/domain may help to find proper

## Classification

The difficulty of classification is the variability in feature values of the same category compared to the difference between feature values for objects in different categories [Duda *et al.*, 2001]. The variability is due to complexity of the parameters, or may be due to noise. Noise relies on the randomness of the sensors and not on the true appearance of the pattern. Exact classification performance is impossible in most cases, a more general approach is to determine the probability for each category.

In general, classifiers are not designed for a specific problem. Due to the complexity of the input space some classifiers will perform better than others on a certain problem.

## Post-Processing

A post-processor may use the output of a classifier and decide on a recommended action. For instance, a post-processor may check the context, that is input-dependent information (additional information provided by the system or user) other than from the target pattern (extracted features) itself [Duda *et al.*, 2001]. The former decision may then be modified.

The pattern recognition performance usually increases using multiple features. Combining the output of different classifiers could also sometimes enhance correct recognition. Each classifier could operate on different aspects or features of the input or a third classifier evaluates the output of the two former used classifiers [Zabel, 2005].

## 5.2 The Design Cycle

Several activities have to be conducted to design a pattern recognition system: data collection, feature selection, model choice, training and evaluation [Duda *et al.*, 2001].

The data collection can be quite time consuming compared to the remaining activities. The omnipresent question is when do we have enough data collected to have an adequately large and representative set of examples for training and testing?

The characteristics of the domain will influence the feature choice. Prior knowledge is very helpful to select promising features. The desire is to find features which are easily to extract, invariant to irrelevant informations, insensitive to noise and, of course, very useful for discriminating objects of different classes.

The choice of a model is also non-trivial. The question is when should another model be taken if the selected one is not performing well? Are guidelines available for the decision of a classifier not doing just trial and error?

Training a classifier means in general using data to determine the best classifier. The most effective way seems to be to learn from examples whereas methods of learning are quite essential in developing pattern recognition systems. These training sets could be already labelled with the right category and the classifier tries to minimise the costs for these patterns. This learning strategy is called supervised learning. Unsupervised learning or clustering means there is no a priori knowledge of the patterns' classes given, categories are determined on the

statistical regularities of the patterns by grouping (clustering) the input data. Different clustering methods from partitioning to model-based theories are mentioned in *Zabel* [2005]. A third possibility is the reinforcement learning where the feedback is just a ‘right’ or ‘wrong’. The evaluation is an important point to test the system and reveal a possible need for improvements. A perfect classification of training examples (training error almost zero) does not necessarily mean a good performance on new patterns (increased validation error). This problem is called overfitting [*Duda et al.*, 2001; *Zabel*, 2005]. A model shall not be too simple to not distinguish between different classes, and not too complex that new patterns are misclassified.

Chapter 6 and 7 will respond to questions raised in this section.

## 5.3 Characteristics in Pattern Recognition

### Data Space Partitioning

The feature vectors consist of  $n$  dimensions resulting in an  $n$ -dimensional input space spanned by all example vectors independent of the classes. The goal of pattern classification is to divide the input space in regions which represent one class. The feature vectors can be seen as data points or patterns in the input space. Each pattern presented to the pattern recognition system is assigned to one region called decision region. Patterns assigned to one region and actually belonging to the class the region is labelled with, are correctly classified, otherwise misclassified. The purpose of a pattern recognition system is to minimise the error of misclassification by putting decision boundaries between pattern examples forming decision regions.

### Adaptivity

Usually, no rules or heuristics are available for creating decision regions, but example patterns of different classes. A pattern recognition system has therefore to be adaptive to incorporate new patterns. Adaption is performed during training when a training set is presented to the pattern recognition system consisting of examples with correct classification. If the system misclassifies a pattern but is trained with the given right class label, it will learn for the future and will probably classify similar patterns correctly. The performance of a pattern recognition system will improve the more training examples are available and the capability increases to classify accurately a wider range of parameters of the same class [*Lee*, 1989].

### Generalisation

The pattern recognition system should be able to assign the right class to a pattern which is not included in a training data set [*Callan*, 2003]. This process is called generalisation. Generalisation based on adaption is the base of an intelligent system. Creating a well selected

training data set including a possible wide range of parameter values for patterns will help to distinguish new examples of different classes learning the essential properties.



---

## PATTERN RECOGNITION ALGORITHMS FOR MARTIAN DUST DEVILS

---

### 6.1 Dust Devils in VIKING Images

38 VIKING images were used as database for the pattern recognition algorithms to extract dust devil features. They were selected because a former search conducted at the Institute of Geophysics and Meteorology, University of Cologne, recognised dust devils in these images from different regions on Mars [Wennmacher *et al.*, 1996]. The search was started in Arcadia Planitia where the first dust devils have been seen on Mars [Thomas and Gierasch, 1985] and extended to several regions on the northern and southern hemisphere including the VIKING lander sites also known as regions where dust devils occur. A total of 240 dust devils were identified in 7 out of 23 regions, whereas Arcadia Planitia with 216 dust devils is clearly outstanding in contrast to one to six detections of dust devils in other regions. All dust devils were detected in local spring and summer of the northern hemisphere. The lack of dust devil detections in spring and summer of the southern hemisphere is referred to the less coverage of this hemisphere and the few images with a resolution of <100 m. The main part of the dust devils occurred between 1400 and 1530 hours out of a selection of images taken between 1200 and 1800 hours. The diameter was typically 200-300 m, the height ranges between 250-4000 m but was mostly 750-1000 m.

In preparation for the development of pattern recognition algorithms each image has been analysed again to verify the previous detections. This time, a total of 325 dust devils were counted in the 38 VIKING images, including more dust devils which have been rejected by the former investigators [Wennmacher *et al.*, 1996] probably due to their small size or strange shape. Some features looking more like small bumps or ridges, previously judged positive as dust devils, have now been rejected. Actually, there are only 313 dust devils included in these

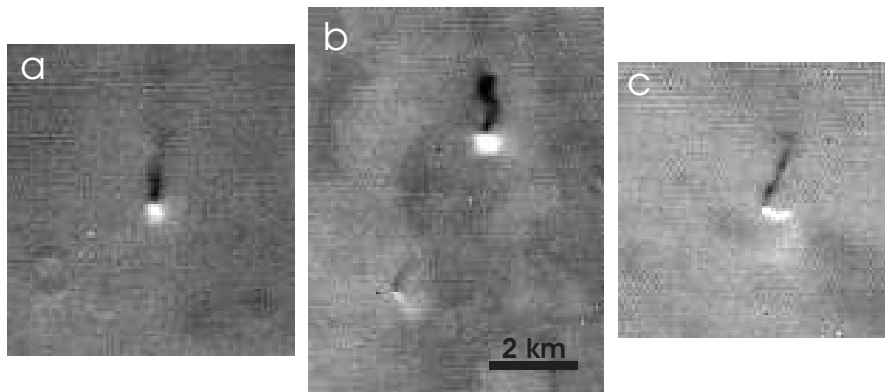


**Figure 6.1:** All dust devils were detected in Viking image f035b14 (image centre at  $41.19^{\circ}\text{N}$ ,  $146.30^{\circ}\text{E}$ ) taken on September 14, 1976. a) An almost perfect appearance of a dust devil with a circular bright spot and an elongated, rectangular and compact shadow. b) A larger dust devil with S-shaped shadow. In the lower left a small, not well represented dust devil is located with a tilted dust column. c) The dust devil column is strongly tilted to the right which is reflected in the cast shadow.

images. Twelve dust devils are counted twice when dealing with the images independently, because some VIKING images overlap. The number of 325 dust devils, however, is still valid for the pattern recognition search where each image is analysed on its own.

The images used for the dust devil search differ from the original raw data in that way they have been processed changing the format, correcting image errors, fixing missing pixels and lines, removing pixel spikes, removing camera shading and reseau and fiducial marks. Images are then radiometrically but not geometrically corrected. These steps were conducted using the VICAR (Video Image Communication and Retrieval) software provided by the Jet Propulsion Laboratory [Duxbury and Jensen, 1994]. Unfortunately, this software is no longer available at the Institute of Geophysics and Meteorology. However, the 38 VIKING images including 325 dust devils provide a sufficient database for the development of pattern recognition algorithms. Processing uncorrected VIKING images has a non-negligible effect on the pattern recognition of dust devils (see the following section). If it is intended to do a greater dust devil search in unknown VIKING images again, it is recommended to use the VICAR software before.

The available images are in the VICAR-format. This format is changed into the binary PGM-format (PortableGrayMap) by analysing the image label, retrieving the label and image size. This new PGM-format has the advantage to access particular pixels easier discarding the former label where additional image informations are included. There is also no loss in image information because no compression technique is applied. This is also the reason for using the original greyscale images and not the contrast enhanced images used for the visual search. Seven VIKING images (f034b01, f035b14, f035b16, f035b18, f038b23, f038b25, f038b27<sup>1</sup>) containing 126 dust devils have been selected to be the main database for pattern recognition development and testing. There are ten or more dust devils in each image to provide enough examples, ranging from very small to large dust devils, including dust devils with a strange shape (Figure 6.1). The other 31 images were used for testing and evaluating

<sup>1</sup>See Appendix A for image identifiers

of the algorithm.

### 6.1.1 The Search for Brightness Maxima

Visualised by the dust-filled column, dust devils are seen as bright features illuminated by the Sun, with a dark cast shadow in images from the Martian surface (Figure 6.1). These two characteristics seem to be the most important features for dust devil recognition. Thus, a search for relative brightness maxima was started in the greyscale images. A grid consisting of  $64 \times 64$  pixel squares was applied to the image, calculating the mean intensity  $I_{mean}$  and standard deviation  $\sigma$  of the pixel values for each square. Pixels with an intensity  $I > I_{mean} + n \cdot \sigma$  were filtered using values of 3 to 4 for  $n$  during the testing phase. Due to possible detection problems at the boundaries of the scan areas, an inner grid was applied to the image as a second step. It consists also of  $64 \times 64$  pixel squares, but has an offset of 32 pixels to the outer grid. The filtered pixels of the outer and inner grid are compared to each other compiling a list where each pixel appears only once. Figure 6.2a shows a black and white image where the filtered pixels are displayed white, all others are rendered black. A value of  $n = 3.8$  was found appropriate after some tests. If the search was not efficient (e.g. resulting in an almost black image), the factor  $n$  may be modified and the search is repeated. The white pixels represent quite well the bright spots of dust devils. The resulting black and white image, however, contains also parts of craters and noise represented by white pixels (Figure 6.2).

The impact of using unprocessed VIKING images (see previous section for the meaning of ‘unprocessed’ and ‘corrected’ images) is explained taking image f034b01 (Figure 6.2) as an example. A total of 2342 pixels have been filtered using the corrected image compared to only 1340 pixels in the not-corrected case. Also, not the same clusters are represented by the white pixels as well as much more single pixels (548 not-corrected to 320 corrected) are filtered. Single pixels are considered as the noise of the filtered data. Dust devils are less well represented using the unprocessed images. Nevertheless, if dust devils have a sufficient size and a clear bright spot and dark shadow, they are also detected in the unprocessed VIKING images.

Bright spots representing the dust-filled columns of dust devils are an important characteristic for the pattern recognition search. However, no parameters are retrieved building components of the feature vector because the degree of brightness is not a parameter to distinguish well between dust devils and craters for example. The search for brightness maxima is therefore a preselection of possible targets.

### 6.1.2 The Hoshen-Kopelman Algorithm

Only a list with filtered single pixels is known so far, but it is not clear which pixels build a cluster. The black and white image (Figure 6.2a) shows clusters but only because the position information of the filtered pixels has been used to arrange a black and white image according to the original image (Figure 6.2b). The goal is to know which pixels belong to

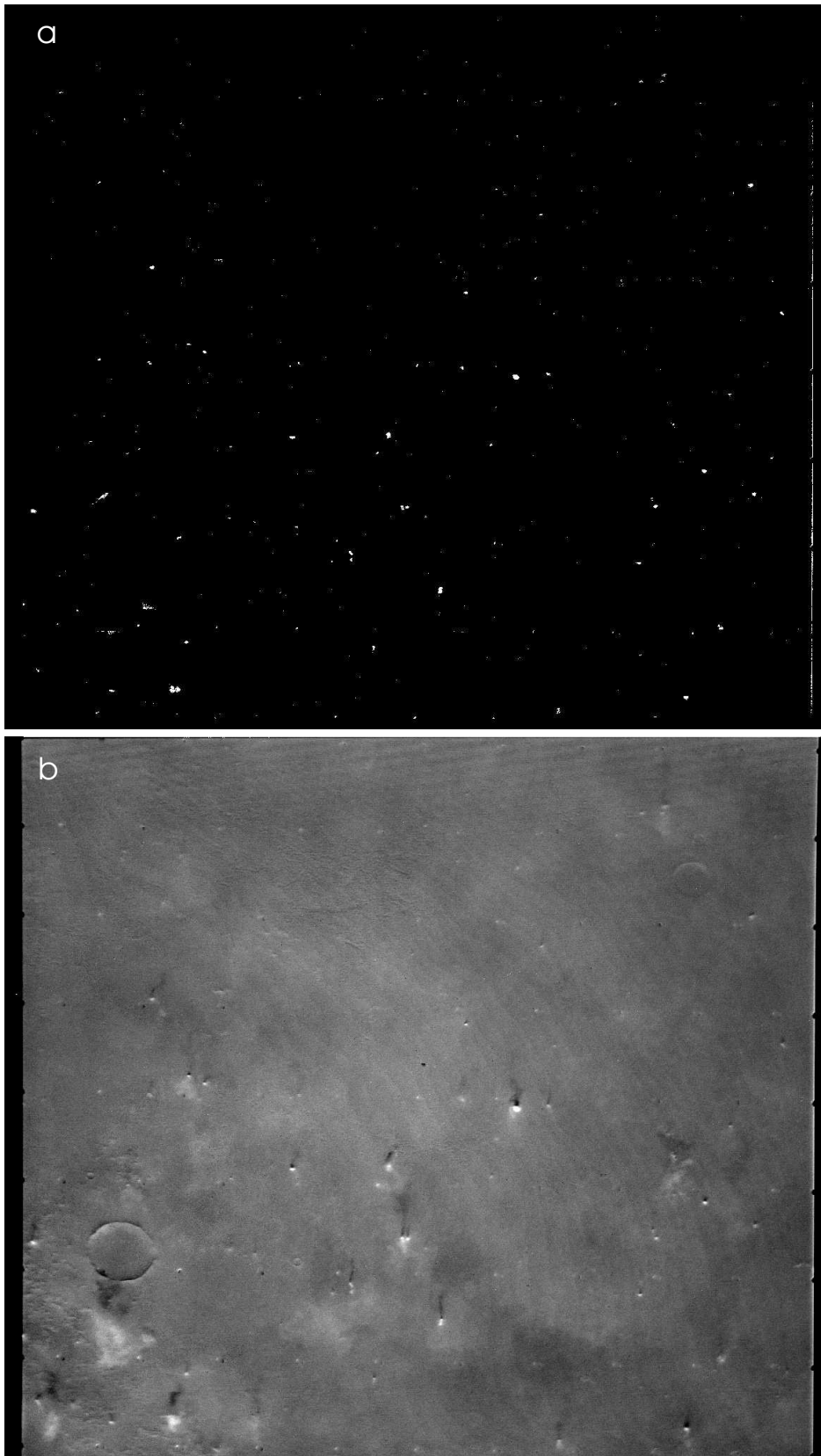


**Figure 6.2:** a) The filtered pixels ( $n = 3.8$ ) have been marked white, all others are rendered black, resulting in a black and white image. b) Corresponding to a) the contrast enhanced original greyscale Viking image (f034b01).

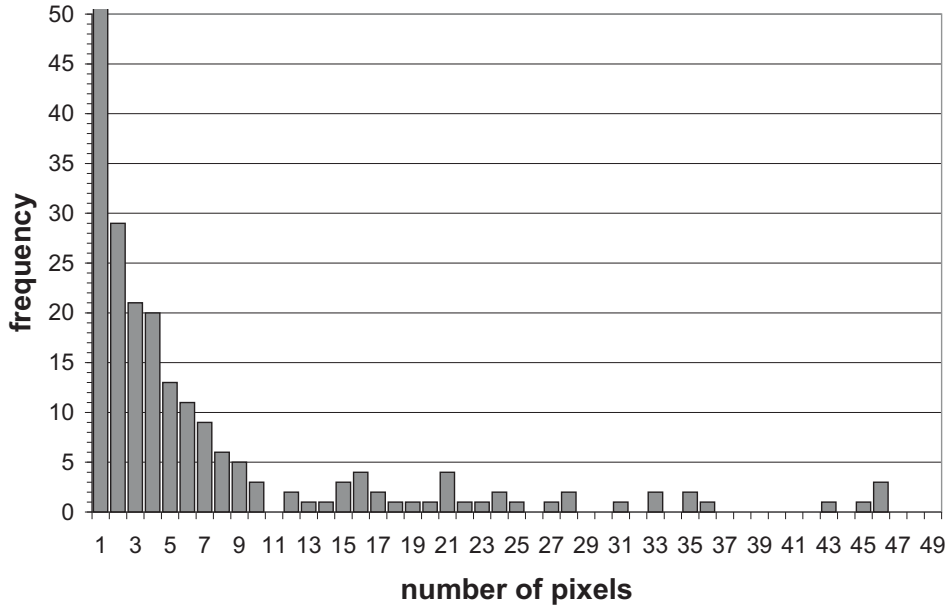


**Figure 6.3:** Cluster size distribution for image *f034b01*. The number of single pixels and clusters larger than 49 pixels are truncated due to displaying reasons. The number of single pixels is 320, there are clusters each once at 52, 61, 77, 90, 121 and 138 number of pixels. Dust devils are expected to be found at  $\sim 10$  pixels upward.

one cluster, how many they are and to ensure that every cluster can be identified and handled independently from other clusters.

The problem mentioned above is a typical percolation problem. The percolation theory describes the formation of the connection of occupied sites in lattice structures. This leads to a network of connections which can cross the whole system. If a cluster spans the whole lattice, from left to right or from the bottom to the top in the two-dimensional case, the system percolates. The Hoshen-Kopelman algorithm [Hoshen and Kopelman, 1976; Hoshen et al., 1976; Babalievski, 1998] is a percolation algorithm for multiple labelling for cluster statistics. The success of the method is based on the application of alternate labels to sites belonging to the same cluster but first given two different labels. The details of the implemented algorithm, lightly adjusted to our problem, can be found in Appendix B.

Figure 6.3 shows the cluster size distribution of VIKING image *f034b01* (Figure 6.2). The number of single pixels and clusters larger than 49 pixels are truncated in the figure for displaying reasons. The range from 1 to  $\sim 10$  pixel clusters describes definitely the noise in the image. Dust devil clusters are expected to be found from  $\sim 10$  pixels upward due to the resolution and the amount of clusters of these sizes in the image, namely just once or twice for a specific size. Clusters with sizes higher than 50 pixels may also be dust devils, but can likely be parts of craters or artefacts like the long lines at the right and left side of the VIKING images (e.g. Figure 6.2) due to the black bands (see Section 3.1). The size of a cluster represents one parameter of the feature vector.

### 6.1.3 Geometry Parameters

The shape of a cluster is thought to be a valuable parameter since it is expected that the dust devil column appears almost circular in the nadir view of the images. For this reason a best-fit ellipse will be adjusted to the detected clusters. A best-fit ellipse is those, whose least and greatest moments of inertia are equal to the least and greatest moments of inertia of the object (cluster). The moments of inertia for an ellipse are:  $J_{min} = \pi/4 \cdot ab^3$  and  $J_{max} = \pi/4 \cdot a^3b$ . If the moments of inertia are computed for the object and set equal to these equations, the semi-minor and semi-major axis, a and b, respectively, can be retrieved. The eccentricity  $\varepsilon = \sqrt{\frac{b^2-a^2}{b^2}}$  is the parameter we are looking for. The following equations show how the least and greatest moments of inertia, the semi-minor and semi-major axis and the angle  $\phi$  are calculated:

$$\begin{aligned}
 J_{min} &= \sum_x \sum_y [(x - x_s) \cos \phi - (y - y_s) \sin \phi]^2 \\
 J_{max} &= \sum_x \sum_y [(x - x_s) \sin \phi - (y - y_s) \cos \phi]^2 \\
 a &= \left(\frac{4}{\pi}\right)^{1/4} \cdot \left(\frac{J_{max}^3}{J_{min}}\right)^{1/8} \\
 b &= \left(\frac{4}{\pi}\right)^{1/4} \cdot \left(\frac{J_{min}^3}{J_{max}}\right)^{1/8} \\
 \phi &= \frac{1}{2} \arctan\left(\frac{2\mu_{11}}{\mu_{20} - \mu_{02}}\right), \quad \begin{aligned} \mu_{20} &= \sum_x (x - x_s)^2 \\ \mu_{02} &= \sum_y (y - y_s)^2 \\ \mu_{11} &= \sum_x \sum_y (x - x_s)(y - y_s) \end{aligned}
 \end{aligned}$$

Figure 6.4 illustrates a best-fit ellipse. The shaded area represents a possible cluster. Computing its least and greatest moments of inertia, the semi-minor axis a and semi-major axis b (unit is pixels) of a corresponding best-fit ellipse are derived.  $\phi$  describes the angle between the x-axis and the semi-major axis b. It ranges between  $-90^\circ$  and  $+90^\circ$  and provides an

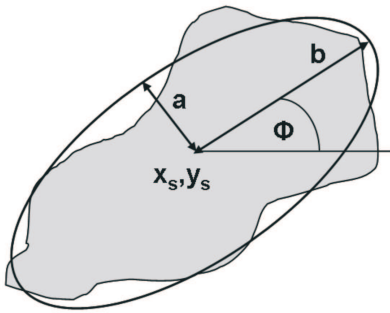


**Figure 6.4:** The shaded area illustrates a possible cluster with an adjusted best-fit ellipse. More details in the text.

indication of the orientation of the cluster.  $x_s$  and  $y_s$  are the coordinates of the barycentre of the cluster and are used to identify a detected object in the original VIKING image.

The analyses of the best-fit ellipses and their corresponding clusters showed the need for another parameter. There are cases where almost a circle was fitted to a cluster, the cluster, however, did not really fulfil the ellipse (Figure 6.5, Label 247). That is due to the strange shape of the cluster, more tattered than a compact one which is expected for the bright spot of a possible dust devil (Figure 6.5, Label 495). The new parameter  $q$  is the ratio of the cluster area within the

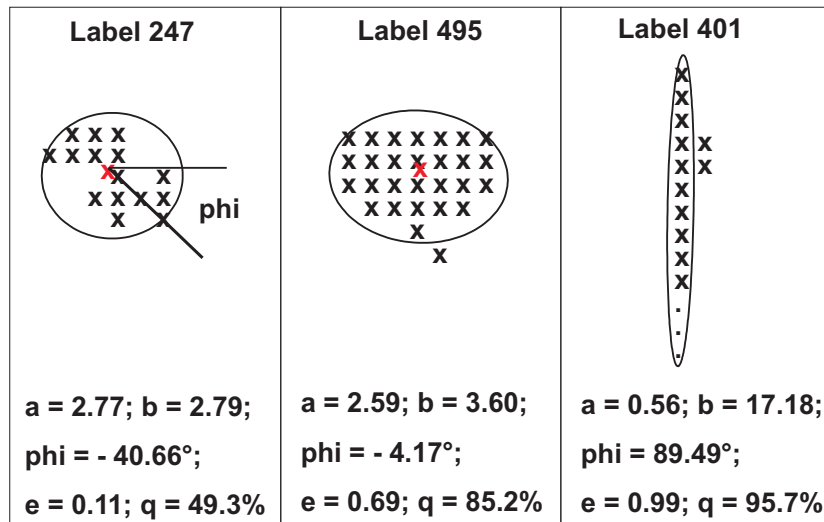


**Figure 6.5:** Three example clusters with their adjusted best-fit ellipse. All obtained from image f034b01. Label 247: Cluster with a tattered structure but the best-fit ellipse has an eccentricity  $\epsilon = 0.11$ . The parameter  $q$  shows the discrepancy between cluster and ellipse having only a value of 49.3%. The red  $x$  shows the position of the barycentre. Label 495: A more compact cluster representing indeed a dust devil column, showing a higher  $q$ -value and also an increased eccentricity. Label 401: Cluster representing a long line from the image border having a high eccentricity and a high  $q$ -value because of the clear shape.

ellipse to the area of the ellipse and is called quality parameter.

An additional advantage of calculating the moments of inertia of the detected clusters is that single pixels and strict lines are discarded. There must be at least one position different to the other  $x$ - or  $y$ -positions of a cluster, otherwise both or at least one of the moments of inertia are zero. Then the semi-minor and semi-major axis cannot be computed. Clusters for which no geometry parameters could be retrieved will no longer be considered and are deleted.

The seven selected VIKING images have been examined to constrain the values of eccentricity and quality parameter for possible dust devils. Dust devil clusters have been compared to craters and other features. Since dust devils may have diameters from a few tens to several hundreds of metres, the size of a cluster as well as the eccentricity may vary significantly if, for example the dust column is tilted by the wind shear (see Figure 6.1c, page 36). The eccentricity ranges from  $0.01 < \epsilon < 0.90$ , the quality parameter from  $46.3\% < q < 99.7\%$  for identified dust devils in the seven VIKING images. However, the value for  $\epsilon$  was only twice below 0.1 and ranges normally at higher values up to 0.7 or 0.8. Most values of  $q$  lie between 80% to 100% for dust devils. Figure 6.6 shows on the left hand histograms of the data derived during the search for the bright spot in all 38 VIKING images. In the range of 0.1 to 0.8 of the eccentricity, the total data (blue colour) consists almost completely of data derived from dust devils (red colour). Other clusters have a peak at  $\epsilon = 0.0$  or are usually close to 1. Dust devil values for  $q$  show the same distribution after the analyses of 38 images as when only the seven preselected images were examined. The majority is between 80% to 100%. The histogram for the size  $g$  shows that non-dust devil clusters are mostly located between 0 to 10 pixels, whereas most dust devils are found from a size of 10 pixels onward.

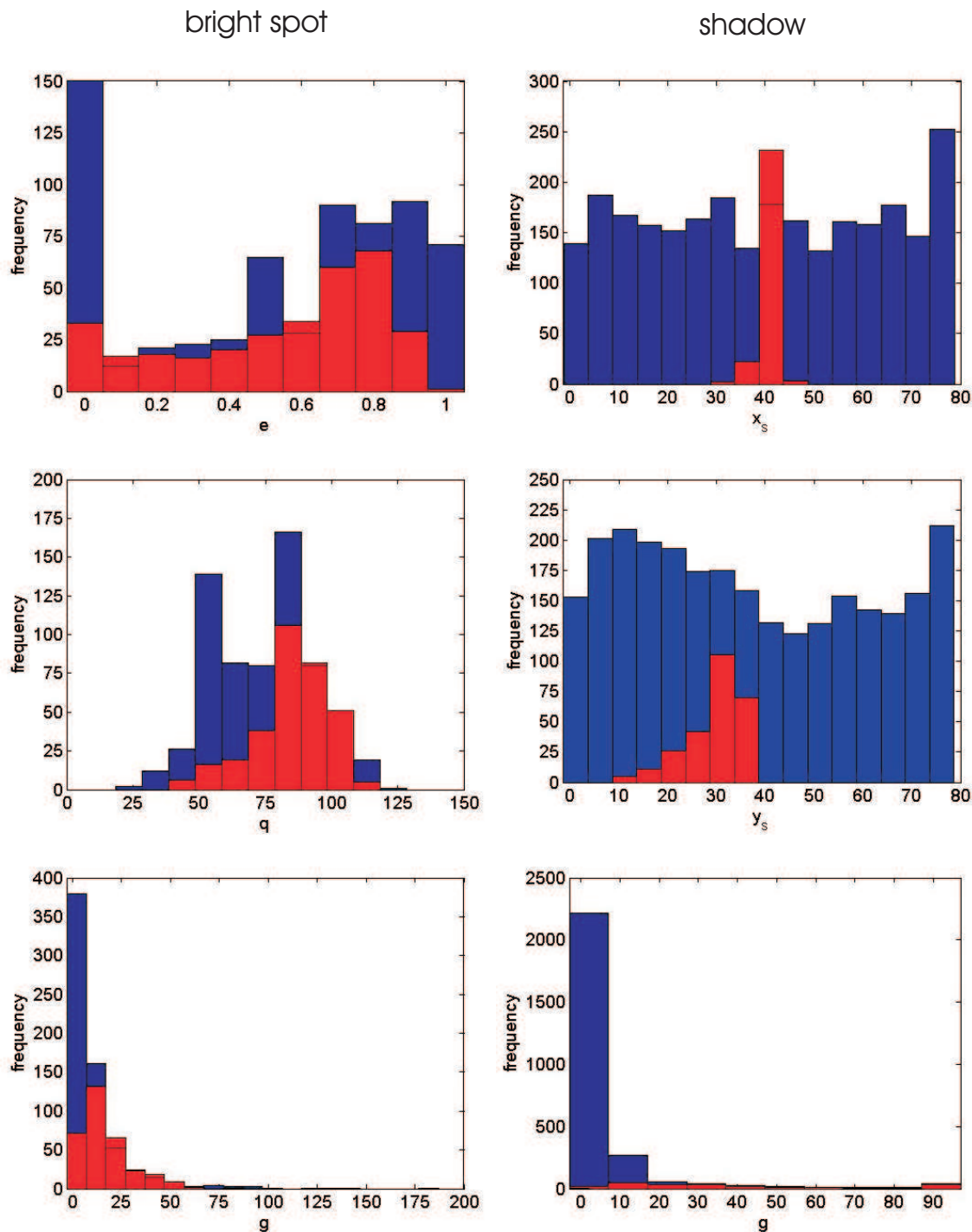


**Figure 6.6:** Histograms of dust devil parameters. The blue columns represent all derived data including the dust devil data, the red columns represent only the dust devil data. On the left side histograms for the bright spot parameters eccentricity  $\epsilon$ , quality parameter  $q$  (%) and size  $g$  (number of pixels). All bright spots obtained from all processed VIKING images go into these histogram data. On the right side histograms for the shadow parameters barycentre coordinates  $x_s$  and  $y_s$  (pixel coordinates) and size  $g$  (number of pixels). Only one VIKING image (f034b01) with a total of 26 dust devil shadows was used to create the shadow histograms. Otherwise the total data derived from the shadow search would cover the much less in number dust devil shadow data, if using all VIKING images.

The search for bright spots has been successful. Nearly every dust devil in the Viking images (together with additional non-dust devil features) has been detected. The interaction of the

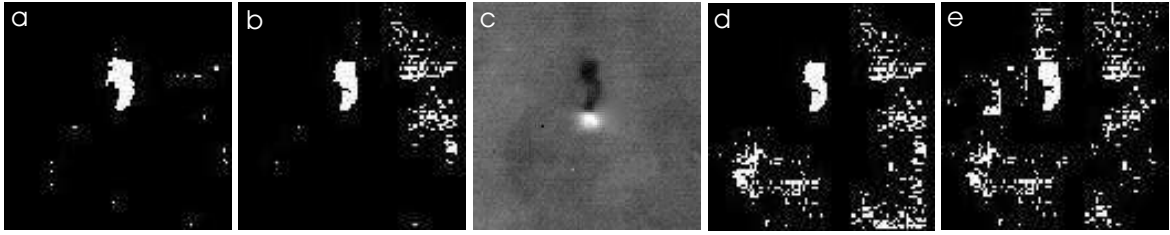


**Figure 6.7:** Search for brightness minima with  $n = -1.4$  for the shadow detection in a  $80 \times 80$  pixels cut-out. a) Search for absolute brightness minima. No grid was applied. b) A grid of  $2 \times 2$  squares (each  $40 \times 40$  pixels) was applied. c) The original VIKING image cut-out. d) A grid of  $3 \times 3$  squares (each  $26 \times 26$  pixels) was applied. e) A grid of  $4 \times 4$  squares (each  $20 \times 20$  pixels) was applied. The noise increases because the dust devil shadow is no longer the dominant brightness minima in the individual squares.

dust devil parameters is essential for the later classification and not one single parameter. Certainly if one parameter stands out in contrast to the usual values, it will likely lead to a wrong classification independently from other parameters. The three parameters size  $g$ , eccentricity  $\varepsilon$  and quality parameter  $q$  will be used for the description of the bright clusters representing the dust columns of dust devils.

#### 6.1.4 The Search for the Dust Devil Shadow

In order to extract the dust devils from other detected features, the shadow of a dust devil is an useful attribute. The same method as for the bright spot search is applied but this time searching for brightness minima. After applying the Hoshen-Kopelman algorithm the same geometry parameters are retrieved for the shadow. Not the entire image is processed now but a pixel array which was chosen large enough ( $80 \times 80$  pixels) so that it may include a potential shadow with the detected bright cluster in the image centre. The results suggest a value  $n = -1.4$ . Using this procedure a shadow is searched for every bright cluster which was left after the geometry analysis. As before dark single pixels and strict lines are discarded.

The entire image was divided in a grid for relative brightness maxima search. The smaller cutout around a bright spot was therefore first divided in several squares, too. Figure 6.7 shows an example for the shadow search with different grids. It is obvious that searching for absolute brightness minima is more efficient than subdividing the small image. This was the case for most dust devil shadows in the images. There is more noise included and the shadow is less well represented the more subdivided the image is.

Shadows and shapes were clearly identified in most cases. The shadow shows the projected vertical structure of the dust devil which may slope with height. It is very important to check the confidence of the parameter range in  $\varepsilon$  and  $q$  for the shadow to see if it can be used for classification.

In some dust devil cases a shadow was not extracted at all from the image. One reason is the already quite dark background where a dust devil is located, so that a shadow does not stand out. The other reason is the black frame on the right and left side of VIKING images. If a dust devil is too close to this frame, the  $80 \times 80$  pixels cut-out may include some columns of

the black boundary. A brightness minima search detects this frame since it is then the darkest feature.

A dust devil shadow will not be represented sufficiently and therefore detected if the dust devil is anyway located at the image border. Also a cut-out of  $80 \times 80$  pixels is not always possible. The software notices such a case and generates an appropriate cut-out. Missing pixels are artificially added later first for displaying reasons, to have all possible dust devil features in the middle of such quick-look plots (see Section 6.1.5 and Figure 6.9), and secondly for classification reasons. If we use the coordinates of the shadow as classification parameters, they should always be represented in the same frame of reference concerning the bright spot.

The most significant parameters for classification of the shadow are supposed to be the size  $g$ , the eccentricity  $\varepsilon$  (longish shadow), the coordinates  $x_s$  and  $y_s$  (barycentre) and the angle  $\phi$  of the cluster, because of the expected position of the shadow relative to the bright spot in dependency on the illumination conditions. The results after analysing the seven preselected VIKING images suggest the size  $g$  and the coordinates  $x_s$  and  $y_s$  as the parameters most useful for identification of a shadow. Figure 6.7b and 6.7d show how most of the retrieved black and white images look like after searching for a dust devil shadow. The shadow is the largest object ( $g \geq 10$ ) in the cut-out surrounded by other smaller clusters, located in the upper half of the image just in the middle of the x-axis giving values of  $x_s \approx 40$  and  $y_s \leq 40$ . Figure 6.6 shows histograms of shadow parameters on the right hand. The histogram for  $x_s$  demonstrates clearly the preference for the value of 40, expecting to find the shadow in the middle of the cut-out.  $y_s$  has values  $\leq 40$ , the shadow is therefore located in the upper half of the  $80 \times 80$  pixels image. The majority of clusters filtered during the dust devil shadow search have sizes less than 10 pixels. Larger sizes indicate mostly a dust devil shadow, but a verification can only be given in combination with the coordinates. The histogram was cut at  $g = 100$  for a better representation of the lower  $g$  values. There are several clusters with sizes larger than 100 pixels.

$\phi$  has also a preference to  $\pm 90^\circ$  but there are significant variances for smaller dust devils. This applies as well for the eccentricity. A small dust devil does not have a longish shadow, showing more an eccentricity of  $\varepsilon \approx 0$  with values of  $\pm 45^\circ$  for  $\phi$  due to that there is no preferred direction (semi-minor and semi-major axis almost equal) if the cluster is almost a circle.

The size  $g$ , both for the bright spot and the shadow, and the coordinates  $x_s$  and  $y_s$  and the angle  $\phi$  of the shadow are not conform with the intention to have size- and rotation-invariant parameters for classification. The bright spot size, however, serves as a filter to distinguish possible dust devils from the background noise mostly consisting of smaller clusters. This applies as well for the shadow cluster (Figure 6.7). The position of a shadow is an adequate parameter because for all 325 dust devils in VIKING images the shadow was found above the bright spot with the illumination from the bottom in the image. This is due to the fact that approximately 300 dust devils have been seen in early orbits (orbits 34-40), spanning a period of only seven Mars days and all were imaged at around  $40^\circ\text{N}$ ,  $210^\circ\text{E}$ . In addition, almost all dust devils have been seen between 1400 and 1600 hours local time, representing therefore the same illumination conditions for a specific point.

VIKING images are not oriented such as north is always up in the images. Where the shadow

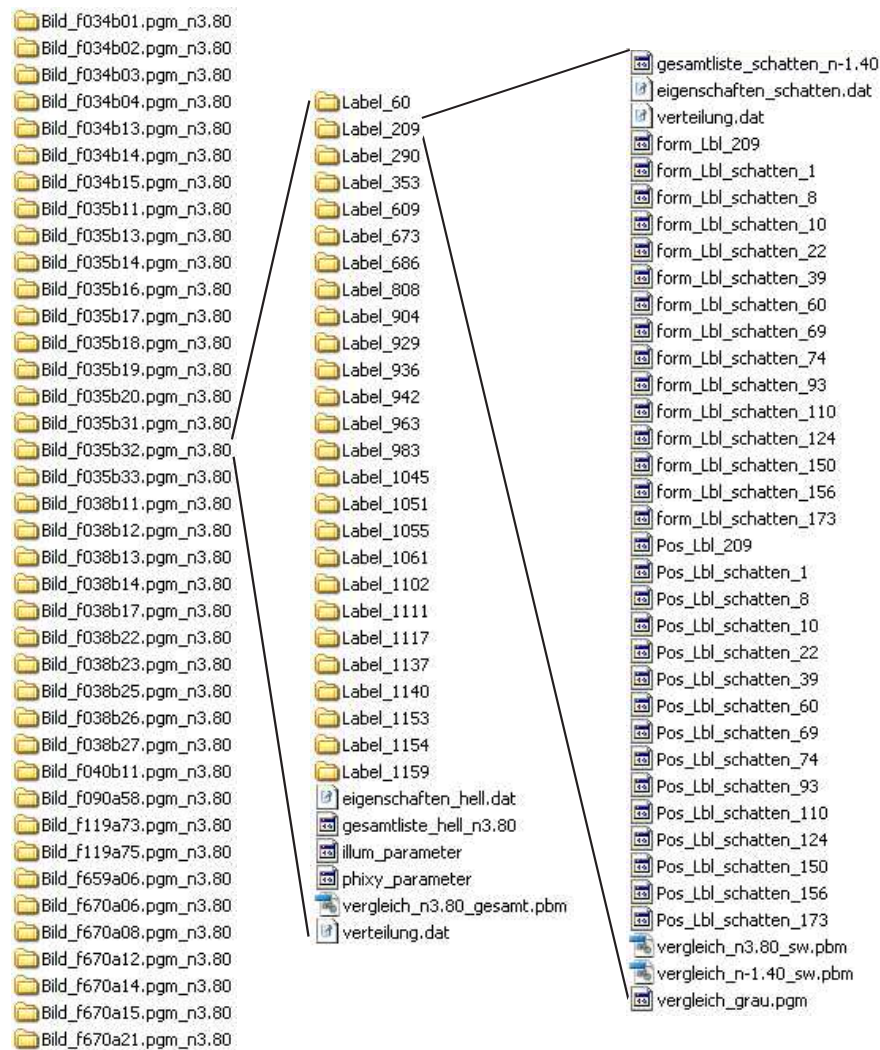


**Figure 6.8:** Structure of results for each processed image. On the left: one folder for each processed image is generated. In the middle: each image folder contains subfolders for each detected bright cluster plus additional auxiliary files. On the right: files containing the position and geometry parameters for the bright cluster and potential shadows plus auxiliary files and quick-look plots (last three files in this column). More details in the text.

is represented in the images, does not reflect the true illumination conditions at this surface point. The positions of the shadows of the remaining dust devils, not imaged within the above mentioned temporal and spatial frame, are maybe located above the bright spot by pure chance, depending on how the images were taken.

Dust devils in HRSC and MOC images will likely be imaged at different conditions so a solution has to be found for different directions of the dust devil shadow. The easiest and quickest way will probably be to rotate the input data derived from VIKING images at specific angles to provide datasets which simulate different illumination conditions.

### 6.1.5 The Structure of the Results

A lot of files and folders are generated during the processing of one image. The comparability of results of different images for the evaluation of the method is an essential requirement.

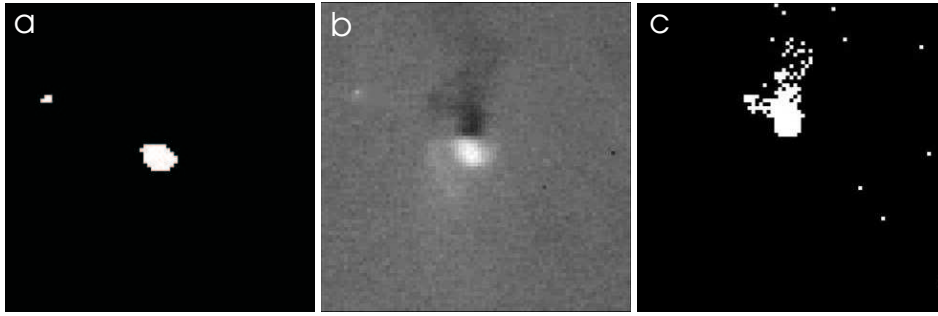


**Figure 6.9:** Quick-look plots of a dust devil seen in VIKING image f034b01. a) Black and white image (*vergleich\_n3.80\_sw.pbm*) with filtered pixels after the brightness maxima search. b) The original greyscale cut-out (*vergleich\_grau.pgm*) shows if a detected object is really a dust devil or not. c) Black and white image with filtered pixels after the brightness minima search (*vergleich\_n-1.40\_sw.pbm*).

It needs therefore an automated way to create filenames and a folder structure in a clear identifiable manner for a quick comparison. The structure of the results is presented here to help to understand the procedure how it is searched for dust devils and the later classification.

A folder is created for each processed image containing the image name (e.g. f034b01.pgm) and the chosen value for  $n$  for the brightness maxima search, here  $n = 3.8$  (Figure 6.8, on the left).

For every detected bright cluster a folder is generated called e.g. *Label\_60* where 60 is the label number given by the Hoshen-Kopelman algorithm. There are only folders left for whose clusters the geometry parameters could be computed. Other clusters are deleted (Figure 6.8, in the middle). The parameters of each cluster (label, semi-minor and -major axis  $a$  and  $b$ , eccentricity  $\varepsilon$ , angle  $\phi$ , quality parameter  $q$ , size  $g$  and the coordinates  $x_s$  and  $y_s$ ) are summarised in the file *eigenschaften\_hell.dat*. The file *gesamtliste\_hell\_n3.80* includes a list of all filtered pixels which fulfilled the brightness criteria. The two files *illum\_parameter* and *phixy\_parameter* are actually later added during the adjustment of the algorithm to HRSC and MOC images and will be explained in Section 6.2.2. The black and white image *vergleich\_n3.80\_gesamt.pbm* shows if the bright spots of dust devils are represented or not (see Figure 6.2, page 38). The frequency distribution of the cluster sizes are listed in *verteilung.dat* (see Figure 6.3, page 39).

Each label folder representing one detected bright cluster contains files produced during the search for an accompanying shadow (Figure 6.8, on the right). Two files are created for every potential shadow, e.g. *Pos\_Lbl\_schatten\_1* and *form\_Lbl\_schatten\_1* for a cluster labelled with 1, containing the pixel coordinates of a cluster and its geometry parameters. The pixel coordinates and geometry parameters for the bright spot are also located here as for example *Pos\_Lbl\_209* and *form\_Lbl\_209*, respectively. *gesamtliste\_schatten\_n-1.40*, *eigenschaften\_schatten.dat* and *verteilung.dat* are the analogues to the files with the almost same name created for the bright spot search. The three quick-look plots are *vergleich\_n3.80.pbm*, *vergleich\_n-1.40.pbm* and *vergleich\_grau.pgm* (Figure 6.9). The first two are black and white images representing filtered pixels for the bright spot and the shadow, respectively. The last image represents the cut-out of the original greyscale image for the verification if a detected object is really a dust devil or not.

## 6.2 Adjustment to HRSC Images

### 6.2.1 General Configuration

HRSC produces due to the imaging technique long image strips with several ten thousand lines (Figure 6.10). The width is also highly variable with mostly several thousand pixels. It is necessary to cut the long images in manageable sizes. VIKING images have a fixed size of  $1056 \times 1204$  pixels. The resolution of dust devil images was in most cases  $\sim 70$  m/pixel. HRSC images have usually a resolution of 12.5 m/pixel. The question is now which image sizes at which resolution shall be generated to retrieve dust devil parameters which are in a comparable range to the VIKING parameters? This is very important since a later correct classification depends on these values and VIKING data are used as the database for classification training.

Several configurations have been tested, and although some aspects are explained here, testing was also done after applying the classifier, to see how it handles the different representations of the dust devils (see Section 7.3). The advantage of HRSC is definitely its high resolution. However, if it is possible to detect very small dust devils now, there is the difficulty that some dust devils are too large to be well represented. A large bright spot will cover a good portion of the image cut-out, raising the mean brightness and therefore no relative brightness maxima are left which can be filtered. A priority has to be given to those dust devil sizes which are expected to be seen most of all. A resolution of 25 m/pixel was chosen to be adequate, since dust devil diameters of several hundreds of metres are most common resulting in approximately 8 to 16 pixels for the diameter with this chosen resolution.

By analogy to the processing of VIKING images the image cut-outs are  $1200 \times 1200$  pixels for HRSC images. The algorithm can handle this size without problems. Choosing a larger square led sometimes to too many filtered pixels for the defined arrays in the software. Since the HRSC image size is highly variable, adjusting a grid of  $1200 \times 1200$  pixel squares will lead to an image border on each side which will remain unprocessed. Dust devils which are located at the image border will then not be detected. Since HRSC images are geometrically corrected, i.e. north is at the top of the image and they are map-projected to a MOLA DTM (digital terrain model), the image border is not a clear line leaving a black frame around the original greyscale data (Figure 6.10). Several cut-outs are then totally black. The software notices that no clusters are found and jumps to the next square. Due to the black frame, the grid of  $1200 \times 1200$  pixel image cut-outs will rather be centred on the real grey-scale

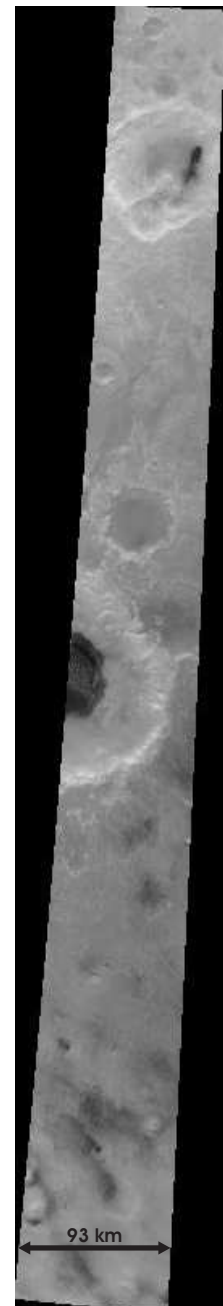


*Figure 6.10: Example of a long HRSC image strip (orbit 2225).*

image data than covering the black area. Dust devils at the image border should therefore be included in the cut-outs in most cases. If the black frame is part of an image cut-out, it may prevent the filtering of dust devil shadows, because it is then the dominant dark object. So far, the cut-outs are directly connected to each other, there is no overlap. Dust devils at the edges of these cut-outs are also difficult to detect. A later improvement could be to overlap the cut-outs to avoid this second border problem.

Depending on the image size, there are usually between 30 to over 100 cut-outs. Extreme cases had over 700 cut-outs. This has an impact on the processing time. The more cut-outs and the more features are detected in an image, the longer does it take. A duration of 1 to 3 hours is acceptable as it was in most cases. A reduction of the image resolution would lead to a significant decrease in computation time.

There are four constants in the algorithm: the factor 64 (square size for the relative brightness maxima search), the factor 80 (square size for the absolute brightness minima search), the factor 3.80 (for filtering the bright pixels) and the factor -1.40 (filtering the dark pixels). It was supposed and later approved that no changes are necessary to the constants 3.80 and -1.40 for filtering pixels. HRSC images are as well greyscale images with in principle the same representations of dust devils and no contrast enhancements are applied.

If the values of 64 and 80 for the square sizes are sufficient depends on the dust devil sizes and the information available in the image. Due to the much higher resolution much more details are seen in the HRSC images. If the squares are chosen too large, too much pixels are filtered and the object we are interested in will not be worked out properly. Smaller divisions would discard larger dust devils. After some testing it was decided to keep the old values of 64 and 80 pixels for the squares for pixel filtering with a resolution of 25 m/pixel. There will still be some dust devils too large to retrieve usable parameters of the bright spot in a  $64 \times 64$  pixel window and the shadow in full length in a  $80 \times 80$  pixel cut-out. Likewise there are still dust devils too small for detection. Nevertheless, in the classification chapter it will be demonstrated that most of the typical dust devils are detected using this configuration.

### 6.2.2 Illumination Conditions

The shadows of all dust devils are oriented in an upward direction in the VIKING images which build our database. This is due to the fact that almost all images containing dust devils cover Arcadia Planitia, taken within only seven days at 1500 to 1530 hours local time. The same illumination conditions in these images provide the same direction of the shadows of dust devils. The location of a shadow is therefore a suitable parameter for classification. There are also other shadow directions possible, especially for HRSC images. The information is needed where a shadow is expected in a Martian image so that a classifier can evaluate if a detected object can be considered as a dust devil shadow. The required complements and add-ons for HRSC (and later MOC) have also been implemented in the software for VIKING although it was not necessary, but the same subroutines are used for all mission images.

The illumination conditions in an image are dependent on the position of Mars and the Sun, the *sub\_solar\_point* and where a camera is pointed to on the Martian surface at a specific time.

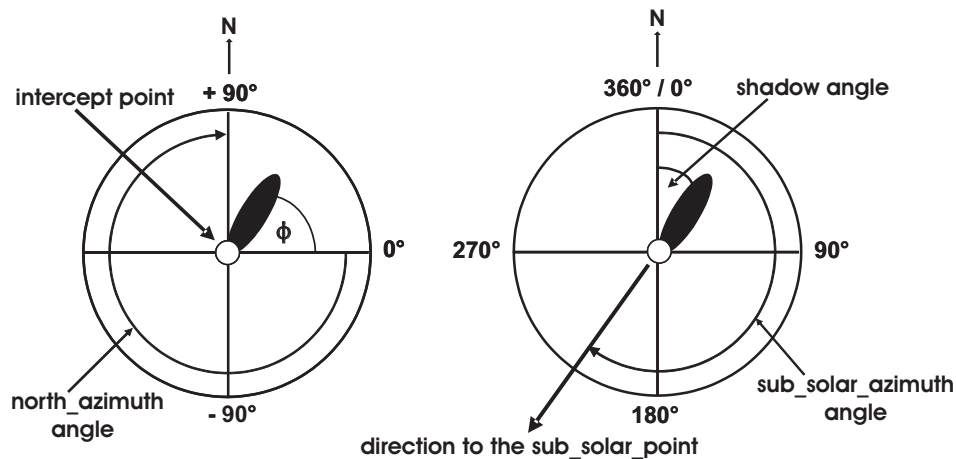


**Figure 6.11:** Illustration of the illumination conditions at a possible dust devil location. Left figure: The white area in the middle represents the bright spot of a dust devil, the black ellipse its shadow. The dust devil location is regarded as the intercept point where the camera points to at a specific time. The angle  $\phi$  is between the semi-major axis of the shadow and the x-axis (line to the right), and has values between  $\pm 90^\circ$ . From the x-axis in a clockwise direction extends the north\_azimuth angle, indicating the northward direction. Right figure: The sub\_solar\_azimuth angle indicates clockwise the direction to the sun from the north. Opposite of the sun direction are the dust devil shadows located. The north\_azimuth, the shadow angle and the sub\_solar\_azimuth have values between  $0^\circ$  and  $360^\circ$ .

The *sub\_solar\_point* is that point on the Martian surface where a line from the body centre to the sun centre intersects the surface (sun is perpendicular to this surface point). All necessary informations about the position of the bodies, the spacecraft and the mounted camera are provided via a software called SPICE. SPICE is a software system produced by NASA's Navigation and Ancillary Information Facility (NAIF)<sup>1</sup> that provides the capability to easily combine accurate space geometry and event data into mission analysis, observation planning, or science data processing software. The software, mostly in the form of subroutines, is used to read SPICE files including relevant information and e.g. the altitude of a spacecraft or the illumination angles can be computed.

The time when an image was taken is the essentially needed information beside SPICE data files for our illumination problem. The VIKING image label was used so far only for the retrieval of the size of the image and the label itself. The same was done for the HRSC images. Now it is searched for the start and stop time of an image for HRSC, and the image time for VIKING. There is only one time stamp provided for the rather small VIKING images compared to the long strips of HRSC. Two illumination angles will be retrieved for the start and the end of an HRSC image, indicating a range of possible dust devil shadow locations.

Since we have two VIKING orbiters and two cameras on each orbiter, the software is also looking for two keywords giving the spacecraft and instrument name. Images can be taken by the VIKING Orbiter 1 or 2, and by the camera A or B. The ND channel is always used to process an HRSC image, so there is no additional information required.

The intercept point where the camera is looking at on the surface has to be calculated. All necessary parameters can be computed for this point at a specific time. First the so-

<sup>1</sup><http://naif.jpl.nasa.gov/naif/>

*lar\_incidence\_angle* is calculated. This is the angle between the local vertical at the intercept point (on the surface) and a vector from the intercept point to the Sun. The height of dust devils are retrieved using this value and the length of the cast shadow. The local time and season are also important for the interpretation of the dust devil occurrence and are retrieved using SPICE as well.

The *sub\_solar\_azimuth* is the angle between a line extending from the intercept point in northward directions and the line from the intercept point to the *sub\_solar\_point* (Figure 6.11). This is the essential angle for the estimation of the dust devil shadow direction. Since HRSC images are all adjusted in a northward direction (north is up in the images) there is no problem in applying the *sub\_solar\_azimuth angle*. This is not the case for VIKING images. North can be everywhere in the image. For this reason the *north\_azimuth* element has to be computed. The *north\_azimuth* provides the value of the angle between a line from the image centre to the north pole and a reference line in the image plane. The reference line is a horizontal line from the image centre to the middle right edge of the image (Figure 6.11). Summing up the *sub\_solar\_azimuth* and the *north\_azimuth* for VIKING images leads to the direction of the *sub\_solar\_point* seen from the image centre (image centre is equal to the intercept point for VIKING images). The values of the angles increase in a clockwise direction. All illumination values, the *solar\_incidence\_angle*, the *sub\_solar\_azimuth*, the *north\_azimuth* and the local time and season are written in the file *illum\_parameter* (see Figure 6.8, page 45).

The factor  $180^\circ$  has to be added to the angle of the *sub\_solar\_point* to get the direction of the shadow (Figure 6.11). The retrieved value is converted so that it can be compared to the derived shadow parameters, the orientation angle  $\phi$  and the coordinates  $x_s$  and  $y_s$ . The computed values are written in the file *phixy\_parameter* (see Figure 6.8, page 45). Checking up this file leads to the selection of an adequate shadow classifier. The shadows of dust devils should have approximately the same parameter values as those written in the file so that they are considered as a shadow of a dust devil.

### 6.3 Adjustment to MOC Images

MARS GLOBAL SURVEYOR MOC images are available through CD-ROMs at the Institute of Geophysics and Meteorology or via the internet<sup>1</sup>. Data from other missions including MARS EXPRESS and VIKING are available on this site as well. MOC images are in the compressed .img-format which can be extracted to the readable .pds-format, which is the standard archive format for images from planetary missions. PDS stands for Planetary Data System. Since the labels of these images have their own format different from the available VIKING and HRSC images in the VICAR format, a new software also installing a PDS library for reading the image label had to be written.

For our purposes the .pds-image is changed to a .pgm-image as it was done for VIKING and HRSC images using the information about the image size in the label. Two time stamps are delivered with an MOC image, the start time and the stop time of an image, providing also a

---

<sup>1</sup><http://pdsimg.jpl.nasa.gov/Missions/index.html>

range of possible values for the shadow direction. The camera consists of two instruments, the narrow (NA) and the wide angle (WA) camera. The *instrument\_id* have to be readout if it is NA or WA. If the WA camera is used it has to be distinguished between the red and the blue filter. These informations are necessary for the right computation of the surface point where the camera points to on the Martian surface. This is important for the correction calculation of the illumination angles.

The further processing is analogous to the VIKING and HRSC image processing. The illumination angles and the local time and season are retrieved. MOC images are also not adjusted in a northward direction so the *north\_azimuth* has to be computed as well. Before applying the derived angle  $\phi$  and the coordinates  $x_s$  and  $y_s$  of possible shadows to a MOC image, it has to be investigated if the image has to be flipped left-to-right. After flipping the image the computed parameters should be in agreement with what is seen in the image. The flipped image is used for further processing.

The image sizes and the resolution are highly variable for MOC images, making an automated processing difficult. The resolutions of NA images are a few metres per pixel, suggesting a decrease of resolution for parameter retrieval, whereas WA images have a resolution of mostly about 240 m/pixel. The size and shape range from long strip-like to small rectangular images. It is therefore not clear in advance if the original image has maybe to be cut in smaller pieces so the software can handle it. It seems to be necessary to have a look at the images before they are processed. There is no software provided for MOC images but a decompressing software. If the resolution shall be reduced or the image shall be cut in smaller ones, another image processing software has to be used or an own code has to be written. This leads to a lot of handwork because each image has to be treated separately. So far the images are let as they are. If the results are not satisfying after applying the pattern recognition and classification software to them, it will be decided thereafter which changes are required.



---

## CLASSIFICATION OF DETECTED PATTERNS

---

There are an increasing number of classifying methods and they are getting more complex since pattern recognition has become very popular in the last years. It is not easy to find an adequate classifier for a set of data. It was searched for a free available software, which provides multiple methods for analysing the retrieved dust devil data and investigating which classifier may be the best one for our problem.

### 7.1 The LNKnet Library

The LNKnet library was developed at the Massachusetts Institute of Technology (MIT), Lincoln Laboratory, within the Information Systems Technology Group (*Lippmann et al.* [1993]; *Kukolich and Lippmann* [2004])<sup>1</sup>. The acronym LNK stands for the first initials of three principal programmers (Richard Lippmann, Dave Nation, and Linda Kukolich). LNKnet includes more than 22 neural network, statistical, and machine learning classification, clustering, and feature selection algorithms (Figure 7.1). The library can run under different operating systems such as Solaris UNIX, Red Hat Linux and Microsoft Windows and provides beside executables, documentation and sample datasets also the source code. This makes the LNKnet library very flexible and adaptable for the specific needs and problems of a user.

The LNKnet pattern classification software can be accessed via three different approaches. The first approach is to use the graphical user interface (GUI) to run experiments. A second approach creates automatic batch jobs, which run classification programs from a command line or in shell scripts. The third approach uses the LNKnet GUI to produce C source code which can be implemented in already existing application programs. This feature of LNKnet allows trained classifiers to be run on any computer that has a C compiler (*Kukolich and*

---

<sup>1</sup><http://www.ll.mit.edu/IST/lknnet/>

	Supervised Training	Combine Unsupervised-Supervised Training	Unsupervised Training (Clustering)
<b>Neural Network Algorithms</b>	Back-Propagation (MLP) Hypersphere Classifier Perceptron Committee	Radial Basis Function (RBF) Incremental RBF Learning Vector Quantizer (LVQ) Nearest Cluster Classifier Fuzzy ARTMap Classifier	
<b>Statistical and Machine Learning Algorithms</b>	Gaussian Linear Discriminant Gaussian Quadratic K-Nearest Neighbor Binary Decision Tree Parzen Window Histogram Naive Bayes Support Vector Machine	Gaussian Mixture Classifier - Diagonal/Full Covariance - Tied/Per-Class Centers	K-Means Clustering EM Clustering Leader Clustering Random Clustering
<b>Feature Selection Algorithms</b>	Linear Discriminant (LDA) Forward/Backward Search		Principal Components (PCA)

**Figure 7.1:** Overview of the current algorithms implemented in the LNKnet library. Adapted from <http://www.ll.mit.edu/IST/lnknet/>.

Lippmann [2004]).

Figure 7.1 shows the algorithms implemented in the LNKnet library. The algorithms include classifiers trained with labelled data (supervised learning), classifiers that use clustering to initialise internal parameters and then are trained further (combined unsupervised-supervised), and clustering algorithms trained without supervision using unlabelled training data (unsupervised). Linear discriminant (LDA) and principal components analyses (PCA) are used to reduce the number of input features. Forward and backward searches provide a selection of a small number of features from among all existing features which shall yield the best classification. These last two algorithms deal with the problem of dimensionality.

LNKnet produces several plots and tables when training a classifier. Decision region, histogram and structure plots are provided, as well as plots showing how the error rate or the cost functions vary with time/training. After an experiment is run, confusion matrices [Kukolich and Lippmann, 2004; Zabel, 2005] and tables of the error rate for each class and overall error rates are shown to illustrate how well the classifier performs.

Only some of the classifiers and methods which were used during testing of the VIKING dataset will be explained in more detail. The description of all classifiers and methods can be found in Kukolich and Lippmann [2004].

## 7.2 Classification of the VIKING Dataset

One of the main problems of pattern recognition and classification is the dimensionality of the input space. The more parameters are retrieved the better an object can be described, the more complex, however, is the feature vector, too. A classifier has then to deal with higher dimensions which make a correct classification more difficult. It was therefore decided to separate the classification of the bright spot and the shadow of the dust devils, so that not 6-dimensional but two 3-dimensional input spaces (according to the selected parameters) have

to be handled. This is also convenient with regard to the design of the pattern recognition software (see Figure 6.8, page 45), where first the bright spot parameters are retrieved, then it is looked for a potential shadow for each bright cluster.

## 7.2.1 Classification of the Dust Devil's Bright Spot

### 7.2.1.1 Separation of Data

It is useful to separate the available data in training, evaluation and testing data. Of course, the majority of the data should be in the training data, so that a classifier has enough examples it can be trained on. Testing data are not presented to the classifier during the training phase. The trained classifier will react on this data in its current status. The testing phase will actually show how well the classifier performs. Evaluation data are necessary because it is possible to design a classifier that provides a low error rate on training data but that does not provide a similar low error rate on other data collected from the same source [Callan, 2003]. First the classifier will be trained using training data. Then the trained classifier is tested using evaluation data. If the results are not satisfying, the classifier structure is changed and the training is repeated. Test data are used for the final test. This approach uses training data to adjust trainable parameters and evaluation data to adjust the classifier sizes and complexity to provide good generalisation.

[Kukolich and Lippmann, 2004] suggest if thousands of patterns are available to split the database into three sets: training, evaluation and testing data. Usually 60% of the patterns are assigned to training data, and each 20% to evaluation and test data. If fewer patterns are available (on the order of hundreds of patterns), the dataset is split into only training (60% of patterns) and test data (40% of patterns). If only tens of patterns are available, only training data is used. In both cases where no separation in three parts is possible, 10-fold cross validation is used on the training data. N-fold cross validation splits the data into N equal-sized folds and tests each fold against a classifier trained on the data in the other folds.

Summarising the results after the bright spot search in 38 VIKING images, we have 2334 patterns. This dataset includes 325 dust devils and 2009 non-dust devil features, giving a ratio of 1:6.2. The number of patterns is large enough to divide them in training, evaluation and test data. The dataset was divided in three parts not considering from what image the data is or how well the dust devils are represented in the different parts. It was made sure, however, that the ratio of dust devils to non-dust devil features is roughly the same in training, evaluation and testing data.

### 7.2.1.2 Normalisation and Feature Selection

The LNKnet library provides two powerful features. The ability to normalise the input data before it is presented to a classifier, and to use only a subset of input parameters for classification. Three methods are available for normalisation. Simple normalisation rescales each input feature (e.g. the eccentricity  $\varepsilon$  or the size  $g$ ) independent from the other features so that a mean of 0 and a variance of 1 is retrieved. This compensates for the differences in

Class	Label	a	b	e	phi	q	g	x_s	y_s
0	177	1.06	1.06	0.00	45.00	56.4	2	310.50	373.50
0	178	1.06	3.04	0.94	8.52	69.1	7	315.14	373.29
0	185	1.28	12.81	1.00	87.77	58.2	35	1178.69	393.74
1	186	2.46	3.25	0.66	10.67	91.6	24	216.33	384.12
0	195	1.86	1.86	0.00	45.00	55.1	7	775.43	400.57
0	204	1.05	1.52	0.73	-75.13	80.1	4	899.50	403.75
0	208	1.06	1.06	0.00	-45.00	84.6	3	1120.33	404.67
0	217	0.76	62.38	1.00	89.84	77.5	121	1178.93	476.07
1	218	1.77	2.93	0.80	-4.58	85.7	16	673.94	420.81
0	224	2.81	2.84	0.14	-40.50	63.9	17	1133.65	450.88
0	226	1.06	1.06	0.00	45.00	84.6	3	801.33	451.33
1	238	1.65	3.78	0.90	-5.40	96.9	19	269.74	496.11
1	242	2.25	2.60	0.50	-24.70	86.8	16	292.50	507.50
0	245	1.66	2.15	0.64	18.22	89.5	10	139.70	518.20

**Figure 7.2:** A part of a training file showing the parameters retrieved during the brightness maxima search. The first line was added for displaying reasons to identify the columns. The first column indicates the class: 0 for non-dust devils, 1 indicates a dust devil's bright spot. Label is the number given by the Hoshen-Kopelman algorithm. Each line represents a 'pattern' or 'sample' as it is referred to in the text. More details in the text.

the means and variances of the input dimensions [Kukolich and Lippmann, 2004; Callan, 2003]. The principal components analysis (PCA) rotates the input space so that the direction of the greatest variance is the first dimension (first component). It is often used to reduce the number of input dimensions if only the most important components are selected [Duda et al., 2001] and the data patterns are then displayed in the new coordinate system. The last method, linear discriminant analysis (LDA), can only be performed when classes and class means can be modelled using Gaussian distributions. It was therefore not used, since our data show clearly no normal distribution. PCA was also tested, but with a simple normalisation the best results were rendered during feature selection.

Our dust devil feature vector consists for both objects, the bright spot and the shadow, of nine parameters. Figure 7.2 shows the nine parameters for each detected relative brightness maxima cluster in an image: first the label is written, the semi-minor axis  $a$ , the semi-major axis  $b$ , the eccentricity  $\epsilon$  ( $e$ ) and the angle  $\phi$  ( $\text{phi}$ ) then represent the parameters of the best-fit ellipse, followed by the quality parameter  $q$ , the size  $g$  and the barycentre coordinates  $x_s$  and  $y_s$ . The class numbers, 0 for non-dust devil objects, 1 for a bright spot of a dust devil, were added so that a supervised training can be conducted.

Needless to say that not all of these nine parameters like the label or the coordinates are useful for classification. Also, the ellipse parameters are interdependent so not all can be used. In the previous chapter the parameters  $\epsilon$ ,  $q$  and  $g$  were thought to be most valuable for classification of the bright spot. This will be checked by using the feature selection tool provided by the LNKnet library.

There are three ways of creating a favourite feature list. In a forward search, each parameter is tried singly and the feature which gets the best classification rate (according to the labelled training data) is selected as the first feature. The remaining parameters are tested in combination with the first feature and the best of them is added as the second feature. Each feature is processed this way creating a list with a sequence of parameters best for classification until no parameters are left.

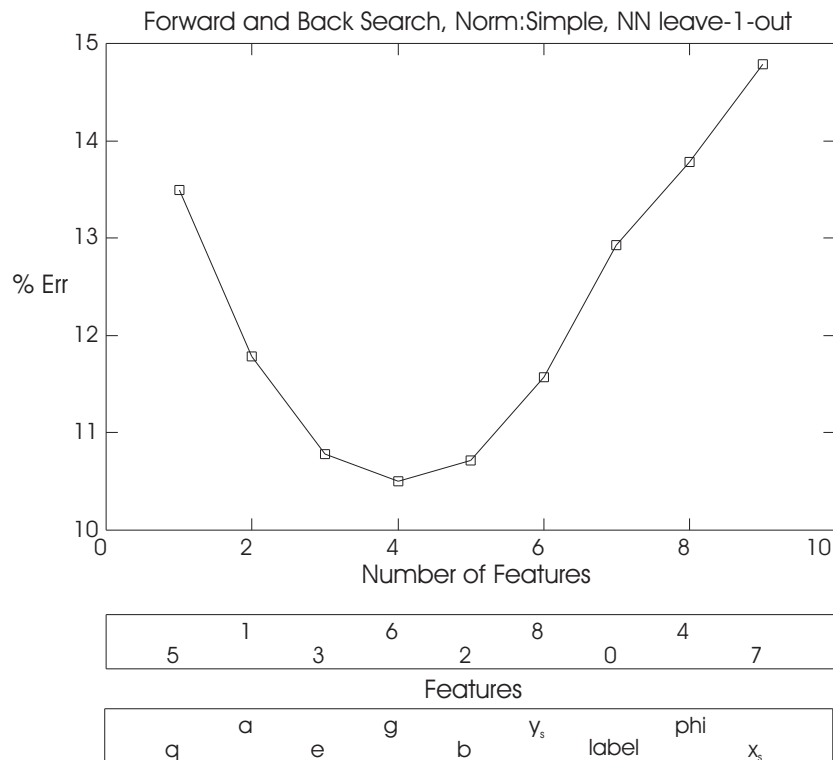


**Figure 7.3:** Error rate for the forward and backward search, using simple normalisation and the nearest neighbour classifier. The parameters 5( $q$ ), 1( $a$ ), 3( $\epsilon$ ) and 6( $g$ ) provide the lowest error for the right classification.

The backward search starts with all features trying to leave each one out. The parameter which the classifier did best without is selected as the last feature. Parameters are taken away until none are left. The idea is that there is a set of parameters which perform well when they are combined but do poorly individually. This combination would not be found if only a forward search is used.

A combination of both methods is the third option, the forward and backward search. First the program starts searching forward until it has two features. Then it searches for one to take away. It is continued by adding two and taking away one, until all parameters are listed. This method will find some interdependencies in the input features which can not be found by the two other methods [Kukolich and Lippmann, 2004].

The testing of the selected features is done via classification. The algorithm can either be a nearest neighbour algorithm with leave-one-out cross validation or any other classifier included in the LNKnet library with N-fold cross validation. Nearest neighbour classifiers work with the idea that a pattern is probably of the same class as its nearest neighbour patterns. Distances are therefore computed between all patterns. In leave-one-out cross validation, the stored training patterns are tested one at a time against a model containing all but the single test pattern. N-fold cross validation splits the data into  $n$  folds testing each fold against a classifier trained on the data in the other folds.

Feature selection was done with the training dataset for the bright spot once normalised, once without normalisation. It was quite obvious that the search performs much better with a simple normalisation of the data. All three search algorithms have been tested using the nearest

neighbour leave-one-out cross validation classification. There are not much differences in the overall error rate from 10.5% to 11.0% for the right classification. The parameters which were selected in most cases as the best for classification are in this sequence the quality parameter  $q$ , the semi-minor axis  $a$ , the eccentricity  $\varepsilon$ , and the size  $g$ . Figure 7.3 shows the error rate for the forward and backward search. Since  $a$  and  $\varepsilon$  are interdependent, only one parameter should be selected. The feature selection provided an error rate of 11.8% for the combination of parameter 5 and 1 ( $q$  and  $a$ ), and 12.1% for the combination of 5 and 3 ( $q$  and  $\varepsilon$ ). The eccentricity was previously thought to be a valuable parameter and was therefore chosen. The later classification showed that it had no major influence choosing  $\varepsilon$  instead of  $a$ , revealing even a lower error rate in parts.

The expectations which parameters are the best ones for classification of the bright spot of dust devils have been confirmed by the feature selection tool of the LNKnet library. The parameters eccentricity  $\varepsilon$ , quality parameter  $q$  and size  $g$  are chosen to train a classifier.

### 7.2.1.3 Classifier Testing

The LNKnet library provides several classifiers. Many of them have been tested on the datasets to see how they react on the dust devil data. Not all tested classifiers and their results will be presented here, but an assortment which shows different characteristics and classifying results, including the later selected trained classifier.

### Neural Network Classifier - Multi-Layer Perceptron

A multi-layer perceptron (MLP) is a widely used neural network classifier. Mapping is performed adaptively and this learning ability is a great advantage. A single-layer perceptron is composed of one layer of ‘neurons’ or nodes. The input is received by all nodes of this layer, but there are no connections between the nodes [Lee, 1989]. Each node refers then to

one class. A more powerful network is an MLP, which is often implemented in two layers (Figure 7.4).

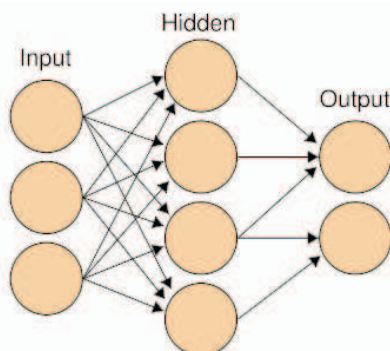


**Figure 7.4:** A two-layer perceptron formed by the hidden and the output layer.

The first layer, known as hidden layer, receives the weighted inputs, whereas the second layer, called the output layer, receives the inputs from the nodes. Such a system is called a feed-forward network [Callan, 2003]. It estimates the a posteriori class probabilities of an input pattern by using sigmoid functions as threshold functions. Decision regions are created by positioning hyperplanes produced by these sigmoid functions in the input space [Kukolich and Lippmann, 2004]. The planes are combined to form decision regions. The weighted connections between the layers of the MLP specify the positions of the planes and their combinations.

Error Report - alle_hellmlp.err.train							
Class	Patterns	# Errors	% Errors	StdDev	RMS Err	Label	
0	24440	704	2.88	( 0.1)	0.155	noDD	
1	3560	1842	51.74	( 0.8)	0.627	DD	
Overall	28000	2546	9.09	( 0.2)	0.266		
Error Report - alle_hellmlp.err.eval							
Class	Patterns	# Errors	% Errors	StdDev	RMS Err	Label	
0	404	18	4.46	( 1.0)	0.171	noDD	
1	63	22	34.92	( 6.0)	0.519	DD	
Overall	467	40	8.57	( 1.3)	0.249		
Error Report - alle_hellmlp.err.test							
Class	Patterns	# Errors	% Errors	StdDev	RMS Err	Label	
0	384	6	1.56	( 0.6)	0.135	noDD	
1	83	47	56.63	( 5.4)	0.650	DD	
Overall	467	53	11.35	( 1.5)	0.300		

**Figure 7.5:** The results of the multi-layer perceptron classification in the configuration of  $3 \times 20$  epochs, 20 nodes in one hidden layer, and a step size of 0.4 for weight updating. At the top the training results are seen, in the middle the results of the evaluation, and at the bottom the test results.

Back propagation is very useful to train a multi-layer network. The weighted connections between the input and the hidden layer (Figure 7.4) are first initialised by random weights. Back propagation will update these weights to assign the given inputs to the desired outputs as given in the training data file. The update is done using a gradient descent algorithm to minimise the error between the actual output of the network and the desired class for a pattern. The output error is computed by a cost function. The patterns in the training data file are repeatedly presented to the classifier until a determined number of iterations are reached or the reduction in error is as minimal as desired [Callan, 2003].

The most important options which have to be set to use the MLP as classifier are the number of times (epochs) the data are examined, the number of hidden layers and the number of nodes in each hidden layer, and the step size for the weight updating. The step size is a multiplier applied to the gradient when the weights are updated [Kukolich and Lippmann, 2004]. Further options concern weight definitions, available cost functions for the back propagation and different sigmoid functions for the nodes of the layers. These last options are usually not changed and it is advised to use the standard configuration [Kukolich and Lippmann, 2004]. Standard weight definitions are a constant step size used for all weights, which are updated after each trial. Trial means after each presented pattern of the training file and not after each epoch (total training file examined). The squared error function is used as the cost function. The standard sigmoid function goes from 0 to 1 with an output of 0.5 for an input of 0.

Testing was started with the standard configuration provided by the LNKnet library: 20 epochs (cycles through the training file), one hidden layer with 25 nodes, and a constant step size of 0.2 for the weight updating. The results were not satisfying, most obvious that

Error Report - alle_hellmlp.err.train						
Class	Patterns	# Errors	% Errors	StdDev	RMS Err	Label
0	24440	797	3.26	( 0.1)	0.156	noDD
1	3560	1801	50.59	( 0.8)	0.633	DD
Overall	28000	2598	9.28	( 0.2)	0.269	
Error Report - alle_hellmlp.err.eval						
Class	Patterns	# Errors	% Errors	StdDev	RMS Err	Label
0	404	19	4.70	( 1.1)	0.188	noDD
1	63	21	33.33	( 5.9)	0.492	DD
Overall	467	40	8.57	( 1.3)	0.251	
Error Report - alle_hellmlp.err.test						
Class	Patterns	# Errors	% Errors	StdDev	RMS Err	Label
0	384	10	2.60	( 0.8)	0.156	noDD
1	83	45	54.22	( 5.5)	0.622	DD
Overall	467	55	11.78	( 1.5)	0.298	

**Figure 7.6:** The results of the multi-layer perceptron classification in the configuration of  $3 \times 20$  epochs, 20 nodes in one hidden layer, and a step size of 0.6 for weight updating. At the top the training results are seen, in the middle the results of the evaluation, and at the bottom the test results.

further training is needed. The LNKnet library provides an option to continue the training. The training data will then be examined another 20 epochs. This option can be repeated until the results are more satisfying. A configuration of  $3 \times 20$  epochs, 20 nodes in one hidden layer, and a step size of 0.4 produced the results seen in Figure 7.5.

The training resulted in a quite good classification of the no-dust devil patterns (Label noDD, class 0) with an error rate of 2.88%, but only every second dust devil was correctly classified with an error rate of 51.74% (Label DD, class 1). This gives a total error rate of 9.09% which is slightly below the error rate obtained during the feature selection. If the classifier is tested using the evaluation data, the results are much better, two third of the dust devils are correctly classified (Figure 7.5, in the middle). 17 of 22 misclassified dust devils have a size  $g < 10$  pixels. This is consistent with what was already seen in the size distribution of clusters (see Figure 6.3, page 39). Cluster sizes below 10 pixels are mostly treated as noise.

The results of the test data show a similar behaviour as those of the training data. The misclassification rate of no-dust devil patterns are very low while dust devil misclassification has an error rate of 56.63% which leads to a total error rate of 11.35%. As in the evaluation case 33 of 47 misclassified dust devils have a size of less than 10 pixels. Other misclassified dust devil patterns seem to have too low  $q$  values or too high eccentricities  $\varepsilon$ .

The aim is to reduce the error rate of dust devil patterns but to keep the good classification rate of no-dust devil patterns. Priority was given in general to configurations which produce little false classification of no-dust devil patterns and accept a higher misclassification of dust devils. This was chosen to reduce the number of false positive detections and accept that maybe small or strange looking dust devils are not detected.

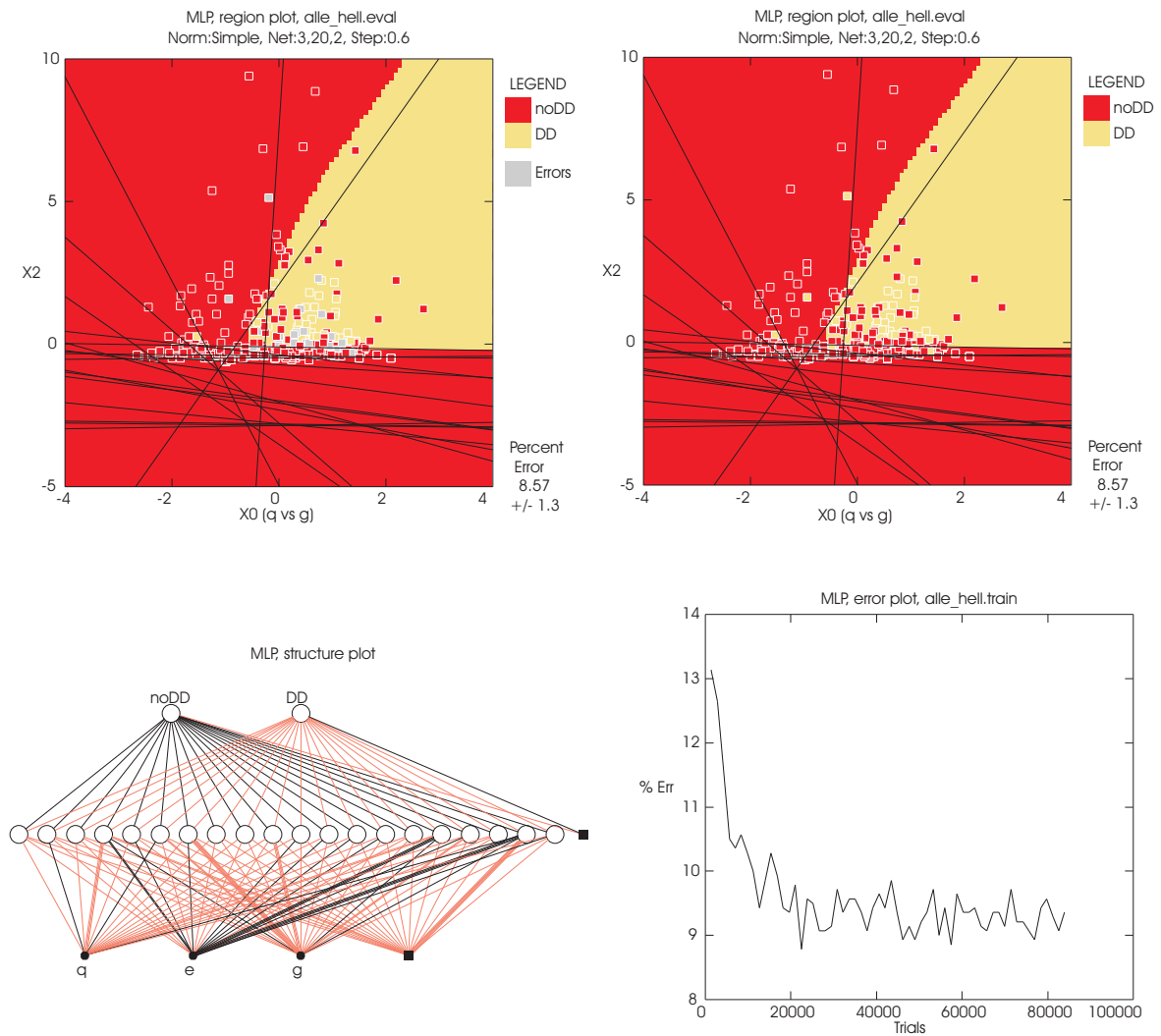


**Figure 7.7:** Plots produced during training and evaluation with the MLP classifier. At the top decision region plots of the two parameters  $q$  and  $g$ . The structure plot bottom left represents the architecture of the classifier, the error plot bottom right shows how the error decreases during training. More details in the text.

The final configuration which was chosen to produce the best results are  $3 \times 20$  epochs of training, a single hidden layer with 20 nodes and a step size of 0.6. A higher step size improves the training time because of the greater increment after each trial. Too big step sizes may lead to a classifier which never converges because the system gets unstable or oscillatory [Lee, 1989]. The improvement of a higher step size of 0.6 instead of 0.4 of the former settings was a slightly better classification rate of dust devil patterns while the no-dust devil patterns and the total error rate degraded a little bit (Figure 7.6). 16 of 21 misclassified dust devils in the evaluation file (Figure 7.6, in the middle) have again sizes less than 10 pixels, as 33 of 45 misclassified dust devils in the test file (Figure 7.6, at the bottom). No-dust devil patterns which were wrongly classified as dust devils have always cluster sizes higher than 10 pixels, a high  $q$  value and lower  $\epsilon$  values. When the eccentricity is higher, also a higher  $q$  value is seen in the patterns which leads to a false positive classification. If  $q$  is lower, also  $\epsilon$  is small and the pattern is again regarded as a dust devil if accompanied with a sufficient size.

Further testings with different sigmoid functions and weight configurations revealed only a

worse classification. These settings are anyway recommended not to be changed [Kukolich and Lippmann, 2004]. Also a second hidden layer included in the architecture of the classifier with nodes ranging in number from 5 to 25 resulted in no improvements. The presented results in Figure 7.6 and 7.7 seem to be the best achievable classification for the dust devil's bright spot with the multi-layer perceptron.

Figure 7.7 shows several plots created during training and evaluation with the settings of simple normalisation,  $3 \times 20$  epochs of training, a single hidden layer with 20 nodes and a step size of 0.6. In the upper half decision region plots are shown after applying the trained classifier to the evaluation file. The two plots are in general identical but in the left plot the misclassified patterns are highlighted as grey squares. Each square represents one pattern included in the evaluation file. Red squares are no-dust devil patterns, yellow ones are dust devil patterns. The right plot is used to discover if the misclassified patterns highlighted in the left plot are no-dust devil or dust devil patterns. The yellow background indicates a region where patterns are mostly dust devils, in the red region patterns are mostly no-dust devil patterns. Some of the red squares lie within the yellow region and vice versa but are correctly classified. That is because it is a two-dimensional plot ( $q$  vs.  $g$ ), although we actually have a three-dimensional problem (parameters  $q$ ,  $\epsilon$  and  $g$ ). The black lines represent hyperplanes defined by the nodes of the hidden layer (same number of hyperplanes as nodes). They generate borders between decision regions.

The structure plot shows the architecture of an MLP and is seen bottom left in Figure 7.7. The three parameters  $q$ ,  $\epsilon$  and  $g$  build the input layer, the hidden layer is build of 20 nodes, and the two classes 'noDD' and 'DD' represent the output layer. The two black squares in the input and hidden layer are bias nodes. Negative weights are coloured orange, positive weights are black. The thickness of the lines is proportional to the magnitude of the connecting weight. The average percent error in classification during each epoch of training is stored in a file and the developing during training can be seen in Figure 7.7, bottom right. The error decreases strongly during the first trials, later the improvements are only minimal with further training.

## Nearest Neighbour Classifiers

The idea of a nearest neighbour classifier is that a pattern is probably of the same class as those patterns nearest to it [Kukolich and Lippmann, 2004]. Nearest neighbour classifiers are quite simple when storing all the training patterns and calculate distances to them all for each testing pattern. The computation can then be quite extensive for larger datasets. Also these classifiers do not generalise well where training and test data differ. A rough estimate how difficult a problem is can be obtained and the classifier is able to create complex decision regions.

A  $k$ -nearest neighbour (KNN) classifier trains by storing all training patterns presented to it. The  $k$ -nearest patterns to the test pattern are found using Euclidean distances during testing. The class which occurs the most among the  $k$  neighbours is assigned to the test pattern [Duda et al., 2001]. The best results using this classifier were obtained with  $k = 1$ , only the closest neighbour is considered in the classification decision. Figure 7.8 shows the obtained error results. Cross validation replaces this time the training error output. Leave-

Error Report - alle_hellknn.err.cross_validation						
Class	Patterns	# Errors	% Errors	StdDev	RMS Err	Label
0	1222	67	5.48	( 0.7)	0.234	noDD
1	178	96	53.93	( 3.7)	0.734	DD
Overall	1400	163	11.64	( 0.9)	0.341	

Error Report - alle_hellknn.err.eval						
Class	Patterns	# Errors	% Errors	StdDev	RMS Err	Label
0	404	17	4.21	( 1.0)	0.205	noDD
1	63	32	50.79	( 6.3)	0.713	DD
Overall	467	49	10.49	( 1.4)	0.324	

Error Report - alle_hellknn.err.test						
Class	Patterns	# Errors	% Errors	StdDev	RMS Err	Label
0	384	8	2.08	( 0.7)	0.144	noDD
1	83	54	65.06	( 5.2)	0.807	DD
Overall	467	62	13.28	( 1.6)	0.364	

**Figure 7.8:** Classification results of the  $k$  nearest neighbour classifier. At the top the results of the cross validation test on the training data, in the middle the results of the evaluation data, at the bottom the results of the test file.

one-out cross validation tests one pattern at a time against a trained KNN model containing all but that single test pattern. Most obvious is the worse classification of the dust devil patterns, especially for the evaluation file in comparison to the MLP results. The no-dust devil patterns have also a lower correct classification rate. The decision region plot for the evaluation (Figure 7.9) shows now a more complex structure trying to characterise single patterns much better. Testing with higher  $k$  values (more neighbours taken into account for a test pattern) revealed only an improvement in classification of class 0 with a significant decrease in correct classification of dust devil patterns.

These results show that in general a nearest neighbour classifier is able to divide the input space into two parts. One part includes the no-dust devil patterns, the other the typical, well represented dust devil patterns consisting of roughly 40-50% of the real dust devil patterns. This is an acceptable result when considering that no adaptive learning is applied and generalisation depends highly on the training data.

A condensed  $k$ -nearest neighbour classifier (CKNN) reacts during testing like a KNN classifier. During training, however, it exa-

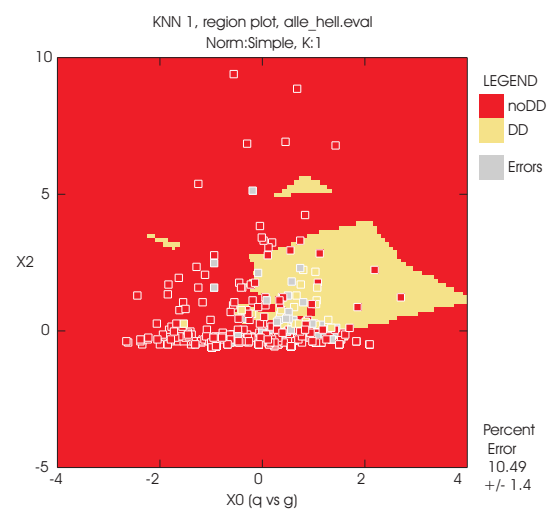


**Figure 7.9:** Decision region plot for the two parameters  $q$  and  $g$  after applying the trained KNN classifier to the evaluation data.

mines the patterns successively and stores only those that are assigned the wrong class. The advantage is the less amount of stored patterns. Epochs are set how many times through the training data shall be cycled. The classification of the dust devil patterns improved a lot during training. Only 18.31% of the dust devils were misclassified compared to 50.59% during MLP training. The classification results of the CKNN classifier of dust devil patterns in the evaluation and test file are similar to the MLP results. Surprisingly, class 0, the no-dust devil patterns, had this time a bad classification rate of about 20% for the training and the two test files. This results in an overall error rate of approximately 23% which is quite unacceptable compared to the former findings. Patterns which had small sizes, a low  $\epsilon$  but high  $q$  values were regarded as dust devils and raised the error in class 0 (no-dust devil patterns). According to our guideline we want to keep the error low in class 0, accepting a possible higher error rate for class 1, the dust devil patterns. The CKNN classifier is therefore not suitable, and the MLP results are still better than the KNN results.

### Committee Database

The idea behind a Committee database is that one single classifier does not provide the best performance. The combination of the decision outputs of several trained classifiers may result in a better classification. New training and testing files have to be created including the outputs from former training and testing. Any of the classifiers implemented in the LNKnet library can be used again on this newly-created dataset. Classifiers which had a bad classification rate when applied to the original data may perform now quite well. Our committee dataset consists of the outputs of the MLP and the Support Vector Machine (SVM) classifier.

A SVM classifier is similar to a perceptron. It separates the input space into two classes by using a hyperplane. The position of the hyperplane is such chosen that the margin is maximised between the two classes. The margin is the minimum distance from the separating hyperplane to the closest patterns in the two classes. This training samples (vectors) define the position of the optimal separating hyperplane and are the most difficult patterns to classify [Duda *et al.*, 2001]. These vectors are the support vectors. Other more distant vectors are not used. More details about the principle of the SVM and the adjustable parameters for classification provided by the LNKnet library can be found in *Kukolich and Lippmann* [2004].

The results of the SVM classifier revealed a misclassification rate of 2.23% for class 0 (no-dust devil patterns) and 47.62% for class 1 (dust devil patterns, 30 of 63 dust devils misclassified) when applied to the evaluation data. The total error rate was 8.35%, which is slightly better than the MLP results. Applied to the test data the classification resulted in 0.78% error for class 0 and 61.45% for class 1 (51 of 83 dust devils misclassified) with a total error rate of 11.56%. This is again better than the former MLP results but only because the classification of no-dust devil patterns improved while more dust devil patterns were misclassified. Nevertheless, the SVM and MLP classifications are the best obtained results of all tested classifiers. The committee was therefore built of the results of these two classifiers.

As stated above the new input space is built by the outputs of the selected classifiers. This means that four parameters are now in the training and test files. The parameters are derived from the two output classes from two classifiers. Every classifier can now be used again,

Error Report - alle_hell_commgauss.err.test_on_train							
Class	Patterns	# Errors	% Errors	StdDev	Avg LogL	Label	
0	1222	58	4.75	( 0.6)	-0.766	noDD	
1	178	63	35.39	( 3.6)	-2.498	DD	
Overall	1400	121	8.64	( 0.8)	-0.987		
Error Report - alle_hell_commgauss.err.eval							
Class	Patterns	# Errors	% Errors	StdDev	Avg LogL	Label	
0	404	17	4.21	( 1.0)	-0.715	noDD	
1	63	19	30.16	( 5.8)	-2.488	DD	
Overall	467	36	7.71	( 1.2)	-0.954		
Error Report - alle_hell_commgauss.err.test							
Class	Patterns	# Errors	% Errors	StdDev	Avg LogL	Label	
0	384	9	2.34	( 0.8)	-0.695	noDD	
1	83	42	50.60	( 5.5)	-2.817	DD	
Overall	467	51	10.92	( 1.4)	-1.072		

**Figure 7.10:** Classification results of the Gaussian classifier applied to the Committee dataset. At the top the results of the test on the train data, in the middle the results of the evaluation data, and at the bottom the results of the test data.

and training was started with the MLP and SVM classifiers since they have revealed the best classification results before. This time the results were somewhat worse than with the MLP classifier alone. The best results were now obtained by using a Gaussian classifier. This is a likelihood classifier which means that a probability density function is estimated for each class [Kukolich and Lippmann, 2004]. Gaussian classifiers are usually the most common and simplest classifiers. Kukolich and Lippmann [2004] state that they should be used first on a new classification problem. They resulted in a bad classification when tried on the original data which is quite clear after examining the histograms generated from the retrieved dust devil parameters (see Figure 6.6, page 42). The Gaussian classifier models namely each class with a Gaussian distribution centred on the mean of that class. The covariance matrix can be found for each class separately or the variances are averaged for all classes. There can also be a diagonal covariance matrix, one variance for each input dimension, or full covariance matrices can be calculated.

The configuration of the Gaussian classifier applied to the committee database which produced the best results includes a single variance for all classes but one for each input dimension. The error results are shown in Figure 7.10. The test on the training data (Figure 7.10, at the top) was added to provide a comparison to the other classifier results. Here, the classifier trained with the training data was again applied to the training data which was not the case in the former classifications. The obviously good performance is not as reliable as the results from the former MLP or KNN classifications.

The results from the evaluation are satisfying. Class 0 has only 17, class 1 19 misclassified patterns with a total error rate of 7.71%. That are two additional patterns for each class which are correctly classified compared to the MLP results. The two dust devil patterns which are

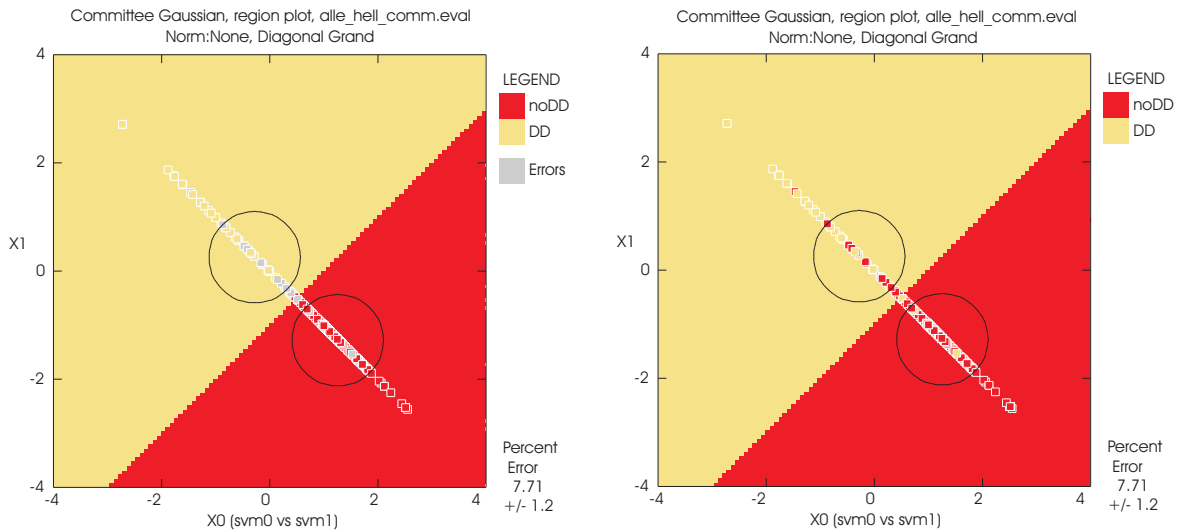


**Figure 7.11:** Decision region plots after applying the Gaussian classifier to the evaluation file of the Committee dataset. Both plots are the same but in the left one the misclassified patterns are highlighted as grey squares.

now additionally correctly classified have sizes of 8 and 9 pixels, with high  $q$  values (above 95%) and an eccentricity of 0.63 and 0.72. The Committee-Gaussian classifier seems to be a little more sensitive to smaller sizes. The other misclassified dust devil patterns are the same in both classifications, with the Committee-Gaussian and the MLP classifier. Also the misclassified no-dust devil patterns are mostly the same when comparing the results of these two methods.

The results of the test file are similarly satisfying. Here, 9 patterns are misclassified in class 0 and 42 in class 1 compared to 10 and 45 patterns, respectively, with the MLP classifier, giving a total error rate of 10.92%. The lists of misclassified dust devil patterns of the MLP and Committee-Gaussian results differ only in five patterns, although two completely different methods were used. Most of the misclassified patterns (33 of 45) with the Committee-Gaussian classifier have sizes less than 10 pixels, others have a too high eccentricity or a too low  $q$  value. No-dust devil patterns which were judged as dust devils have always sizes greater than 10 pixels, high  $q$  values and a moderate eccentricity. The no-dust devil patterns in the misclassified lists of both classifiers are also mostly the same. The lower performance of the correct classification of dust devil patterns included in the test file compared to the evaluation file seems to be because more samples have no typical dust devil values. At least there are twice as many dust devils with sizes less than 10 pixels in the misclassified list of the test file than of the evaluation file. The classification of the test file was always worse than that of the evaluation file.

Figure 7.11 shows decision region plots obtained by applying the Gaussian classifier to the Committee evaluation file. Input patterns represented by the small squares are displayed on a line in this two-dimensional plot of the output parameters of the SVM classifier (svm0 and svm1). This view reveals a possible strict separation of the data, coloured squares which do not fit to their background colour are misclassified patterns as it can be seen in the left plot of Figure 7.11. When displaying combinations of the other parameters of the Committee data this strict separation is not seen, explaining why this classifier does not provide a better

classification rate than the MLP classifier alone.

### Selected Classifier

Although the Committee-Gaussian classifier provides a slightly better performance (number of misclassified patterns decreased), the MLP classifier was preferred. MLP tends to misclassify smaller dust devils with sizes less than 10 pixels, while Committee-Gaussian emphasises the quality parameter  $q$  and the eccentricity  $\varepsilon$ . A sufficient size of clusters, however, seems to be reasonable so that not all of the smallest bright objects are regarded as dust devils. Preference was therefore given to the MLP classifier because the kind of classification seems to be more important than to choose the lowest number of misclassifications with respect to upcoming investigations of HRSC and MOC image data.

It also has to be kept in mind that the Committee-Gaussian classifier is a combination of three different methods of classification. The MLP classifier used as a single method is almost as good as the Committee-Gaussian classifier regarding the results. What can be seen from the presented classification examples here and the conducted but not explained methods, is the possible achievable maximum of correct classification of the bright spot of the dust devils. Some methods revealed as their best results almost identical outputs approximating the results of the MLP classifier, when the training and testing files were compared.

### 7.2.2 Classification of the Dust Devil's Shadow

The pattern recognition software is built such that after searching for brightness maxima clusters, a shadow is searched for each of these clusters. The question is now if all collected data from each bright cluster shall be used to create a dust devil shadow database. Since there are quite more objects than dust devils and naturally only the dust devil clusters include a dust devil shadow, this would lead to a large database with many samples but with a strong imbalance between shadow and no-dust devil shadow patterns. Correct classification will be complicated. It was therefore decided to include only data derived from dust devils in the database, so that at least one sample represents a dust devil shadow out of the detected brightness minima clusters belonging to one bright spot.

After examining all of the 38 VIKING images filtering the dust devils' bright spots and their accompanying shadows, 13 images were selected. These 13 images include each 10 or more dust devils with more or less good representations of dust devil shadows. A total of 4589 patterns are available, with 213 real dust devil shadows and 4376 no-shadow patterns (other dark clusters), giving a ratio of 1:20.5. The data were grouped in training and testing data in such a way, that this ratio was almost kept in each file. The training file got again 60% of the whole data, the evaluation and test files each roughly 20%.

The whole procedure as for the classification of the bright spots were conducted again. First, the data were normalised and the feature selection tool was applied to the data. The best parameters for classification of the dust devil shadow patterns seem to be the barycentre coordinates  $x_s$  and  $y_s$ , and the size  $g$  with a total error of 0.9%. This is the anticipated result

Error Report - ausgewaehlte_schattenmlp.err.train						
Class	Patterns	# Errors	% Errors	StdDev	RMS Err	Label
0	52460	215	0.41	( 0.0)	0.054	noSch
1	2660	147	5.53	( 0.4)	0.235	Schatten
Overall	55120	362	0.66	( 0.0)	0.074	
Error Report - ausgewaehlte_schattenmlp.err.eval						
Class	Patterns	# Errors	% Errors	StdDev	RMS Err	Label
0	936	4	0.43	( 0.2)	0.060	noSch
1	43	4	9.30	( 4.4)	0.306	Schatten
Overall	979	8	0.82	( 0.3)	0.087	
Error Report - ausgewaehlte_schattenmlp.err.test						
Class	Patterns	# Errors	% Errors	StdDev	RMS Err	Label
0	817	1	0.12	( 0.1)	0.037	noSch
1	37	4	10.81	( 5.1)	0.310	Schatten
Overall	854	5	0.59	( 0.3)	0.074	

**Figure 7.12:** Classification results of the MLP classifier applied to the shadow dataset. The configuration was simple normalisation, selected features  $x_s, y_s, g$ ,  $3 \times 20$  epochs of training, a single hidden layer with 25 nodes and a step size of 0.2. At the top the results of the training data, in the middle the results of the evaluation data, and at the bottom the results of the test file are shown.

(see Section 6.1.4). Four applied classifiers provided almost the same good results on the test files only differing in one or two misclassified patterns of both classes. Again, the choice was made in favour of the MLP classifier. Beside the good classification results, the characteristics of this classifier promise a satisfying generalisation when applying it to new data.

Figure 7.12 shows the results of the MLP classifier. The overall error rates are below one percent for every test file. Again, the classification of the no-dust devil shadow patterns is better than the classification rate of dust devil shadows. The very good results depend this time on the many more data available for class 0 leading to a low percent error rate. The error for class 1, dust devil shadows, is about 10%, which is also a very satisfying result. It was already seen from the histograms (see Figure 6.6, page 42), that the barycentre coordinates  $x_s$  and  $y_s$  of the shadow clusters shall have values about 40 and  $<40$ , respectively. Misclassified dust devil shadow patterns have either  $x_s$  values which are too far away from 40 or very low  $y_s$  values which means that the cluster is far away from the image centre (where the bright spot is located). Low  $y_s$  values are allowed but then the cluster size has to be much larger. This is consistent with the appearance in the original images: if a dust devil is larger, the shadow is larger as well and the barycentre coordinates of the cluster move from nearby the centre to the upper part of the cut-out. This behaviour is also seen very well in the decision region plots (Figure 7.13).

Figure 7.13, upper left, shows the decision region plot built by the two parameters  $x_s$  and  $y_s$  (here indicated as  $x$  and  $y$ ). The  $y$ -axis is defined positive in an upward direction in contrast to our original image cut-outs where the point of origin is in the upper left corner. This results from how the images are read in. So the decision region representing dust devil shadows are

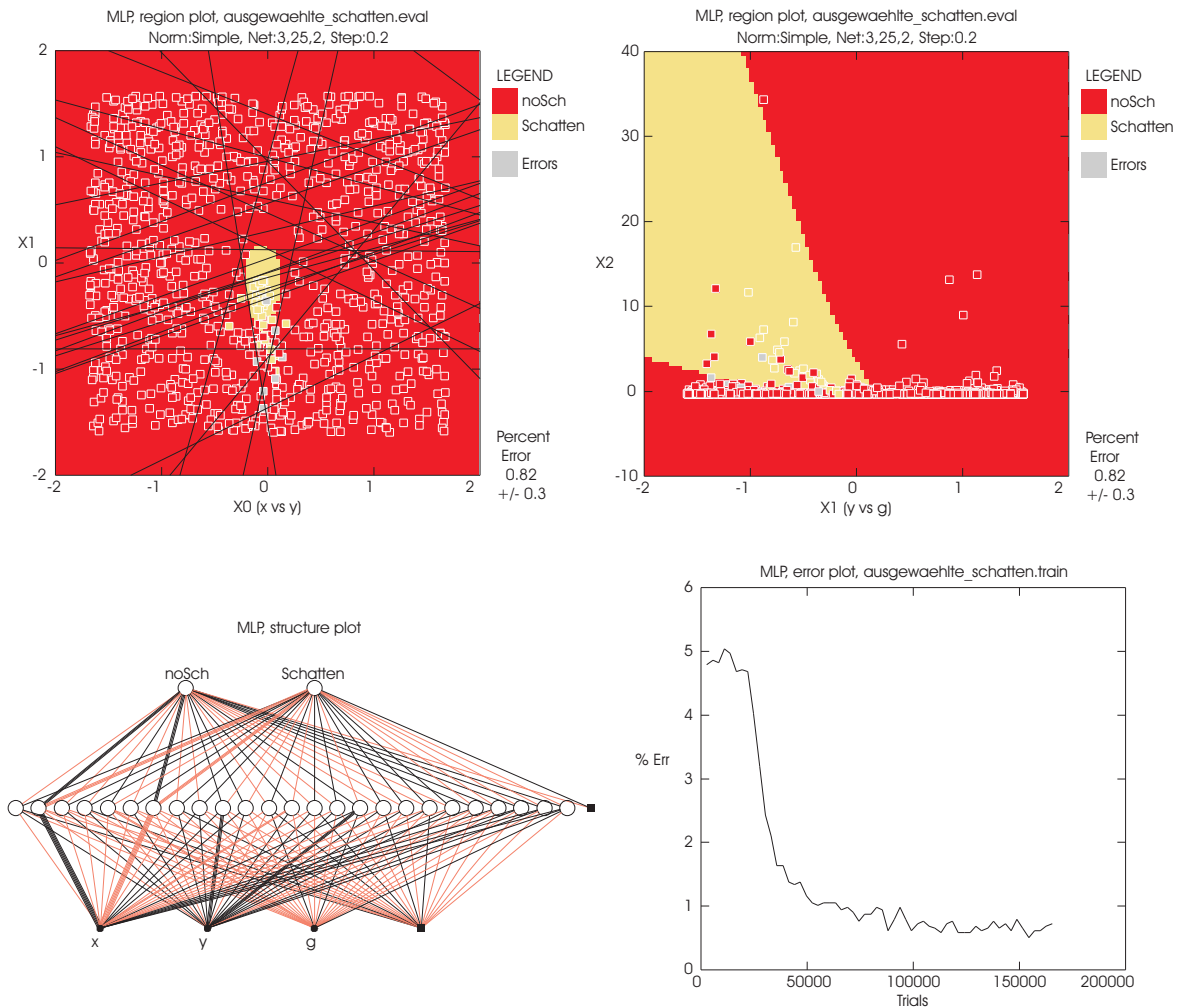


**Figure 7.13:** Plots produced during training and evaluation of the dust devil shadow data with the MLP classifier. At the top decision region plots of the two parameters  $x_s$  and  $y_s$  on the left, and  $y_s$  and  $g$  on the right. The structure plot bottom left represents the architecture of the classifier, the error plot bottom right shows how the error decreases during training. More details in the text.

found in the lower half of the MLP decision region plot whereas the shadows are displayed above the bright spot in the grey-scale images (see Figure 6.7, page 43).

Most of the dust devil shadow patterns are correctly classified and are located close to the image centre. Some patterns are still around  $x_s = 40$  but have lower  $y_s$  values. That the size  $g$  increases with decreasing  $y_s$  coordinate can be seen in the right decision region plot. Dust devil shadows are still correctly classified with higher distance to the centre (location of the bright spot) if the size increases as well. In this view of the normalised input space almost all of the left half with  $g > 0$  is assigned to dust devils. The hyperplanes represented as black lines in the left decision region plot are not displayed here because they would cover most of the data patterns (squares).

The no-dust devil shadow samples are located throughout the plot beside in the centre (Figure 7.13, upper left). This is the position of the bright spot and naturally no dark features can be found there, so there is a gap where no patterns are located in the plot. The yellow decision region where patterns are regarded as dust devil shadows is extended in this gap far beyond where dust devil shadow samples are actually located. This plays a role in classification.

Shadow patterns located on that side of the bright spot where it is not expected to detect any dust devil shadow because of the illumination conditions, will sometimes be classified as dust devils. This problem occurred mainly during HRSC analyses and will be discussed in Section 7.3.

The structure plot of the MLP classifier is seen in Figure 7.13, lower left. From the input parameter  $x$  strong connections are drawn to two nodes in the hidden layer. One with negative weights (orange), the other with positive weights (black). From these two nodes in the hidden layer strong connections are again drawn to the two classes. These nodes seem to be very important with respect to the classification results, defining significant hyperplanes which separate the data essentially.

The percent error plot on the lower right of Figure 7.13 shows the rapid decrease of the error during the first epoch of training. Further training reveals moderate improvements of the misclassification rate.

### 7.2.3 Results of the Pattern Classification

The trained classifiers, both for the bright spot and for the shadow of dust devils, were generated as C-code. This C-code was embedded in the existing pattern recognition software as

Class	Label	$e$	$q$	$g$	$x_s$	$y_s$
0	248	0.53	62.40	7	429.71	523.29
1	1			123	41.89	9.17
1	142			16	38.81	32.50
1	252	0.26	78.30	12	602.50	526.50
0						
0	253	0.00	112.80	4	417.50	527.50
0						
1	254	0.34	75.30	24	668.42	530.46
1	15			60	40.47	13.82
0	256	0.65	93.60	5	717.20	528.60
0						
1	263	0.65	72.30	15	793.13	539.60
1	37			68	40.03	28.34
1	265	0.49	85.20	52	746.52	543.92
1	11			128	38.75	27.18
0	267	1.00	69.70	138	1178.83	603.82
0						
0	277	0.92	96.80	7	1057.86	569.29
1	82			26	40.15	34.54
0	280	0.00	56.40	2	717.50	587.50
0						

**Figure 7.14:** A part of the classification results list of VIKING image f034b01. The first line was added for displaying reasons to identify the single columns. The first line of each data group represents an assessed bright cluster, the following lines if existent positively evaluated shadow clusters. More details in the text.

subroutines. First, a bright cluster is assessed if it is a dust devil bright spot or not. Independently of this classification, the dark clusters collected during the shadow search belonging to this bright cluster are assessed if one or more can be considered as a dust devil shadow. Then the next bright cluster is evaluated.

Figure 7.14 shows a part of the classification results file of VIKING image f034b01. The content is similar to the training and test files used for classification. The first column indicates the class assigned by the classifier. ‘0’ means no-dust devil cluster, ‘1’ stands for a dust devil cluster in the opinion of the classifier. The second column is the label given to the detected clusters by the Hoshen-Kopelman algorithm. They are useful to identify the clusters if it is necessary to examine the data in detail. The next three columns contain the parameters eccentricity  $\epsilon$ , quality parameter  $q$  and size  $g$ , which are used to assess the bright spot. For shadow patterns only the size is used, together with the coordinates  $x_s$  and  $y_s$  of the cluster, re-

<b>38 VIKING Images with 325 Dust Devils<sup>1</sup></b>		
Pattern recognition software detects	215 objects	166 dust devils - 49 other objects 77.21% dust devils - 22.79% other objects
325 dust devils		166 detected - 159 not detected 51.08% detected - 48.92% not detected
159 not detected dust devils	117	bright spot negatively evaluated; 97 with $g < 10$ pixels
	13	image border
	6	shadow is connected with other dark clusters
	28	no shadow exists in the data / too dark
	3	shadow exists but negative evaluation
130 non-detectable dust devils	195 detectable	85.13% (166 dust devils) detected
49 false positive objects	25	craters or crater rims
	21	hills
	1	possible dust cloud
	2	dust devils, hills?

**Table 7.1:** Classification results of the VIKING database. More details in the text.

presented in the last two columns. The indication of the coordinates of the bright spot is given to identify the object in the original image for a final human evaluation if the detected object is really a dust devil or not.

In each data group the first line demonstrates the assessment of the bright spot, which can be negative ('0', no-dust devil feature) or positive ('1', dust devil object). Independently of this classification, the possible shadows are evaluated. If one or more patterns fit a dust devil shadow in the opinion of the classifier, the values of these clusters are added along with the classification number and the label. If no shadow patterns are positively evaluated, only the classification number '0' is written in the next line after the bright spot data.

Samples are counted as dust devils if the bright spot and a dark cluster are both evaluated with '1'. At the end of the classification results file a summary is written how many dust devils have been detected in an image. All 38 VIKING images including 325 dust devils have been processed in this way. The results of this study can be seen in Table 7.1.

The pattern recognition software evaluates positively 215 objects whereof 166 are really dust devils and 49 are other objects. That is three of four positively assessed samples are indeed dust devils, which is a very satisfying result. This means as well that from the total number of 325 dust devils only 51.08% are detected. The 159 misclassified dust devils were examined in detail to discover the reasons why they have been negatively evaluated by the classifier.

The bright spot was not correctly classified for 117 of 159 dust devils, whereof 97 have sizes less than 10 pixels. Other dust devil samples reveal a too high eccentricity or a too low quality parameter for the bright spot as it was seen during the classifier testing, too. Other samples are misclassified due to an incorrect shadow classification. 13 dust devils were located at the image border so that no dark clusters can be retrieved as possible shadows because of the black frame in the VIKING images. Other misclassification reasons are that the image cut-out

<sup>1</sup>Details of each analysed image in Appendix C

is too dark to extract a shadow, or the shadow is connected with other clusters, so that it gets a strange shape and therefore strange parameters which do not fit dust devil values. Only three shadows are really misclassified despite they are seen in the data. Two of them, however, are broken in pieces and quite far away from the bright spot, the third is too small with a size of four pixels. Summarising these results it is reasonable and acceptable that some dust devils are misclassified. Note that eight dust devils exist in two misclassification categories, because e.g. the bright spot was not correctly classified and the dust devil was located at the image border.

Dust devils with bright spot sizes less than 10 pixels (97 dust devils), along with those located near the black frame of the images (13 dust devils) or in a very dark area so that no shadow can be extracted (28 dust devils), can be regarded as non-detectable dust devils. In summary this reveals 130 non-detectable dust devils, not 138 because of the double-counting of misclassified dust devils in two categories. 195 dust devils are therefore left which should be detectable. The resulting classification rate of 85.13% (166 of 195 dust devils positively evaluated) is a very good result.

The 49 objects which were wrongly assessed as dust devils are in most cases craters and hills. Hills have sometimes a very similar appearance like dust devils and a verification if an object is a dust devil or not can only be done if a second image of the same area is available. If the object did not disappear, move or at least change its appearance it is classified as hill. The classification performance depends on the quality of the orbit. If many hills or cratered surfaces are imaged, more false positive classifications will occur. If the image is quite dark, it is difficult to extract any bright spot of a sufficient size.

These classification results are very satisfying and no changes were applied to the architecture of the trained classifiers embedded in the software. The pattern recognition software was then tested with HRSC images.

## **7.3 Classification of the HRSC Dataset**

### **7.3.1 Adjustments**

Additional shadow classifiers are necessary for a correct classification of dust devils detected in HRSC images with different shadow directions. For this reason the 13 VIKING images used to build the shadow database were rotated clockwise through 90, 180 and 270 degrees so that the main directions are covered. Since the trained classifier has no strict decision borders it was thought that maybe four classifiers (for above, below, left and right locations of the shadows seen from the bright spot) are enough to cover the other slightly differing shadow locations as well. The pattern recognition software was applied to the 13 images again and training and testing files were created such that the data of the same images go into each the training, evaluation and test file as for the original case. Misclassified or correctly classified samples should be the same.

The newly-created databases were again simple normalised and the feature selection tool was

used to see which parameters are now selected. As it was expected the parameters  $y_s$ ,  $x_s$  and  $g$  provide in this sequence the lowest error rate for the through 90 and 270 degrees rotated datasets. Since the shadow is expected right or left of the bright spot,  $y_s$  should be in the range of 40 and is therefore the essential classification parameter. The sequence  $x_s$ ,  $y_s$  and  $g$  provides the best results for the through 180 degrees rotated dataset like for the original one. The MLP and its architecture were kept as classifier with  $3 \times 20$  epochs of training, one hidden layer with 25 nodes, and a step size of 0.2 for weight updating.

The total percent error of each of the training, evaluation and testing files is mostly consistent when comparing the three new datasets. The training file has an average total error of 0.71%, the evaluation file of 1.13% and the test file twice an total error of 0.85% and once of 0.35% with the through 90 degree rotated dataset. This is in the range of the classification results of the original data although those were slightly better with respect to all three training and testing files. Again, the classification of class 0, the no-dust devil patterns, was better in comparison to class 1, the dust devil patterns. The number of misclassified patterns ranges from 1 to 9 samples in the evaluation and test file. One more correctly classified pattern leads to a clear improvement in the percent error rate of class 1 because of the low number of dust devil shadow samples.

The reasons for the misclassification of dark cluster samples are more difficult to understand than for the bright spot samples. Much less misclassified patterns can be examined which is actually an appreciated result. The list of the misclassified patterns of the three newly-created datasets include many of the samples from the original dataset. There are, however, samples which were first correctly classified and now are assigned to the wrong class and vice versa. It can be concluded that the coordinates play the decisive role and stronger variances are only allowed in correlation with a larger size of the clusters (see Figure 7.13, upper right, page 69). The misclassified samples of all four datasets can be regarded as border problems and are therefore sometimes correctly classified and sometimes not.

One misclassified no-dust devil shadow pattern of the through 180° rotated dataset showed strange coordinates. It was classified as dust devil shadow with  $x_s = 39.50$  and  $y_s = 33.25$  although it is expected from this dataset to detect a shadow below the bright spot of dust devils located in the image centre. The  $y$ -values should be greater than 40. This misclassification problem was seen before in the decision region plots produced during training and testing of the shadow data (see Figure 7.13, upper left, page 69) and can be clearly seen again in the decision region plot of parameters  $x_s$  and  $y_s$  of the through 180° clockwise rotated dataset

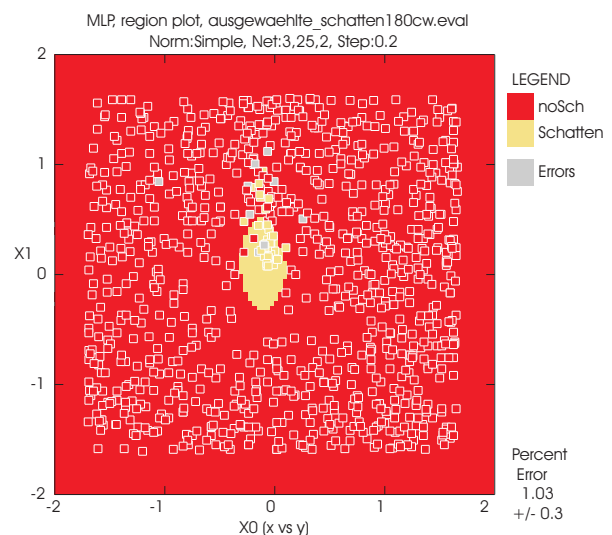


**Figure 7.15:** Decision region plot of the assessment parameters  $x_s$  and  $y_s$ . The yellow decision region of dust devil shadows is extended in the opposite direction where shadows are expected in this dataset.

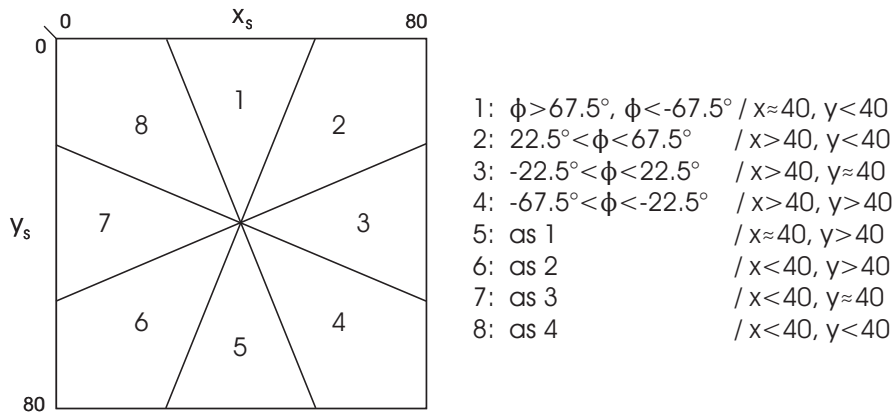


**Figure 7.16:** Shadow classifier regions and their parameter constraints. The unit of the coordinates is pixel.

(Figure 7.15). The decision region belonging to dust devil shadows is extended in the area where the bright spot is located since no-dust devil patterns are missing here and do not constrain the dust devil shadow region. This problem of misclassification of no-dust devil shadow patterns occurred not very often but it is an unintentional result which can be easily solved. After the classifier assigned class 1, dust devil shadow, to a presented sample the coordinates of the dark cluster are checked if they are in the desired range. If not, the assessment is changed to class 0. This is called post processing (see Figure 5.1, page 30) where the decision of the classifier may be changed due to additional considerations.

Examining four HRSC images with different dust devil appearances revealed very high positive detection rates. Over 300 alleged dust devils were detected for example in one image. Since one processed HRSC image is much larger than one VIKING image, this high number of positive detections is dependent on the image size as well. The analysis of the positively evaluated objects showed that the shadow classification with the coordinates and the size alone are not efficient in evaluating dust devils in HRSC images. Every somehow shaped dark cluster with the right size and location was assigned the class 1 and together with a positively assessed bright spot counted as a dust devil. An additional factor had to be found to constrain further the decisions.

The angle  $\phi$  of the best-fit ellipse adjusted to a shadow cluster was found to be useful to eliminate unnecessary dark clusters. It was not integrated in the classifier itself since it is then based on VIKING data which do not provide the needed informations for other shadow directions. The illumination angles were calculated and adjusted to the angle  $\phi$  as it is described in Section 6.2.2. A factor of  $\pm 10^\circ$  was added to the range defined by the two calculated illumination angles for the start and the end of an HRSC image strip. After the classifier assigned the class 1 to a presented dark pattern and is therefore regarded as dust devil shadow, the values of  $\phi$  are checked if they are in the desired range. If not the classification result is changed to class 0, no-dust devil shadow.

This reduced the number of positive detections a lot, for instance only eleven out of previously over 300 objects were left from one examined orbit. Admittedly, dust devils which have larger variances from the desired range of  $\phi$  values for the shadow are of course not positively assessed any more. This is true for dust devils where the shadow is smaller and not elongated

in the computed direction, or the dust devil is tilted and deformations in the vertical structure are reflected by the cast shadow.

Using the illumination angles as constraints reduced the false positive detections a lot, but still the detection rate of dust devils was lower than expected. This was attributed to the four available shadow classifiers, not sufficient to cover the direction of the dust devil shadows lying more diagonal than horizontal or vertical in the image. For this reason four additional shadow classifiers were built. The original dataset was used and all records were kept in their sequence and values but the barycentre coordinates  $x_s$  and  $y_s$  and the angle  $\phi$  of the dark clusters. These parameters were artificially rotated clockwise through 45, 135, 225 and 315 degrees. Classifiers were trained again, showing similar error rates as for the other shadow datasets. Figure 7.16 shows the different areas and by which classifier they are covered with the constraints of the angle  $\phi$  and the coordinates  $x_s$  and  $y_s$  of the dark cluster.

Applying a more appropriate shadow classifier to the images revealed naturally more positive detections than before. The analysis of the image where before over 300 and with the  $\phi$ -request only 11 objects were detected, produced now 49 positive classifications. This is an exception and is due to the fact that the Martian surface imaged in this orbit contained many small size craters. A normal detection rate was between ten to twenty positive classifications for a complete HRSC image strip.

### 7.3.2 Results

In this section two orbits and their classification results are discussed in detail, followed by a summary of all analysed orbits where it was already known that dust devils are included. HRSC orbits were examined and searched for dust devils all the time in parallel during the development of the pattern recognition software. 13 HRSC images included dust devils and were first investigated applying the software. The search was then extended to certain regions on Mars where many dust devils have been seen before analysing new unknown images.

#### Orbit 2242 - Terra Cimmeria

Orbit 2242 was taken in October 2005 and covered Eridania Scopulus and Planum Chromium located in Terra Cimmeria, southern hemisphere. These regions have elevations mostly between 0 and -1000 m, but parts of Eridania Scopulus are as high as 2000 m. The image was taken at the solar longitude<sup>1</sup>  $L_S = 305^\circ$ , southern summer, and local time was 1220 hours. The season and the time of day favour dust devil formation.

18 dust devils have been seen before the pattern recognition software was applied and their diameters, heights and forward speeds have been analysed. Figure 7.17 shows a part of the classification results list summarising the results of each image cut-out of the long image

<sup>1</sup>The solar longitude provides the angle between the Mars-Sun line at the time of interest and the Mars-Sun line at the vernal equinox. It is a measure for the season, with values of  $0^\circ$ - $90^\circ$  representing northern spring,  $90^\circ$ - $180^\circ$  representing northern summer,  $180^\circ$ - $270^\circ$  representing northern autumn,  $270^\circ$ - $360^\circ$  representing northern winter.

strip of orbit 2242<sup>1</sup>. A total of eight positive classifications was achieved and all detections revealed indeed dust devils. One of these dust devils was also a new discovery which has not been seen before during the ‘human’ visual search. Three new dust devils have been detected altogether when the software was applied to the image without checking the values of the angle  $\phi$  and of the coordinates  $x_s$  and  $y_s$ .

h2242_0000.nd3.04_half_y28x0.pgm:	0	Staubteufel	gefunden!
h2242_0000.nd3.04_half_y28x1.pgm:	0	Staubteufel	gefunden!
h2242_0000.nd3.04_half_y28x2.pgm:	0	Staubteufel	gefunden!
h2242_0000.nd3.04_half_y29x0.pgm:	0	Staubteufel	gefunden!
h2242_0000.nd3.04_half_y29x1.pgm:	0	Staubteufel	gefunden!
h2242_0000.nd3.04_half_y29x2.pgm:	0	Staubteufel	gefunden!
h2242_0000.nd3.04_half_y30x0.pgm:	0	Staubteufel	gefunden!
h2242_0000.nd3.04_half_y30x1.pgm:	0	Staubteufel	gefunden!
h2242_0000.nd3.04_half_y30x2.pgm:	0	Staubteufel	gefunden!
h2242_0000.nd3.04_half_y31x0.pgm:	0	Staubteufel	gefunden!
h2242_0000.nd3.04_half_y31x1.pgm:	0	Staubteufel	gefunden!
h2242_0000.nd3.04_half_y31x2.pgm:	1	Staubteufel	gefunden!
h2242_0000.nd3.04_half_y32x0.pgm:	1	Staubteufel	gefunden!
h2242_0000.nd3.04_half_y32x1.pgm:	0	Staubteufel	gefunden!
h2242_0000.nd3.04_half_y32x2.pgm:	0	Staubteufel	gefunden!
h2242_0000.nd3.04_half_y33x0.pgm:	1	Staubteufel	gefunden!
h2242_0000.nd3.04_half_y33x1.pgm:	0	Staubteufel	gefunden!
h2242_0000.nd3.04_half_y33x2.pgm:	0	Staubteufel	gefunden!

**Figure 7.17:** A part of the classification results list of image 2242 showing the summary of each image cut-out.

Two of these new dust devils were then overruled by the post processing because of bad  $\phi$  values of the shadow patterns (Figure 7.18). The post processing decreased the number of positive detections from 27 (12 dust devils, 15 no-dust devil features) to 8 (8 dust devils, 0 no-dust devil features) which demonstrates the clear advantage of the post processing. The four dust devils which were now not correctly classified any more are due to the  $\phi$  checking. All formerly detected hills and parts of craters regarded as dust devils could also be eliminated on this account.

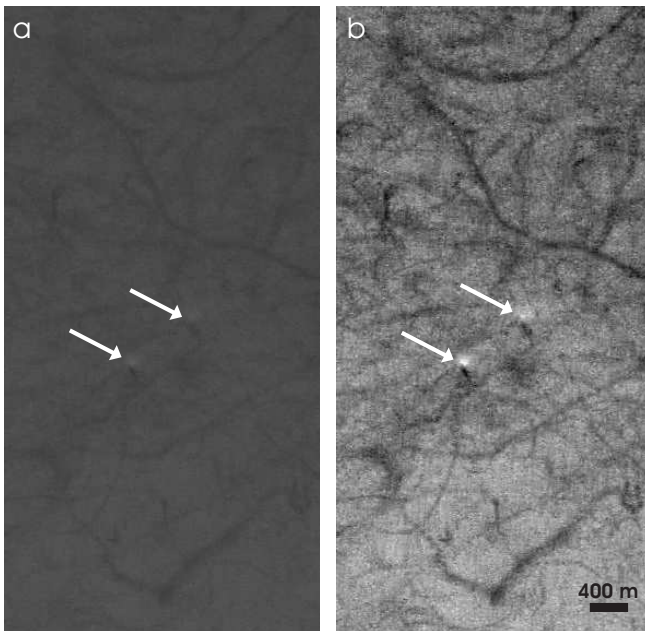


**Figure 7.18:** a) The original grey-scale image (orbit 2242) as the software processes it. b) Contrast enhanced image to show the dust devils (arrows) more clearly. The left dust devil was first correctly classified but the  $\phi$  checking expelled it. The black lines around the dust devils are tracks supposed to be left by dust devils.

Beside the formerly seen 18 and the three dust devils newly detected by using the pattern recognition software, additional dust devils were discovered in close vicinity of the other dust devils when the image was visually analysed again (Figure 7.18). These dust devils are very small so that the bright spots were sometimes not seen in the data filtered by the software. Parts of the image were quite dark as well. Most of the shadows have been correctly assessed by the classifier but the decisions were overruled because the deviations of  $\phi$  were too large. A total of 26 dust devils were counted, eight dust devils have been correctly classified, leading to a detection rate of 30.8% or roughly every third dust devil was detected by the software. Reasons for the misclassification are mostly the small sizes of the bright spots or the large deviations of  $\phi$

<sup>1</sup>See Appendix A for image identifiers

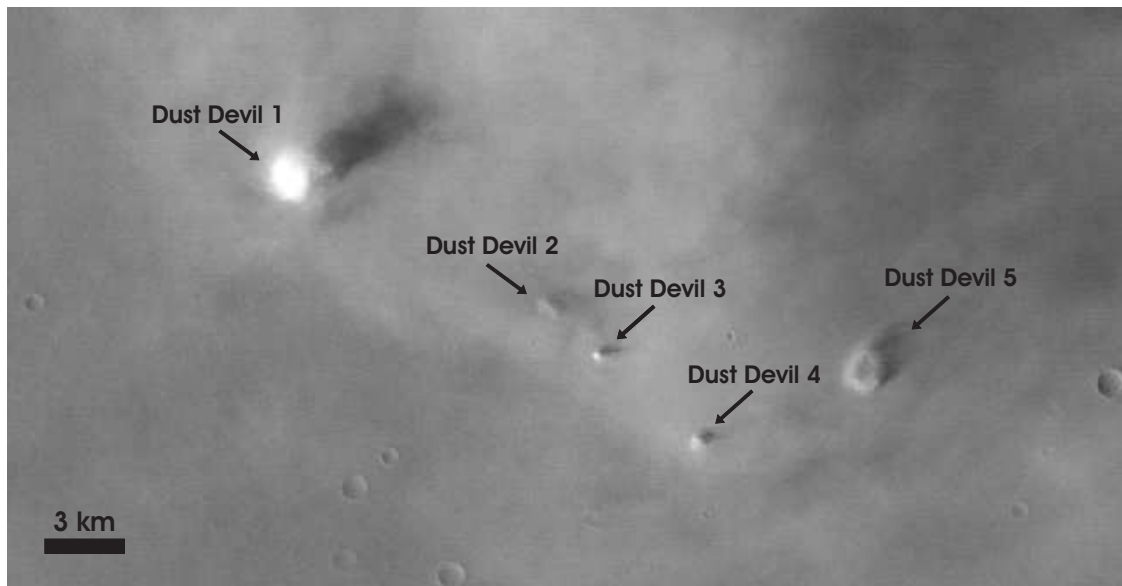


*Figure 7.19: Five dust devils in Syria Planum (orbit 2054) located in front of a dust storm.*

from the computed range of values which is allowed for the shadows.

### **Orbit 2054 - Syria Planum**

Syria Planum is a plateau about 7000 m high, just south of Noctis Labyrinthus, the most western extensions of Valles Marineris, the large canyon system on Mars. It is located on the southern hemisphere and is known as a region where dust storms and large dust devils have been seen. The image was taken in August 2005, on  $L_s = 273^\circ$ , begin of summer on the southern hemisphere, local time was 1513 hours. These conditions favour dust devil formation.

Figure 7.19 shows the five dust devils seen in this orbit just in front of a dust storm. The relation of dust devils with dust storms is discussed in Chapter 8. A total of 5 objects were positively evaluated with shadow classifier 3. One of these objects is dust devil 3 (Figure 7.19). Dust devil 2 and 5 are not detectable because they have no real vortices and no tight shadow. Not much was seen in the filtered data but fragments of the bright dust clouds. Dust devil 4 was unfortunately at the edge of one image cut-out and could therefore not be found. With the setting of 25 m/pixel resolution dust devil 1 is much too large so that during the relative brightness maxima search not many pixels are filtered in this area because the bright vortex covers everything else. The shadow is also too large and too far away from the bright spot when analysing the image with the defined  $80 \times 80$  pixel cut-out for the shadow search. Different resolutions applied to the image cut-out displayed in Figure 7.19 were tested to verify the performance of the pattern recognition and classification software and to avoid problems like that the dust devil 4 is on the edge of the former image cut-outs.

With a resolution of 25 m/pixel (half of the original resolution) dust devil 3 was correctly classified with shadow classifier 3 as before. The bright spot and shadow of dust devil 4 are both negatively evaluated. The size of the bright spot with  $g = 142$  was quite large and the

quality factor of  $q = 68.8\%$  was concurrently too low. The shadow is also very large with  $g = 501$ . This is maybe the reason for the misclassification or the variance in the seen  $y_s$  coordinate. The shadow classifier 2 revealed indeed a correct classification of the shadow but the  $\phi$  checking overruled the decision with class 0. Dust devil 3 was still correctly classified with shadow classifier 2.

Dust devils 3 and 4 are both correctly classified in principle when using one fourth of the resolution, 50 m/pixel. The  $\phi$  values of their shadow clusters differ from the allowed range by 0.55 and 4.15 degrees for dust devils 3 and 4, respectively. Allowing a larger range of  $\phi$  values ( $\pm 15^\circ$ ) revealed correct classifications for both dust devils. The reduction from half of the resolution to one fourth, changed unfortunately the  $\phi$  value of the shadow of dust devil 3 such that no correct classification was achieved now with the former settings of  $\pm 10^\circ$  for  $\phi$ .

With a resolution of 100 m/pixel (one eighth of the original resolution) dust devil 4 is positively assessed. Dust devil 3 was now not correctly classified due to its smaller size of seven pixels for the bright spot but showed otherwise good values of its parameters. The large dust devil 1 has now also acceptable values for the pattern recognition software but again the  $\phi$  value differs from the allowed range by 1.22 degrees which is the only reason why correct classification was prevented.

The  $\phi$  checking reduced the number of positively classified objects from 94 to 5 for this orbit 2054. As demonstrated above, some dust devils, however, are now not recognised any more. This is no problem if the dust devil shadow clusters are in the desired range, as it is expected if the dust-filled vortex is in an upright position. Tilted vortices as it is slightly seen at dust devil 3 in Figure 7.19 lead to incorrect classification depending on the resolution and the pixels filtered thereon.

Correct classification depends also on the selected shadow classifier suggesting to use more than one if the computed shadow directions are in the intermediate range of two classifiers. It could be shown that in dependency of the resolution, the selected classifier and the defined  $\phi$  range, all detectable dust devils 1, 3 and 4 (Figure 7.19) can be correctly classified.

### Summary of 13 HRSC Orbits including Dust Devils

HRSC images were visually searched for dust devils during the development of the pattern recognition and classification software. 13 orbits scattered over the Martian surface on both hemispheres included dust devils. The software was applied to all images although some orbits (e.g. orbit 1054) include dust devils which have no real vortices, the shadows were weak or looked like a dust cloud without a shadow. This makes a correct classification almost impossible. Table 7.2 shows the summary of the pattern recognition search in the 13 images.

Roughly every sixth detected object (16.9%) is a dust devil. The false positive patterns are mostly crater rims or hills. Especially the orbits 1081 and 3246 show a very high detection rate which was due to the large amount of craters seen in those images (Figure 7.20, a+c). The crater slope which is turned to the direction of the Sun appears bright, and the rim casts a shadow exactly at the position where a dust devil shadow is expected. Normally, the crater shadow is not circular as in Figure 7.20c, but perpendicular to the Sun direction because of the

<b>13 HRSC Images with 140 Dust Devils</b>				
Image	Number dust devils	Correctly classified	Total objects (incl. dust devils )	Notes for dust devil misclassification
0037	3	1	(410)	image border, bright spot weak
1054	1	0	5	dust cloud, bright spot weak
1081	5	1	49	weak shadows, $\phi$ check
1258	5	1	15	small dust devils
2032	2	1	14	$\phi$ check
2054	5	1	5	large dust devils, image border
2100	26	10	18	small dust devils, image border, $\phi$ check
2133	5	3	6	$\phi$ check, no bright spot
2225	8	0	3	small dust devils, shadow variances
2242	26	8	8	too small, $\phi$ check, image border
2315	4	2	2	small dust devil, $\phi$ check
3210	1	1	12	
3246	49	3	52	small dust devils, shadows too large
Total	140	32	189	

32 of 140 dust devils: 22.9% correctly classified  
32 of 189 objects: 16.9% are dust devils

**Table 7.2:** Classification results of 13 HRSC images. More details in the text.

rim. This would suffice to classify the object as a no-dust devil feature. In this case, however, the shadow concatenates with other dark parts around the crater, giving the resulting dark cluster a best-fit ellipse with a  $\phi$  value which fits the requirements computed for the prevailing illumination conditions. Craters like the one in Figure 7.20c led to the high detection rates. Hills have sometimes the same appearance as dust devils and pose therefore also a high number of false positive detections. Unlike craters they can only be discarded as dust devils in certain cases if they are not moving. The necessity of stereo images comes up since analysing only the nadir channel of one HRSC orbit is sometimes not enough. The total number of positively evaluated objects (410) for orbit 0037 (Table 7.2) is put in parentheses because this high number is an exception. Due to the extremely long image strip, more than 800 image cut-outs resulted in 14 hours of runtime of the software. Craters, hills and ridges are, of course, the reasons for detections, but the long orbit matches 8 to 10 times of the size of normal orbits. The total number of detections is not only a factor of the performance of the classifier but also of the orbit size summing up the detections from each cut-out. The high detection rate is an outlier and was therefore not included in this short statistic.

Every fourth to fifth dust devil is correctly classified (22.9%). This is a satisfying result considering the wide range of dust devil appearances. The computed range of the illumination angles cover sometimes two shadow classifiers. The images are then examined twice with different classifiers. The total number of correctly classified dust devils is written in the third column of Table 7.2, whereas the number of total detected objects states the mean of the two runs through the images. This was the case for orbit 3246 among others. One run was done with shadow classifier 3, revealing 1 dust devil of a total of 39 objects. The second run with shadow classifier 4 produced 64 total objects with 3 detected dust devils, including the one

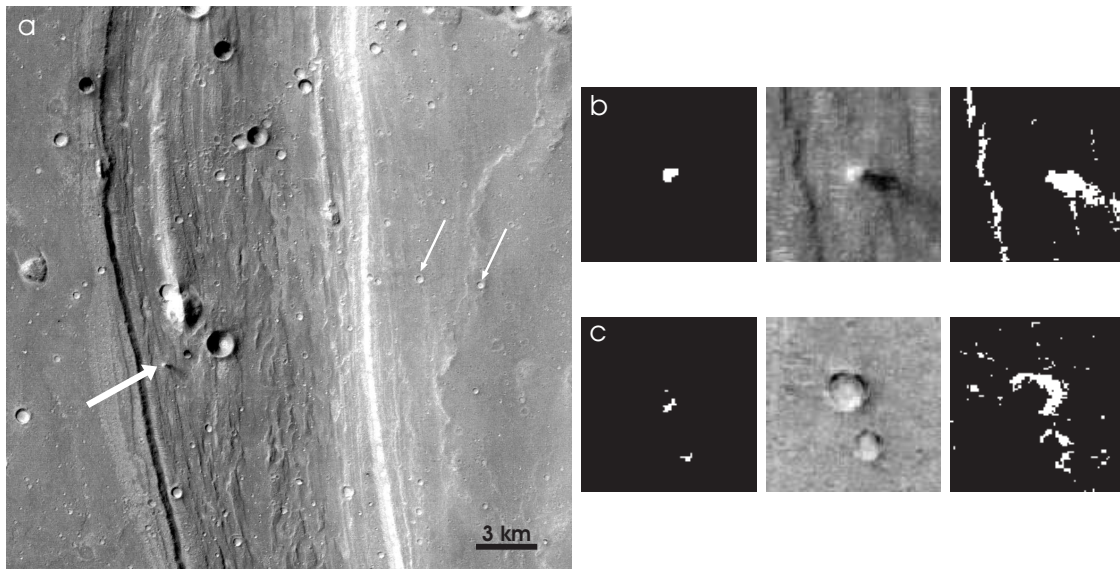


**Figure 7.20:** a) Part of orbit 3246 showing the surface with many small-size craters, two indicated by the thin white arrows. The big white arrow indicates a dust devil. b) The dust devil from a) displayed in detail and the filtered pixels for the bright spot and the shadow. c) A crater with filtered pixels which represents a false positive object.

from the first run. The two dust devils, now additionally correctly classified, would match with shadow classifier 3, but are correctly classified with shadow classifier 4. The reason is maybe the large size of the shadow clusters (Figure 7.20b). It was shown in Section 7.2.2 that at the expected coordinates moderate sizes are allowed, and clusters located more at the edge of the examined area are allowed to have larger sizes. The shadow of the dust devil in Figure 7.20b is quite large and is located where it is actually expected for shadow classifier 3. For shadow classifier 4 it is at the edge and the larger size is allowed in the estimation of the classifier.

This problem is a training problem based on the VIKING data. No such large shadows have been seen in these data leading now to a misclassification problem of large shadow clusters but located where they are expected. Adjacent shadow classifiers may classify them correctly since there are no strict boundaries defined by the shadow classifiers.

The main reason for the misclassification, however, is still the small size of dust devils, although HRSC deals now with another order of magnitude (less than 50 m in diameter) than small size VIKING dust devils have (less than 150 m in diameter). Over 30 of the 49 dust devils seen in orbit 3246 (Table 7.2) have bright spot sizes of less than 10 pixels or are not seen in the filtered data at all. This diminishes the number of detectable dust devils a lot. The checking of the  $\phi$  values of the shadow clusters prevents sometimes an accurate classification. It occurs not too frequently, but some dust devil shadows have just missed the allowed range, leading to a worse classification rate. Deactivating the  $\phi$  check would lead to too much positively assessed features as it was shown in Section 7.3.1.

How many objects are positively assessed depends on the surface and background of the orbit. If it is a clear orbit with little dust in the air and sharply displayed structures like craters, ridges or valleys (Figure 7.20), the search will find many objects which fit dust devil parameters. Orbits like image 2242 (see Figure 7.18, page 76) where the background appears

more pixelised and coarse, but smooth, let the dust devils be much more prominent than their surroundings. The results of the orbits 2242 and 2315 point this out with a classification quality ('Precision', see *Zabel [2005]*) of 100% for class 0. No no-dust devil feature was wrongly evaluated as dust devil. Every positively assessed object was indeed a dust devil. Additionally, when comparing the detection rates of different image cut-outs it can be seen that the detection rate increases considerably where craters and hills are numerous in the image and diminishes in smooth areas. Likewise, the more dust devils are in the image, the more will be correctly classified (Table 7.2).

The performance of the pattern recognition and classification software achieves not the same quality as when it was applied to the VIKING images (compare Table 7.1, page 71 with Table 7.2, page 79). The software is built on the VIKING database and therefore more sensitive to the parameter values obtained from these data. The consequential problems like too large dust devils can be solved when the HRSC images are adjusted to the VIKING images with respect to the resolution. The chance, however, to detect much more and smaller dust devils is then given away. The large dust devils would be seen anyway during the fast visual scan of the total image at highly decreased resolution which is always done, independently of the detections of the software. The experience teaches that several dust devils can occur simultaneously. If one is correctly classified, this leads often to the visual detection of all dust devils imaged in one orbit, because then it is known that the atmospheric conditions are suitable for dust devil formation.

HRSC images are on average 30 to 100 times larger than VIKING images. The total objects classified as dust devils must therefore be divided through the amount of image cut-outs to be compared to the number of classified objects per VIKING image. This gives a similar result of about 0.2-0.5 classified objects per HRSC image cut-out which represents approximately the size of one VIKING image.

It could be demonstrated that the typical well-shaped dust devils were correctly classified with the pattern recognition and classification software at a resolution of 25 m/pixel. No further changes will be applied to the software.

### **Investigating Several Regions on Mars**

After the first dust devils have been seen in VIKING images [*Thomas and Gierasch, 1985*] speculations started where they may occur most frequently on Mars. The northern lowlands were favourites because of the higher pressure supposed to help in the initialisation of dust devils. Former studies of VIKING or MARS GLOBAL SURVEYOR MOC images revealed insights about their occurrences in different regions on Mars. One of the regions with the highest dust devil frequency according to MOC studies [*Fisher et al., 2005; Cantor et al., 2006*] is Amazonis Planitia, indeed a northern plain. For this reason the search in new unknown images was started in Amazonis Planitia examining all available HRSC images for this region. The later chosen regions comply with results of former dust devil papers. It will be checked if the derived frequencies and characteristics of dust devils can be verified with HRSC data or if differences and new findings are discovered.

Table 7.3 shows the summary after analysing different regions on Mars. The detection rate

<b>Summary of Analysed Regions<sup>1</sup></b>				
Region	Number images	Number dust devils	Correctly classified	Mean total objects
Amazonis Planitia	87 (42)	8	1	14
Syria Planum	17 (16)	8	2	24
Chryse Planitia	29 (29)	166	34	44
Total	133 (87)	182	37	27

37 of 182 dust devils: 20.3% correctly classified  
37 of 2349 (87\*27) objects: 1.6% are dust devils

**Table 7.3:** Classification results of HRSC images from several regions. Images and their results from Table 7.2 are included for the appropriate region. The number of images in parentheses is the number of images which were analysed with the software (Amazonis Planitia) or which are included in the calculations of the mean total objects per image (Syria Planum).

of dust devils with 20.3% is almost the same as for the 13 HRSC images alone where it was already known that dust devils are included (Table 7.2). The fraction of dust devils from the total objects which were estimated by the classifier to be dust devils is only 1.6%, which means that every 63<sup>rd</sup> object is a dust devil. The performance depends strongly on the individual orbits as it was shown in the preceding paragraph. Many hills and craters lead to a high detection rate. It can also not be anticipated that in every orbit dust devils are seen. The comprehensive study of MARS GLOBAL SURVEYOR MOC images over four consecutive Mars years [Cantor *et al.*, 2006] revealed dust devils in every 238<sup>th</sup> image, but then 16 dust devils per image on average. HRSC images showed the simultaneous occurrence of multiple dust devils as well. Although no dust devils are imaged in an orbit, the classifier will likely detect some other objects which is the reason for the low ratio of dust devils to total objects classified as dust devils when analysing a large image database.

The scientific results of the dust devil search are discussed in Chapter 8. One specific characteristic is discussed here since it influences not directly the scientific results obtained from HRSC images, but it has definitely to be mentioned regarding dust devil investigations in VIKING images.

HRSC orbit 2128 covered mainly Lucus Planum, but also a small part of Amazonis Planitia, and was therefore selected for analysing. Lucus Planum is located south of the equator at 185°E and is roughly -2000 m high. Especially between 1°N and 4°S at 186°E which was covered by the image 2128 the surface consists of terrain heavily eroded by aeolian processes [Williams, 2007]. The grooved material is possibly composed of yardangs (linear wind-eroded hills shaped like upturned boat hulls). The yardang terrain is sedimentary or volcanoclastic in origin. Because the wind streaks of the outlying hills and the yardangs are parallel, the prevailing wind pattern from SW to NE could have been very strong and long lasting. The outlying hills looked like dust devils. The software assessed 72 objects positively but no one was a dust devil (Table C.3, page 124). Figure 7.21 shows the comparison between a cut-out of HRSC image 2128 and the VIKING image f038b12.

<sup>1</sup>Details of each analysed image from different regions in Appendix C

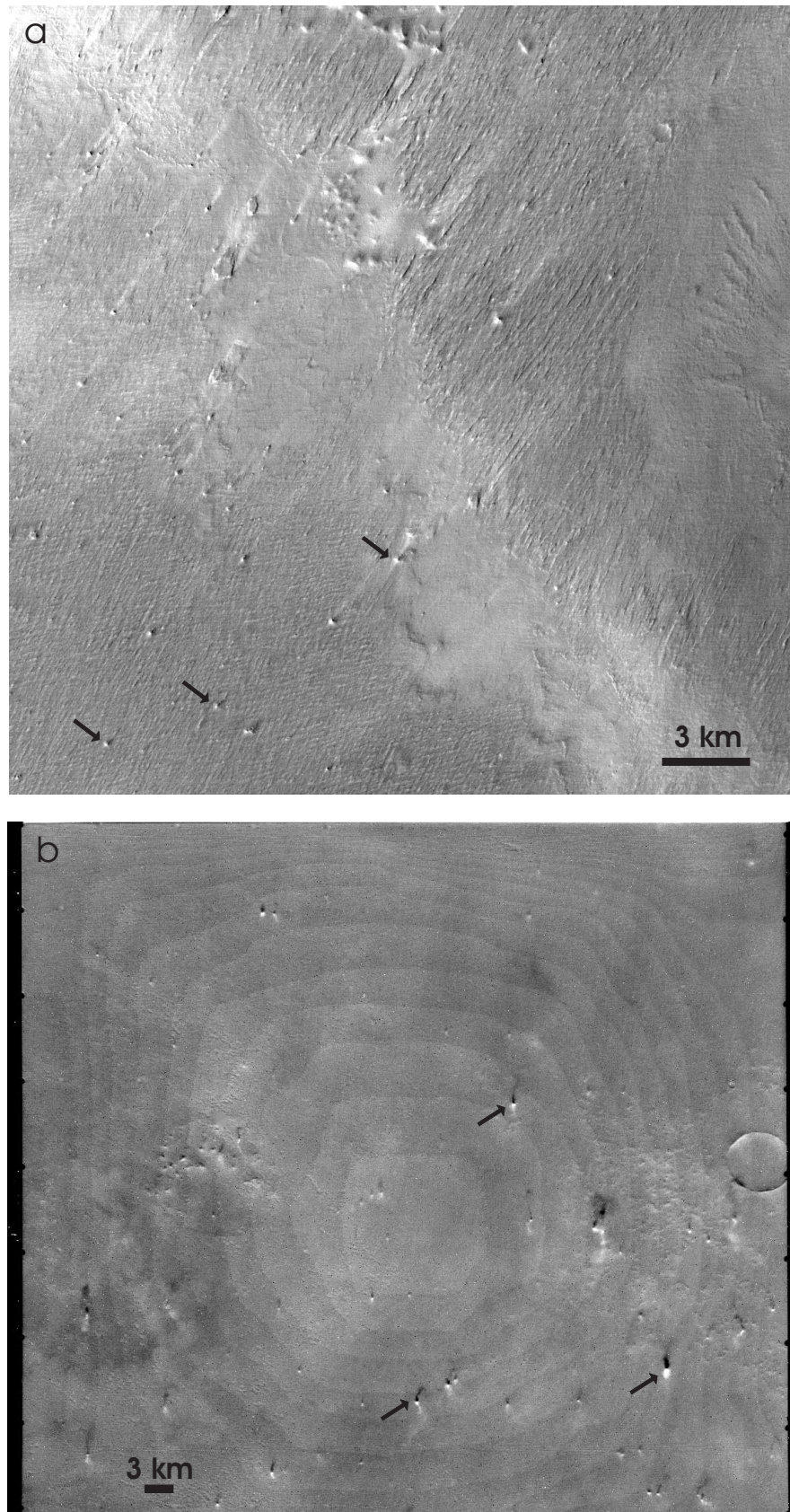


**Figure 7.21:** a) HRSC image 2128. The black arrows indicate some peaks which were classified as dust devils. b) VIKING image f038b12. The black arrows indicate some dust devils which are parts of the database for the classifier. The analogy to the features in the HRSC image is obvious.

The HRSC image has a three times better resolution than the VIKING image with a size of  $1200 \times 1200$  pixels and a resolution of 25 m/pixel. The VIKING image has a size of  $1204 \times 1056$  pixels with a resolution of 70 m/pixel. The dust devils in the VIKING image build the database for the classifier and the parameters fit now the hills seen in the HRSC image. Even the visual check could sometimes not clarify if these objects are really hills or dust devils. The stereo images were used to analyse if the detected objects are moving. This comparison revealed that all features must be hills.

The conclusion which is drawn from this analysis is that maybe some of the dust devils seen in VIKING images are hills and were wrongly counted as dust devils. Not many reference images (covering the same area at a different time) were available to prove that the objects disappeared and are therefore dust devils. The high resolution of HRSC images helps to analyse such ambiguous objects in detail and the stereo channels prove if it is a spatial and temporal variable feature.

## 7.4 Classification of the MOC Dataset

*Cantor et al.* [2006] reviewed MOC images from almost four Mars years for dust devil purposes. The search was started in September 1997, after MARS GLOBAL SURVEYOR arrived at the planet, and includes images up to January 21, 2006. Since MARS GLOBAL SURVEYOR stopped working in November 2006 due to a wrong command, almost all available MOC images have been already searched for dust devils. A summary of narrow angle (NA) and wide angle (WA) images including dust devils is shown in *Cantor et al.* [2006]. It is therefore not necessary to start a comprehensive search with the pattern recognition and classification software in MOC images. It will be shown that the software is properly working with images from this Mars mission as well.

Partly based on the former published paper of *Fisher et al.* [2005] 29 NA and 15 WA images have been selected and searched with the pattern recognition software. Most of the images covered Amazonis Planitia since this is the region with the highest dust devil activity according to MOC image analyses [*Fisher et al.*, 2005; *Cantor et al.*, 2006]. Other images covered Sinus Meridiani, Chryse Planitia, Sinai Planum, Mare Cimmerium, Noachis Terra and Claritas/Coracis Fossae. The results of applying the pattern recognition and classification software to MOC images are shown in the Tables 7.4 and 7.5.

The resolutions of the MOC images represent the original values but for the NA images m09-00193<sup>1</sup> and m13-00139, where one fourth and the half of the original resolution revealed the best classification results, respectively (Table 7.4). Dust devils were only counted for the NA images and compared with the counts of *Cantor et al.* [2006] because the quality of the WA images made it difficult to verify the high number of dust devils. Enhancing the contrast resulted often in almost black and white parts of the images. In addition, many stripes, brighter and darker ones, cross the images (Figure 7.22b). Some of the dust devils may only be verified to be ones if an image of the same area is available to prove that the objects have

---

<sup>1</sup>See Appendix A for image identifiers

<b>29 MOC Narrow Angle Images</b>					
Image	Resolution	Number dust devils ( <i>Cantor et al.</i> [2006])	Number dust devils (this work)	Correctly classified	Total objects (incl. dust devils)
m01-04498	11.31	1	1	1	1
m02-02530	5.81	1	1	1	6
m03-00396	5.96	1	1	1	1
m03-00435	6.12	1	2	0	1
m03-01869	5.68	1	1	0	2
m09-00193	11.52	1	1	1	1
m13-00139	17.66	1	1	1	1
m13-00483	11.05	19	17	2	2
e02-02175	12.34	6	4	1	1
e03-00938	6.14	3	2	1	1
e03-01651	9.22	7	3	0	0
e03-02304	12.30	4	3	0	0
e03-02711	4.59	1	1	0	0
e04-00765	9.25	4	3	2	2
e04-01708	9.28	4	3	1	1
e05-00695	12.34	1	1	1	1
e05-01343	12.31	1	1	1	1
e05-02077	12.28	4	4	3	3
e06-00037	12.27	5	5	1	1
e20-00851	12.91	5	4	0	0
e20-01304	12.92	3	2	0	0
e21-01170	6.45	3	2	0	0
e22-00666	6.44	5	2	0	0
e23-00955	12.91	10	6	1	1
e23-01274	12.90	5	3	1	1
r01-00879	12.88	4	4	1	1
r02-00052	6.45	6	1	1	1
r02-00468	6.46	3	3	0	0
r02-00854	9.69	4	4	0	0
Total		114	86	22	30
22 of 86 dust devils: 25.6% correctly classified					
22 of 30 objects: 73.3% are dust devils					

**Table 7.4:** Classification results of MOC Narrow Angle images. Resolution is displayed in metre per pixel. More details in the text.

disappeared. Counting was once done for WA image e21-01290 since this image is missing in *Cantor et al.* [2006] although it is mentioned in *Fisher et al.* [2005] and contains  $\sim 25$  dust devils. The dust devil counting in NA images produced sometimes a lower number than in *Cantor et al.* [2006]. One reason may be the quality of the images because we used the raw unprocessed images available from CD-ROMs or via the internet<sup>1</sup>. Another reason for a higher number of dust devils may be that also dust devils were counted which are only seen partly in the images, e.g. the shadow is visible but not the dust column. These dust

<sup>1</sup><http://pdsimg.jpl.nasa.gov/Missions/index.html>

<b>15 MOC Wide Angle Images</b>					
Image	Resolution	Number dust devils ( <i>Cantor et al.</i> [2006])	Number dust devils (this work)	Correctly classified	Total objects (incl. dust devils)
m01-01092	252.35	1	-	0	0
m01-01279	259.13	96	-	2	2
m01-01417	232.93	7	-	0	0
m01-01485	258.98	62	-	3	3
m01-01875	254.70	114	-	2	2
m01-02267	254.00	133	-	10	10
m01-02674	337.66	219	-	5	5
m01-02779	304.00	28	-	5	6
m01-03324	399.00	45	-	1	1
m01-05369	383.14	8	-	0	0
e03-00363	316.62	12	-	0	0
e03-01649	262.67	12	-	0	0
e06-00036	257.77	29	-	1	1
e21-01290	291.67	-	25	1	1
e22-00369	286.15	67	-	1	1
r02-00354	338.88	82	-	0	0
r04-00083	286.02	127	-	4	4
r04-02072	371.08	25	-	0	0
<b>Total</b>		<b>1139</b>	<b>25</b>	<b>35</b>	<b>36</b>

35 of 1164 dust devils: 3.0% correctly classified  
35 of 36 objects: 97.2% are dust devils

**Table 7.5:** Classification results of MOC Wide Angle images. Resolution is displayed in metre per pixel. More details in the text.

devils were not considered in our counting since the software is not capable of detecting such representations of dust devils.

After examining some images it was noticed that the original setting for filtering bright image pixels are too strong. It was set to  $n = 3.40$  and in some cases also to 3.00 (see Section 6.1.1). The allowed variation from the computed  $\phi$  values of the orientation of the shadow was extended from  $\pm 10^\circ$  to  $\pm 15^\circ$ .

It is most obvious that nearly all detected objects (73.3% for NA, and 97.2% for WA) are indeed dust devils (Tables 7.4 and 7.5). Only in three images hills were wrongly classified as dust devils. This good classification rate is of course also a result of the imaged surfaces. If there are not much hills or small craters, only dust devils fit to the required parameters as it was mostly the case for the Amazonis Planitia images (Figure 7.22a).

The high number of dust devils seen in the images cannot be reproduced with the pattern recognition search for both, the NA and WA images. The fraction of 25.6% detected dust devils for NA images is similar to the results of the HRSC image classification. In most cases the bright spot is too weak and even with the decreased value for filtering bright pixels it could not be displayed properly (Figure 7.22a). As always some dust devils are still too small even with the high resolution of the NA images or they have a strange shape. Some dust devils are too large in the NA images. Even the reduction of the resolution revealed

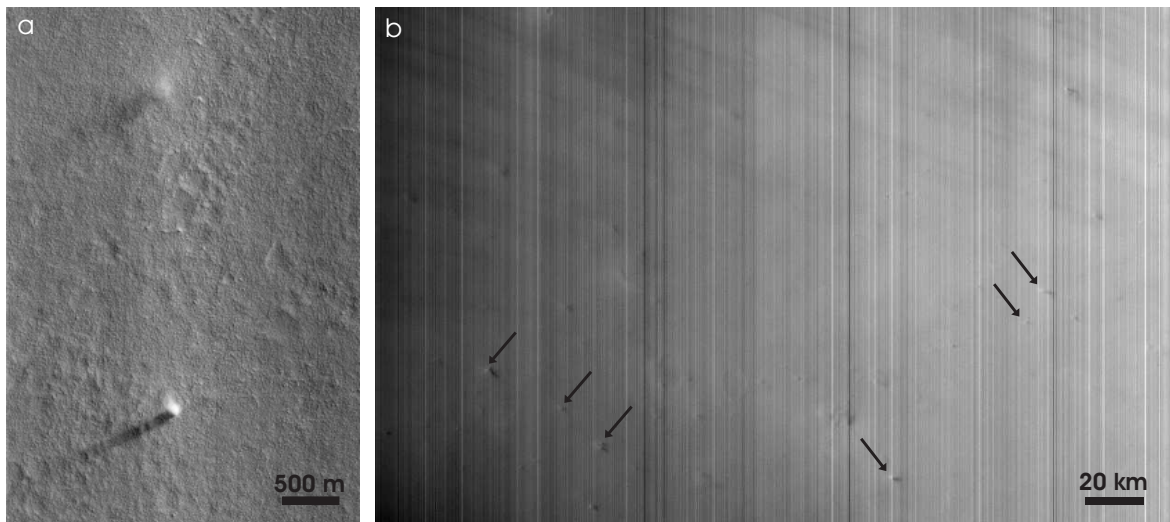


**Figure 7.22:** a) MOC Narrow Angle image e05-02077. The lower dust devil was correctly classified, the upper one has a too weak bright spot so that nothing was filtered. b) MOC Wide Angle image e03-00363. The black arrows indicate dust devils which are hardly detectable because of the brightness gradient which makes the left side quite dark, and the right side quite bright. Additionally, the dark and bright stripes are seen which complicate a correct classification.

no improvement. Worth mentioning is the effect of the bright and dark stripes in the MOC images since sometimes the shadow concatenates with a dark strip and is then ruled out as a dust devil shadow by the classifier because of the strange  $\phi$  value (Figure 7.22b). For WA image m01-02674 it was once tested to run the pattern recognition and classification software with and without the  $\phi$  checking. With  $\phi$  check the search resulted in 5 detected dust devils, without the check in 18 objects with 12 clearly identifiable dust devils (including the former detected 5 dust devils). Other detections are hills or not explicitly assignable objects. This would suggest to deactivate the  $\phi$  check or allow a wider range of permitted  $\phi$  values when processing MOC images.

Beside the adjustments of the pattern recognition parameters  $n$  (bright spot filtering) and  $\phi$  (shadow orientation) no further changes were necessary to apply to the existing software as it was anticipated (see Section 6.3). Despite the differences in image resolutions and sizes the software could handle the data from the NA and WA camera without problems after flipping the images left-to-right if required. The analysed images represent of course only a small part of the large database of MARS GLOBAL SURVEYOR MOC images. Nevertheless, the positively classified objects are almost all dust devils which show the capability of the software to detect dust devils in MOC images as well.



---

## DUST DEVILS: THE SCIENTIFIC INVESTIGATION

---

A total of 205 dust devils have been observed as of July 2007 in HRSC images from 23 different Mars Express orbits. The observations range from January 2004 to July 2006, covering northern and southern hemispheres at various seasons. First, no systematic search for dust devils was performed, such as choosing certain regions for dust devil examination. The early focus, however, was on the northern lowlands, in the spring and summer for images taken between 0600 and 2000 hours local time. These conditions referred to the knowledge and assumptions of previous dust devil studies (see Chapter 2). Later it was not concentrated on the season for the respective hemisphere, nor was any importance attached to the local time of observations but several regions were examined. One focus was on Amazonis Planitia where many dust devils have been found (Cantor et al., 2002; Fisher et al, 2005; Cantor et al., 2006). The details of each orbit where dust devils have been detected, as well as the dust devil characteristics (speeds, diameters and heights) are listed in Table D.1 in Appendix D.

### 8.1 Spatial and Temporal Distribution

70 dust devils were found in the southern hemisphere between  $50^{\circ}$  and  $62^{\circ}$ S latitude at local summer,  $L_s = 281^{\circ}$  to  $317^{\circ}$  (Figure 8.1). They have not been detected in any single region, but occur in areas from  $14^{\circ}$ E (Noachis Terra, orbit 2225) to  $170^{\circ}$ E (Terra Cimmeria, orbit 2315). The orbits 2100 and 2242, covering this special latitude range, contain each 26 dust devils giving a total of 52 dust devils. The local conditions were favourable for dust devil development. Another three orbits on the southern hemisphere (orbits 2032, 2054, 3210) showed eight dust devils in Syria Planum (Table D.1, Figure 8.1), whereas one dust devil

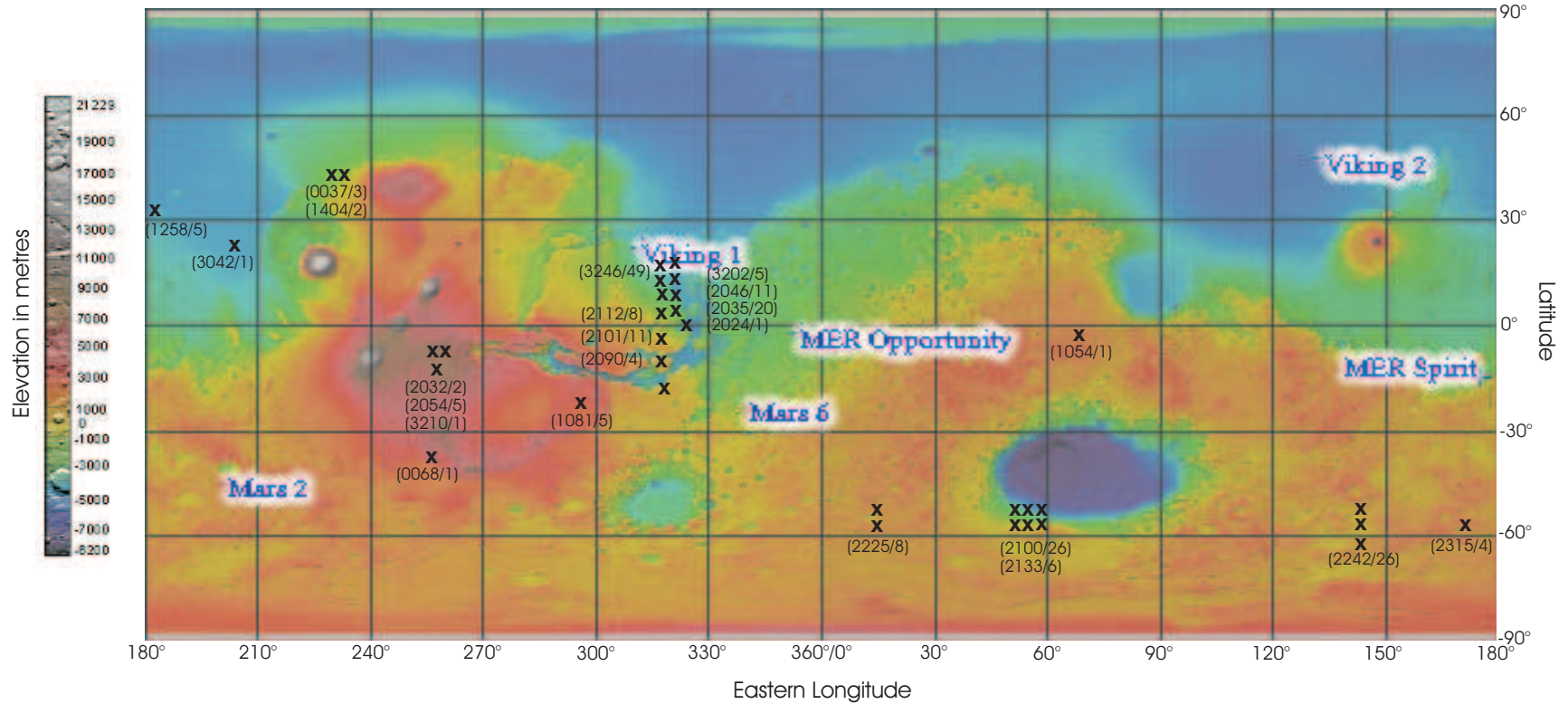


**Figure 8.1:** Coloured topography map based on Mars Orbiter Laser Altimeter (MOLA) data. Dust devil locations detected by HRSC are indicated by the big crosses. Note that one cross does not always represent one orbit/image and mostly not one single dust devil. The crosses stand for the spatial coverage where dust devils have been detected. The numbers in parentheses belong to the above lying crosses except for crosses below the VIKING 1 lander region, where the dedicated parentheses are right or left of the crosses. The first number represents the orbit number, the second the number of dust devils seen in this orbit. Highlighted are the landing sites of probes from different missions. The Mars Pathfinder landing site is located at 19°N, 327°E, covered by the VIKING 1 writing.

(orbit 3210) was found at local autumn. Four of the dust devils in Thaumasia Planum (orbit 1081; dust devils 2, 3, 4 and 5) were detected in all three stereo images. One (dust devil 1) was seen only in the nadir and backward looking image because it was out of the field of view of the forward-looking channel (see Figure 8.4, page 96). These dust devils are the only ones detected in the southern hemisphere during the winter ( $L_s = 118^\circ$ ). The relatively small dust devil in orbit 0068 (Icaria Planum) is only seen in the ND and S2 channel but at a low quality. A dust cloud is found near the equator (orbit 1054) in Syrtis Planum.

Dust devils observed in the northern hemisphere are six dust devils in Amazonis Planitia (orbits 1258 and 3042) and five in Arcadia Planitia (orbits 0037 and 1404). The three dust devils in orbit 0037 were the very first dust devils discovered by HRSC. They are located in the same region where *Thomas and Gierasch* [1985] found the first dust devils on Mars from VIKING images. Further remarkable is that they occurred at local winter ( $L_s = 337^\circ$ ).

One target area was Chryse Planitia, a northern lowland ( $12\text{--}41^\circ\text{N}$ ,  $305\text{--}334^\circ\text{E}$ ). Most of the available HRSC images, however, covered only the southern part of Chryse Planitia and extended sometimes to Noachis Terra ( $20^\circ\text{S}$ ), crossing the equator and Valles Marineris (Figure 8.1). Nevertheless, these orbits were fully analysed by the pattern recognition and classification software and revealed a high number of dust devil detections in the longitude range of  $317\text{--}326^\circ\text{E}$  and between  $20^\circ\text{N}$  and  $20^\circ\text{S}$ . 55 dust devils seen in six orbits were imaged within 32 Mars days ( $L_s = 267\text{--}283^\circ$ ). Depending if the dust devils were imaged on the northern or southern hemisphere, the season is northern winter or southern summer. In northern spring ( $L_s = 76\text{--}82^\circ$ ) 54 dust devils were imaged (orbits 3202 and 3246). The season seems not to be the dominant factor that dust devils evolve in such a high number because of the location near the equator. Valles Marineris disembogues into Simud Vallis, and Simud Vallis finally into Chryse Planitia. There is maybe a flow field induced by this valley system and the surrounded highlands that force dust devil formation.

The high amount of 109 dust devils seen between  $20^\circ\text{N}$  and  $20^\circ\text{S}$  at  $317\text{--}326^\circ\text{E}$  must not be overvalued with respect to the other dust devil locations. Every image covering these regions were examined for dust devil occurrences, whereas the other detections are rather individual cases of different regions.

HRSC data were compared to results from other orbiter data [*Whelley and Greeley*, 2006; *Fisher et al.*, 2005; *Cantor et al.*, 2006]. *Whelley and Greeley* [2006] found a dust devil 'season', similar to results of *Malin and Edgett* [2001] and *Cantor et al.* [2006]. The season begins in late spring, continues through summer into mid fall for the respective hemisphere. However, *Whelley and Greeley* [2006] found that the frequency of tracks in the southern hemisphere is an order of magnitude larger, which was attributed to differences in heating due to orbital asymmetries. The highest frequency was between  $50^\circ$  and  $60^\circ\text{S}$  latitude, consistent with our HRSC data ( $\sim 34\%$  or 70 of 205 dust devils seen in this latitude range). This is in contrast to *Cantor et al.* [2006] who found in MOC images over 88% of about 11500 active dust devils in the northern hemisphere (with over 99% of northern hemisphere dust devils in Amazonis Planitia alone). So far a total of 87 HRSC orbits (January 2004 to July 2006) covering Amazonis Planitia were examined, including all seasons and ranging in local time from morning to late afternoon. Only six dust devils were detected in two orbits (1258 and 3042). These Amazonis orbits, however, cover often the latitude range between  $0\text{--}30^\circ\text{N}$ ,

which is a region where *Cantor et al.* [2006] noted that dust devils are absent.

No special remark is made by *Cantor et al.* [2006] about numerous occurrences between 50° and 60°S latitude. They note, however, that between 0° to 40°S at various longitudes no dust devils at all have been seen in WA images. The majority of dust devils in NA observations occurred outside a longitudinal band spanning from 18-23°S [*Cantor et al.*, 2006]. This strengthens our findings of the latitude range of active dust devils seen on the southern hemisphere. We have also detected dust devils (orbit 0068, Icaria Planum; orbit 1081, Thaumasia Planum) where *Cantor et al.* [2006] have never seen one dust devil in their comprehensive search in the MOC database. This suggests that the detection of dust devils is still highly variable and depends strongly on the local time and season when the images are taken and on the image resolution. Talking about the spatial distribution of dust devils requires to include all available results from different Mars orbiters and landers at the best.

In addition to the high number of active dust devils, HRSC dust devil tracks were only seen in those five orbits (from a total of 23 orbits with active dust devils) that cover the 50° to 60°S latitude range. This strengthens the argument of *Whelley and Greeley* [2006] that asymmetries in dust deposits are responsible for the paucity of tracks in the northern hemisphere in comparison to the southern hemisphere (see Figure 8.6, page 101).

The highest dust devil track frequency is found in the northern hemisphere between 60° and 70°N, as seen in MOC images [*Whelley and Greeley*, 2006]. This was not observed by HRSC data, as no active dust devils were seen north of 43°N. Most dust devils seen in the northern hemisphere were detected in the southern parts of Chryse Planitia. *Fisher et al.* [2005] detected three active dust devils (local winter) and four dust devil tracks (local summer and winter) in this region. *Metzger et al.* [1999] showed using MARS PATHFINDER lander images that this is an active dust devil region. Taking these results and those from *Whelley and Greeley* [2006] into account, there is a possible explanation for the high number of active dust devils seen in Chryse Planitia. It is a region of higher surface pressure (lowland) with a thick dust layer which favours dust devil formation. The flow field of the southerly located valley system may play a role, too, as mentioned above.

All dust devils detected by HRSC occurred at noon or afternoon with a peak between 1400 and 1600 hours, as on Earth [*Sinclair*, 1969; *Snow and McClelland*, 1990] and in previous Mars studies [*Wennmacher et al.*, 1996; *Balme et al.*, 2003b; *Greeley et al.*, 2006]. Eight orbits showed also dust devil activity in local winter and local autumn beside the dust devil season in spring and summer. The locations, however, are sometimes near the equator.

A diurnal distribution of dust devil occurrence cannot be retrieved from MOC data, since the observations are limited to 1400-1500 hours local time. The distribution of dust devils seen in HRSC data compare favourably with terrestrial observations where dust devil activity starts in the morning hours around 1000-1100 hours, peaks at 1300-1400 hours, and tends to vanish after 1600-1700 hours [*Sinclair*, 1969]. The local time of dust devil occurrence is in agreement with the near-maximum heating of the ground and the overlying air [*Thomas and Gierasch*, 1985]. HRSC imaged dust devils in all seasons on both hemispheres, with most seen in the spring and summer. Summarising the regions and the seasons when dust devils have been observed, our data support the hypothesis that dust devils evolve wherever the atmospheric conditions are suitable [*Cantor et al.*, 2006].

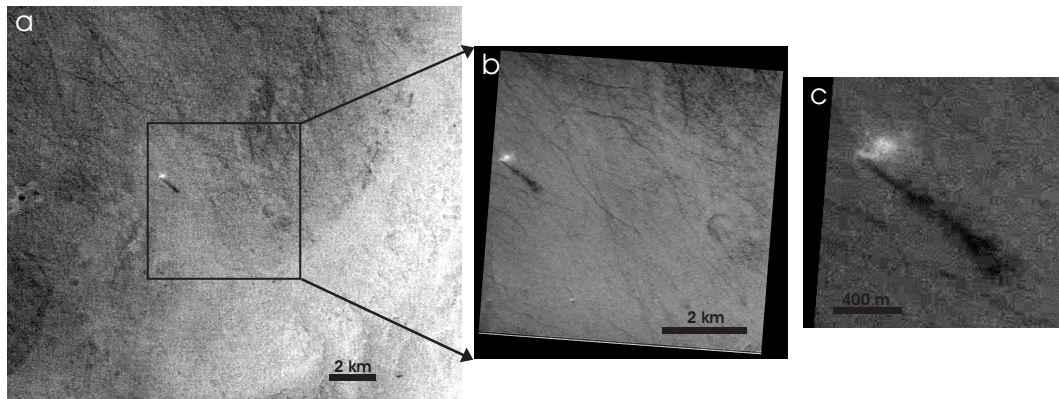


**Figure 8.2:** *a) Dust devil in Peneus Patera seen in the ND image (orbit 2133, resolution 25 m/pixel). The black square outlines the location of the SRC image. b) SRC image (resolution 5 m/pixel) revealing many more dust devil tracks than seen in the ND image. c) An enlargement of the dust devil seen in the SRC image, showing the kink between the lower and the upper part of the dust devil. North is to the top of each image.*

## 8.2 Dimensions

The diameters of most observed dust devils were between 100-400 m (Table D.1). Clear exceptions were two features that lacked well defined vortices, which are most likely large dust clouds with  $\sim 1010$  and  $\sim 1430$  m across. The largest dust devil seen in HRSC images was  $\sim 1650$  m in diameter and  $\sim 4440$  m high, while the smallest diameter was  $\sim 45$  m and the lowest height  $\sim 75$  m measured for the same dust devil. The average size was  $\sim 230$  m in diameter and  $\sim 660$  m in height, consistent with the findings of narrow angle (NA) MOC images by *Fisher et al.* [2005]. Heights of 3.8 to 8.5 km were found in wide angle (WA) MOC images where only the large dust devils can be detected.

Sometimes it is difficult to determine the diameter directly from the dust devil column because it has no well-defined shape or the column is tilted. Then the diameter is measured from the width of the shadow. The error in diameter measurements is assumed to be five image pixels, that is  $\sim 63$  m with the best resolution of 12.5 m/pixel in the ND image. The error in the height measurement depends on the length of the shadow and the sun incidence angle and is therefore variable for each dust devil. A better resolution like available in SRC images can help to correct the found values of dust devil dimensions.

So far only one dust devil was observed by both the HRSC and the SRC (Figure 8.2) on the caldera floor of Peneus Patera. This is very fortunate because SRC images are not obtained on every orbit and they typically cover only a small strip embedded in the centre of the nadir images. The SRC observation during orbit 2133 was designed to be a N-S raster mode observation transecting the caldera floor and the dust devil column and its shadow are clearly visible. The dust devil is almost at the image border of the SRC image. Nevertheless, this example shows the potential of the SRC. While the resolution of the ND channel was only 25 m/pixel (Figure 8.2a), the SRC image at 5 m/pixel reveals more details of the structure of the dust devil, as well as of the surrounding environment (Figure 8.2b). In addition, streaks inferred to be dust devil tracks can be identified and placed in the broader context of the

HRSC image, suggesting that the floor of Peneus Patera is covered with dust.

The dust devil is tilted in the direction of the shadow which can be seen in the ND image. The analysis of the SRC image shows a clear ‘kink’ between the lower, thinner, columnar vortex, and the upper broad, expanded vortex (likely due to wind shear) of the dust devil (Figure 8.2c). The kink is in the direction of the shadow and cannot be seen in the shadow itself, so its altitude cannot be retrieved.

The direction of tilt of dust devils is assumed to indicate their direction of motion [*Rennó et al.*, 2000; *Greeley et al.*, 2006]. The sequential position of the dust devil is in the direction of the kink, in agreement with the first position seen. We conclude that the wind shear tilts the dust devil in the wind direction and that the ambient wind moves it forward.

The better resolution of SRC also enabled a better measure of the dust devil diameter. For example, the lower columnar vortex appeared to be 90 m in the HRSC ND channel, but 42 m in the SRC image. This suggests that the diameters obtained for the HRSC ND are over-estimates. We found no significant difference in the shadow length and therefore the height (1352 vs. 1366 m), between the HRSC ND and SRC data.

### 8.3 Traverse Velocity

The unique imaging capability of the HRSC enables the forward velocities of dust devils to be computed from their positions seen in the three stereo channels. The time when the dust devils were imaged is given in the binary prefix of each image. Dust devils could not always be recognised in all three HRSC images, either because they disappeared in the time between acquisitions of two HRSC channels, or because the image resolution of an individual channel was too low. Typically, the Martian surface is imaged with the ND channel at the best resolution (12.5 m/pixel) and with the S1 and S2 channels at 25 m/pixel. Repeated observations of regions using the full-resolution stereo mode of the HRSC include ND, S1, and S2 channels at 12.5 m/pixel. Nevertheless, all calculations of dust devil diameter and height, discussed above, were done using the highest resolution data, typically the ND channel.

We estimate the error in the recorded dust devil position (centre of plume) to be 5 pixels ( $\sim 63$  m at highest resolution in nadir image) for the image lines and samples, respectively. The total error is then approximately  $\pm 177$  m for the travelled distance between two positions of the dust devil. The uncertainty in dust devil position also leads to an uncertainty in time when the dust devil was imaged. The time error depends on the spacecraft altitude and speed, and is in most cases less than  $\pm 0.1$  s. Errors in position and time affect the value of the derived dust devil speeds and are taken into account in Table D.1. These errors are not of the same kind as time and range errors in measurements on Earth where one observes the dust devils in field studies in mostly horizontal views [*Snow and McClelland*, 1990]. The size, height and travelled distance must be estimated in a relatively short time. For Mars with HRSC, we have three images and mostly three clear positions of the dust devils.

The larger part of the detected dust devils has a forward motion range from a few metres per second up to 15 m/s (Table D.1). These values are in good agreement with observations of

dust devils on Earth [Sinclair, 1969; Snow and McClelland, 1990] and with predictions for Mars [Ryan and Lucich, 1983; Metzger et al., 1999; Rennó et al., 1998; Ferri et al., 2003]. The average speed for 74 dust devils, however, was 23.1 m/s with a range from 15.0 to  $\sim$ 59 m/s (Table D.1). The question is if these results can be regarded as near-surface wind values or if the high speeds result from observations of the dust column at higher altitudes and therefore reflect the wind speed at this altitude.

We used wind speed profiles derived from the Martian Climate Database [Lewis et al., 1999] for a given local time, season, and region. These profiles were compared with the derived dust devil speeds and heights of the first four orbits where dust devils have been seen (orbits 0037, 1054, 1081 and 1258, see Stanzel et al. [2006]). Figure 8.3 shows an example for dust devil 4 in Thaumasia Planum (orbit 1081). This dust devil was approximately 3.4 km high and travelled at 19.6 m/s, corresponding well with the wind profile speed at the altitude of 3.4 km. It seems that the speed was measured at the upper part of the dust devil and therefore represents a value of the wind speed at this altitude, with a speed of only a few meters per second at the surface. This is consistent with most of the observed dust devils except for dust devil 1 and 5 in Thaumasia Planum and those in Amazonis Planitia (orbit 1258).

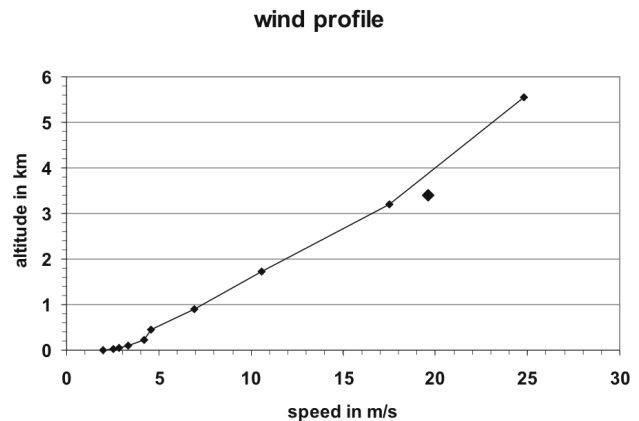


**Figure 8.3:** Wind speed profile from the Martian Climate Database for the given local time, season and region of dust devil 4, Thaumasia Planum. The dust devil travelled at 19.6 m/s on average with a height of 3.4 km (indicated by the big diamond).

According to the predicted wind profiles of the database, the smaller dust devils 1 and 5 in Thaumasia Planum should move at 4 to 7 m/s but also those dust devils have a forward speed of 16.9 and 20.8 m/s like the other three higher dust devils in Thaumasia Planum. It is remarkable that the five dust devils move almost in-line in the same direction although several kilometres separated from each other (Figure 8.4). They have maybe formed along an air mass boundary, and move forward at that high speed because of the high wind speeds existing along fronts and shear lines.

The dust devils in Amazonis Planitia have heights of 0.9 to 1.4 km, suggesting a wind speed of 9.5 to 13.5 m/s from the Martian Climate Database for this altitude, but the observed speeds are 1.5 to 6.0 m/s. It seems that in this case the real near-surface forward speed of the dust devils was measured and not the wind speed at a higher altitude.

The intersection of the shadow with the plume (interpreted as the vortex) defines the surface point which is tracked in each image. If the high speeds result from observations of the plume at higher altitudes and not directly from the surface, the parallax error has to be taken into account because of the tilted viewing direction ( $18.9^\circ$ ) of the stereo channels (see Section 4.3).

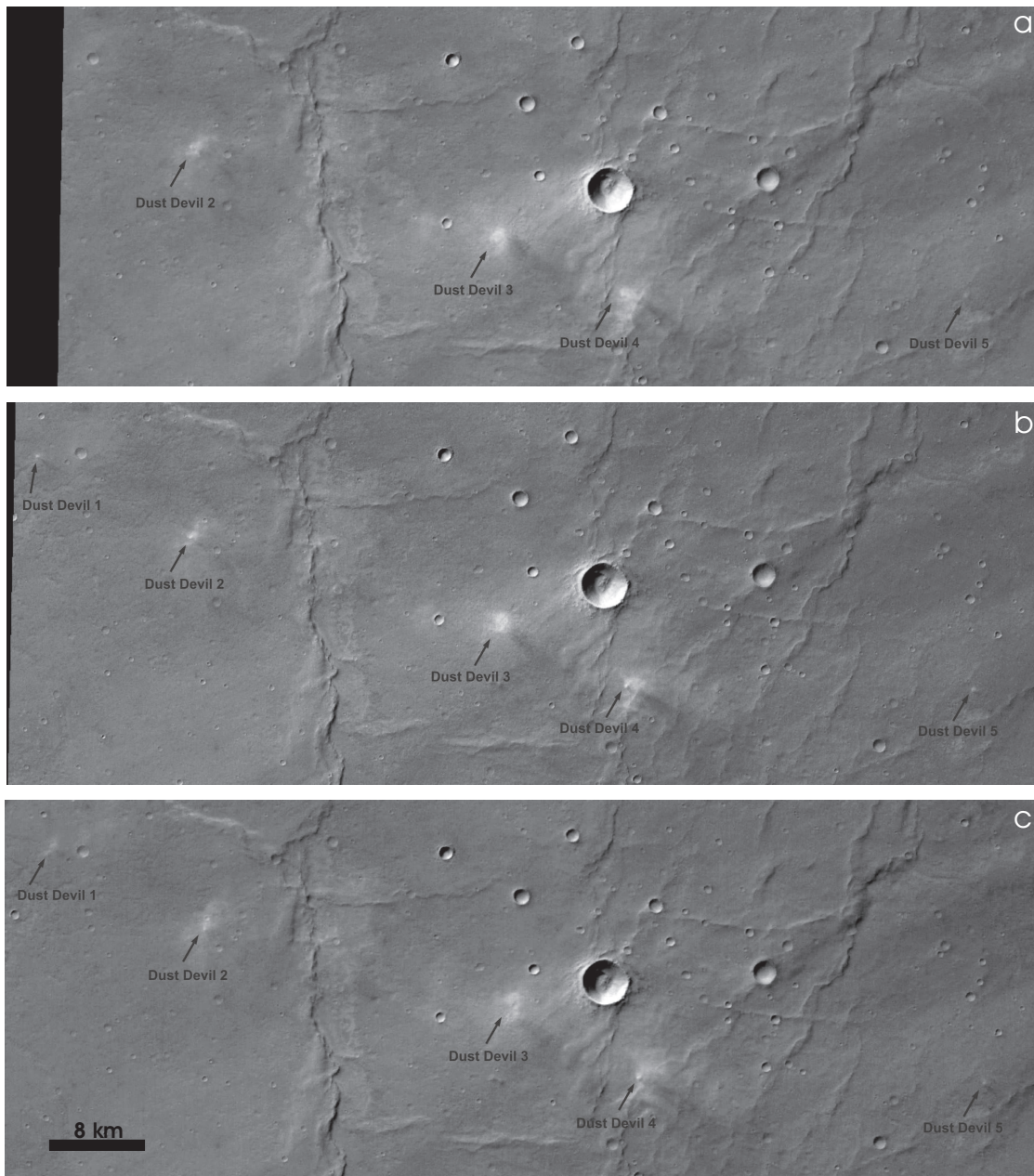


**Figure 8.4:** HRSC stereo images showing five dust devils in Thaumasia Planum. The illumination is from the upper left. North is to the top of each image. a) Stereo 1 forward looking channel. b) Nadir image showing the change in position of the dust devils after 44 s. Note that dust devil 1 entered the field of view. c) Stereo 2 backward looking channel showing the change in position of the dust devils after 53 s after nadir image (97 s after S1 image).

The parallax error leads to an error in the distance and hence the speed (Table 8.1). Speeds are between 10.6 to 14.4 m/s for the dust devils in Amazonis Planitia which had before only a few metres per second. The speed results showed no major changes for dust devils in the other regions (Table 8.1). Values between 12.1 to 24.8 m/s correspond well with former results without parallax error. The parallax has no effect because the dust devils moved a much larger distance than those in Amazonis Planitia. The derived speeds are therefore interpreted as near-surface values. This is underlined by the impression of the images. Figure 8.4 shows that in the S1 and S2 images the top of the dust devils is tilted forward and backward (best

Dust Devil Number	Channels	speed, m/s without	speed, m/s with parallax	Dust Devil Number	Channels	speed, m/s without	speed, m/s with parallax
<i>Thaumasia Planum, Image = h1081_0000</i>				<i>Amazonis Planitia, Image = h1258_0001</i>			
1	ND-S2	20.8	19.1	1	S1-ND	2.2	13.1
					ND-S2	6.0	13.2
					S1-S2	4.1	13.1
2	S1-ND	22.7	23.2	2	S1-ND	3.2	10.6
	ND-S2	18.8	16.9		ND-S2	1.8	11.3
	S1-S2	20.6	19.7		S1-S2	2.5	10.9
3	S1-ND	20.0	12.1	3	S1-ND	1.6	14.4
	ND-S2	15.0	15.0		ND-S2	1.5	13.6
	S1-S2	16.3	12.9		S1-S2	1.6	13.8
4	S1-ND	21.4	23.1	4	S1-ND	5.8	11.4
	ND-S2	17.8	21.9		ND-S2	2.7	14.0
	S1-S2	19.4	22.4		S1-S2	4.1	12.7
5	S1-ND	16.8	15.7	5	S1-ND	5.6	11.1
	ND-S2	16.9	16.3		ND-S2	5.1	12.3
	S1-S2	16.8	16.0		S1-S2	5.2	11.6

**Table 8.1:** Dust devil speeds computed once with the parallax error and once without. The dust devils seen in *Thaumasia Planum* had anyway a high forward speed. The parallax has no effect. The speeds with the parallax error for the dust devils in *Amazonis Planitia* are unrealistically high in contradiction to the impression by the images where the dust devils moved only a small distance.

seen at dust devil 3) due to the parallax. And this it not the surface point where the speeds are measured [Stanzel *et al.*, 2006].

Assuming that the computed speeds are near-surface values leads to two possibilities of interpretation. First, if dust devils do move with the environmental wind, this ambient wind has a higher speed than usually assumed (5 m/s) when dust devils occur. However, dust devils have not been seen at high wind speeds (>10 m/s) very often in terrestrial investigations. Second, the ambient wind is only a few metres per second, then the dust devils move much faster and have a strong forward component beside the high rotational and vertical velocities independent from the environmental conditions. Most observations show that dust devils from a single image move in the same direction despite their distances and have approximately the same speed. This underlines the assumption of movement with the current ambient wind.

One explanation for the relatively high speeds of the five dust devils detected in *Thaumasia Planum* (Figure 8.4), which moved all in one row, is that they may have developed at an air mass boundary [Stanzel *et al.*, 2006]. We infer that they moved across the surface at high wind speeds that are found along such fronts. No environmental explanation, however, could be provided for the relatively high speeds of the dust devils in *Arcadia Planitia* (orbit 0037) and *Syrtis Planum* (orbit 1054).

Two orbits covering *Syria Planum* (2032 and 2054) showed seven dust devils and revealed another explanation for their relatively high speeds. The images, taken only 7.4 Mars days apart from each other, include a small and a large dust storm. Cantor *et al.* [2006] showed several MOC images where large dust devils and plumes occurred at the fronts of dust storms. They relate them to terrestrial vortices accompanying passing storm fronts. So the dust storms

seen with HRSC may be responsible for the fast motion and the initiation of the dust devils. The dust devils seen at the front of the storm indicate with their computed speeds as well the speed of the dust storm if they are propelled by the storm. This is supported by the simulations of *Toigo et al.* [2003] where dust devils developed both in the 'highest wind speed' case and in the 'no background wind' case.

Former investigations concerning dust devils on Earth and Mars assumed that high ambient wind speeds suppress dust devil formation and evolution and that measurements of high forward motions are due to measurement errors [*Snow and McClelland*, 1990]. *Kanak* [2006] did a survey of numerical simulations of dust devil-like vortices for both Earth and Mars. The review revealed that dust devil-like vortices occurred in all simulations despite differences in the models, initial conditions, or experimental designs. Three of four studies of the Martian atmosphere included ambient wind and were mostly run at low wind conditions. *Michaels and Rafkin* [2004] noted that there is an influence of background wind which was overcome by afternoon heating, which is an important issue on Mars. The potential intensity of convective vortices depends on the thermodynamic properties of the environment, while the vortex radius of maximum wind depends on both the thermodynamic properties and the value of the ambient vorticity, in agreement with *Rennó et al.* [2000] and *Rennó and Bluestein* [2001]. Combining this theory and the results from HRSC leads to the suggestion that dust devil formation is not suppressed by high wind speeds. The dust devil speeds are a few metres per second as reported in most cases [*Ryan and Lucich*, 1983; *Metzger et al.*, 1999; *Rennó et al.*, 1998; *Ferri et al.*, 2003] if ambient winds are low or non-existent. Dust devils exist at and move with high wind speeds as well, including the best developed and largest dust devils observed with HRSC (Figure 8.4).

After the analysis of almost 200 dust devil speeds it can be concluded that dust devils move with the ambient wind as it always was expected. The derived speeds of dust devils seen in one orbit are consistent and all dust devils despite their distances moved in the same direction. The derived speeds can therefore be taken as an indirect measurement of the surface wind speeds.

The orbits 2035 and 2046 showed speeds up to 30 m/s on average, with some exceptions of over 40 and 50 m/s. These speeds seem to be unrealistically high and are mostly due to the fact that the observed objects represent more dust clouds than dust devils. A specific near-surface point can therefore not be tracked because no clear vortices are seen. This leads to the high speeds and the usually assumed error in speed measurements should be estimated much larger for these cases. It is assumed that the real speed is about 30 m/s as calculated for the other dust devils in the orbits. The high speeds in the Simud Vallis regions were referred to a possible flow field forcing dust devil formation.

Another consequence of high wind speeds according to theory [*Rennó et al.*, 2000] is that the diameters of maximum wind of dust devils, and therefore the diameter of the dust devils themselves, tend to be larger with high wind speeds (increase in ambient vorticity). No such correlation is apparent in the HRSC data, however. Only the dust devils in Amazonis Planitia have diameters <100 m and low speeds. There are, however, dust devils in Syria Planum (orbit 2032) with small diameters of 80 and 138 m and average speeds of 20 m/s. The diameters of the dust devils in Xanthe Dorsa (orbit 3246) range from 60 to 530 m, but

the speeds do not increase with diameter. The largest diameters (orbit 2054) have been seen at high speeds. However, the images of the three stereo channels are ‘snap-shots’ and do not indicate longer duration observations. The smaller dust devils formed at high speeds might have just formed and were still growing [Rennó *et al.*, 2000].

## 8.4 Dust Devil Tracks and Lifetime

Wind streaks interpreted as dust devil tracks are common in SRC image mosaics. Fifteen mosaics (Table 8.2) have clearly identifiable tracks, ranging from linear to curved and from two to 512 individual tracks per mosaic [Williams, 2007; Whelley, 2007]. Most of the tracks seen in SRC are also in the 50-70°S latitude range as seen by Whelley and Greeley [2006]. Four mosaics on the northern hemisphere show tracks between 50-70°N which corresponds with MOC results as well. The high frequency of tracks supports the high number of active dust devils in these latitude ranges and the argument that the Hadley cell is the main causer. All streaks are dark except for those found on the south slope of the Pavonis Mons caldera and within the Arsia Mons caldera (Figure 8.5), which are bright.

The occurrence of bright dust devil tracks, indicative of the removal of darker materials superposed on brighter surfaces by dust devils, is relatively rare in both HRSC and SRC images (Table 8.2). In SRC images the only occurrences of bright tracks are within the calderas of the Tharsis Montes. 95% of the detected dust devil tracks on the floor of the Arsia Mons caldera on orbit 0263 ( $L_S = 13.5^\circ$ , local autumn; local time 13:15, Figure 8.5) were bright, roughly 5% were dark [Stanzel *et al.*, 2007]. The fine, diffuse, white, sublinear tracks seen in the Arsia summit caldera were previously observed on MOC images [Malin *et al.*, 2003]. Malin and Edgett [2001] also reported streaks on the summit of Olympus Mons. At an elevation of 16.3 km, the atmosphere at the Arsia summit caldera is extremely thin ( $\sim 1$  hPa or comparable to Earth’s atmosphere at an altitude of  $\sim 40$  km). Dust is very dif-

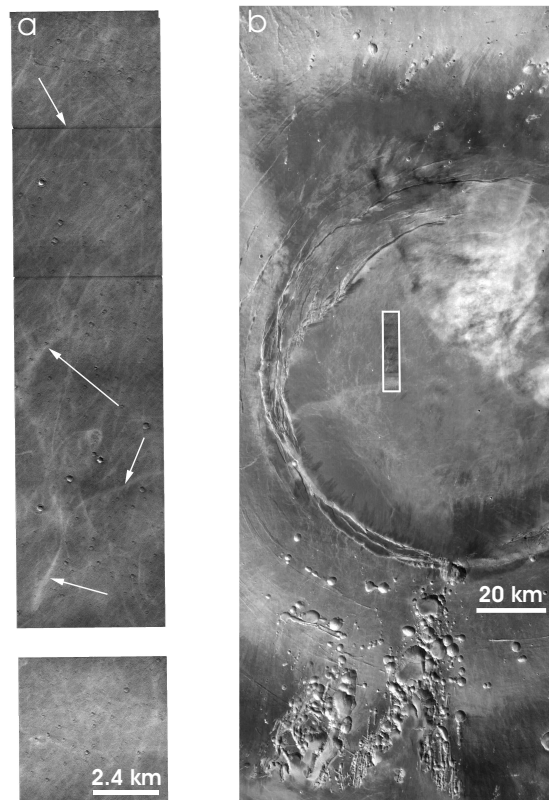


**Figure 8.5:** HRSC-SRC images taken during orbit 263 imaging Arsia Mons caldera. North is to the top. a) SRC mosaic of part of the caldera, showing bright dust devil tracks (white arrows). b) HRSC image of the Arsia Mons caldera, showing the location (white box) of the SRC mosaic. The white zone obscuring the right side of the caldera is thought to be a water-ice cloud. By courtesy of D. Williams.

Orbit	Location	Track Morphology	Number of Tracks	Track Albedo
0016 (Frames 10-16)	3.0°S, 256.6°E N of Noctis Labyrinthus	linear	2	dark
0030	38.4°S, 61.3°E Hellas Planitia	linear to sublinear	38	dark
0263	9.1°S, 239.2°E Arsia Mons caldera	sublinear to curved	268	bright
0383	49.5°S, 321.7°E Argyre Planitia	linear	2	dark
0891	0.3°N, 247.4°E Pavonis Mons caldera S slope	curved	26	bright
1269	65.2°N, 177.8°E Vastitas Borealis	linear to curved	316	dark
1475	67.5°N, 81.6°E Vastitas Borealis	linear	9	dark
1607	51.7°N, 71.7°E Northern lowlands	linear to curved	184	dark
2133	57.7°S, 53.4°E Peneus Patera caldera	linear to curved	512	dark
2148	46.9°S, 20.0°E Noachis Terra, crater Kaiser	sublinear to curved	419	dark
2209	71.6°S, 139.5°E Planum Chromium	sublinear to curved	422	dark
2293	62.0°S, 171.6°E Terra Sirenum (near dark dunes)	sublinear to curved	81	dark
2295	63.1°S, 334.8°E Noachis Terra	sublinear to curved	218	dark
2315	61.6°S, 169.8°E Planum Chromium	sublinear to curved	443	dark
2418	71.9°S, 127.6°E Planum Chromium	sublinear	170	dark

**Table 8.2:** Dust devil tracks found in SRC mosaics through orbit 3354 (August 2006). By courtesy of D. Williams.

difficult to move in such a rarefied atmosphere, requiring wind speeds of some 200 m/s [Greeley and Iversen, 1985]. However, the low-pressure central cores of dust devils are very efficient in the removal of fine particles [Greeley *et al.*, 2003]. It is not known if these tracks reflect recent dust devil activity or are relicts of a previous climate when the atmosphere might have been of higher density. Malin and Edgett [2001] report dust devil streaks at all elevations and at almost all latitudes from MOC image analysis.

More dust devil tracks are seen than active dust devils themselves. Fisher *et al.* [2005] reported that they detected many tracks, but not a single active dust devil in their search of Casius and Utopia Planitia. However, dust devils are occasionally observed creating new tracks seen from Spirit [Greeley *et al.*, 2006], and from orbit in MOC images [Cantor *et al.*, 2006]. Seven active dust devils were observed with HRSC in orbit 2225 leaving tracks in southern Noachis Terra (Figure 8.6). They are surrounded by an abundance of other streaks.

Assuming that dust devils create tracks once they start moving and that they collapsed where the streaks terminate, we computed the potential lifetime of dust devils by using the measured

speeds of active dust devils and the lengths of their tracks. Tracks created by observed dust devils were used along with tracks in the vicinity of dust devils 3-6 (Figure 8.6) in orbit 2225 (Table D.1). The assumed speed for the tracks is 6 m/s, which is the average for the four active dust devils. The shortest life time was less than four minutes for a dust devil which moved  $\sim 1850$  m at 8.4 m/s. The longest life time was about 32 minutes for a distance of 11.7 km at 6 m/s. The mean value for 12 analysed tracks is about 13 minutes.

It was noted by *Sinclair* [1969] that most terrestrial dust devils last only for a few minutes, with some as long as 20 minutes, although some exceptions of several hours duration are mentioned. Long durations occur when dust devils are stationary, and if there is sufficient warm air and a supply of particles [Ives, 1947]. *Snow and McClelland* [1990] came to similar conclusions. In addition, the duration depends on the size of dust devils with larger dust devils lasting longer and travelling further. These relations appear to be true on Mars as well. The computed lifetimes for Martian dust devils may be a lower limit because the visible dust devil is used as the end point, and the vortex is likely to continue to exist even without entrained dust. The tracks are used as a measure for the travel distance (including the starting point), but as stated above and as seen in most of the HRSC orbits, dust devils may occur without leaving visible tracks.

That dust devils are temporally highly variable could be additionally seen in some orbits where dust devils developed between two stereo image acquisitions. The time difference between two images is also sufficient to observe the collapse of dust devils.

No well-defined dust columns and only smeared shadows can be detected in sequent images. Understanding the duration of Martian dust devils is important to obtain a better estimation of the dust entrainment into the atmosphere based on frequency, size, and flux of dust of dust devils.

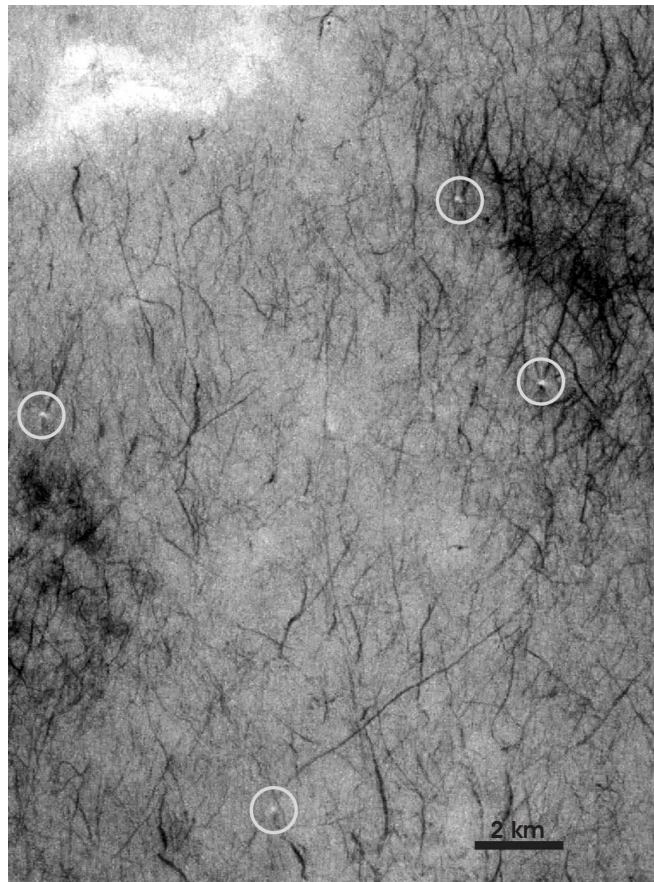


**Figure 8.6:** Nadir image of Noachis Terra (orbit 2225) showing four dust devils (outlined by white circles) and their tracks. North is to the top of the image.

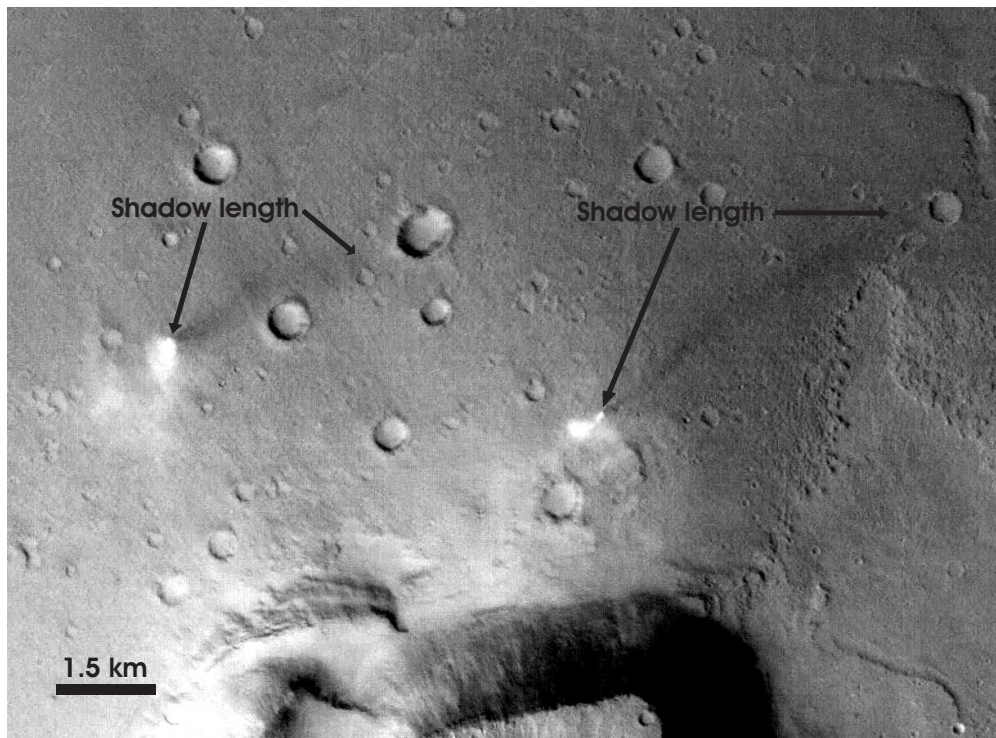


**Figure 8.7:** Two dust devils (Chryse Planitia, orbit 2046) with partly slender dust columns but very long shadows indicating a larger height. The height was 1740 m for the left, and 2840 m for the right dust devil. North is to the top.

## 8.5 Dust Lifting Rates of Dust Devils

The magnitude of the dust flux and the mechanism of dust entrainment into the atmosphere remain uncertain. *Neakrase et al.* [2006] simulated the dust flux in dust devils for various laboratory settings. Smaller, tighter vortices are more efficient in lifting dust. The dust flux increases with larger pressure wells. This is confirmed by the theoretical work of *Balme and Hagermann* [2006] showing the efficiency of the pressure difference in particular for smaller particles lifted by small and fast dust devils. The quantitative analysis by *Greeley et al.* [2006] using SPIRIT data demonstrates the large amount of dust which is lifted by many small size dust devils. These simulations, theories, and image analyses prove the contribution of dust devils to the dust cycle of Mars. Larger dust devils as seen by HRSC (Figure 8.7) can carry dust several kilometres high where it may remain in suspension. Depending on their longer lifetime and larger size the HRSC dust devils provide an additional contribution to the amount of lifted dust of  $19 \text{ kg/km}^2/\text{sol}$  calculated by *Greeley et al.* [2006].

We computed the amount of dust lifted by typical HRSC dust devils (diameter 230 m, duration 790 s, travelled distance 4300 m) by determining the aerial extent of the dust devil's interaction with the surface and multiplying that by published dust devil flux and frequency measurements (Table 8.3).

The area from which dust is lifted is calculated first as the dust devil area with  $\pi r^2$  ( $4.2 \times 10^4 \text{ m}^2$ ), and secondly as the area of the travelled distance, diameter\*distance ( $9.9 \times 10^5 \text{ m}^2$ ). Different dust fluxes were derived from observations by SPIRIT (*Greeley et al.* [2006]:  $2 \times 10^{-5} \text{ kg/m}^2/\text{s}$ ), MARS PATHFINDER (*Metzger et al.* [1999]:  $5 \times 10^{-4} \text{ kg/m}^2/\text{s}$ ) and MOC (*Cantor*

Source	Dust Flux (kg/m <sup>2</sup> /s)	Area (m <sup>2</sup> )	Number dust devils (dd(t)/km <sup>2</sup> /a)	Dust Lifting (kg/m <sup>2</sup> /a)
Spirit (Greeley et al., 2006)	$2 \times 10^{-5}$	$4.2 \times 10^4$	0.060	$3.98 \times 10^{-5}$
			0.600	$3.98 \times 10^{-4}$
			0.810	$5.38 \times 10^{-4}$
			0.470	$3.12 \times 10^{-4}$
			0.344	$2.28 \times 10^{-4}$
		$9.9 \times 10^5$	0.060	$9.39 \times 10^{-4}$
			0.600	$9.39 \times 10^{-3}$
			0.810	$1.27 \times 10^{-2}$
			0.470	$7.35 \times 10^{-3}$
			0.344	$5.38 \times 10^{-3}$
Mars Pathfinder (Metzger et al., 1999)	$5 \times 10^{-4}$	$4.2 \times 10^4$	0.060	$9.95 \times 10^{-4}$
			0.600	$9.95 \times 10^{-3}$
			0.810	$1.34 \times 10^{-2}$
			0.470	$7.80 \times 10^{-3}$
			0.344	$5.71 \times 10^{-3}$
		$9.9 \times 10^5$	0.060	$2.35 \times 10^{-2}$
			0.600	$2.35 \times 10^{-1}$
			0.810	$3.17 \times 10^{-1}$
			0.470	$1.84 \times 10^{-1}$
			0.344	$1.35 \times 10^{-1}$
MOC (Cantor et al., 2006)	$1 \times 10^{-9}$	$4.2 \times 10^4$	0.060	$1.99 \times 10^{-9}$
			0.600	$1.99 \times 10^{-8}$
			0.810	$2.69 \times 10^{-8}$
			0.470	$1.56 \times 10^{-8}$
			0.344	$1.14 \times 10^{-8}$
		$9.9 \times 10^5$	0.060	$4.69 \times 10^{-8}$
			0.600	$4.69 \times 10^{-7}$
			0.810	$6.34 \times 10^{-7}$
			0.470	$3.68 \times 10^{-7}$
			0.344	$2.69 \times 10^{-7}$
Laboratory (Neakrase et al., 2006)	$1 \times 10^{-3}$	$4.2 \times 10^4$	0.060	$1.99 \times 10^{-3}$
			0.600	$1.99 \times 10^{-2}$
			0.810	$2.69 \times 10^{-2}$
			0.470	$1.56 \times 10^{-2}$
			0.344	$1.14 \times 10^{-2}$
		$9.9 \times 10^5$	0.060	$4.69 \times 10^{-2}$
			0.600	$4.69 \times 10^{-1}$
			0.810	$6.34 \times 10^{-1}$
			0.470	$3.68 \times 10^{-1}$
			0.344	$2.69 \times 10^{-1}$

**Table 8.3:** Estimations of dust lifting rates. Mean dust devil duration is 790 s. ‘dd’ stands for dust devils, ‘ddt’ stands for dust devil tracks. More details in the text.

*et al.* [2006]:  $1 \times 10^{-9}$  kg/m<sup>2</sup>/s), and from laboratory work (*Neakrase et al.* [2006]:  $1 \times 10^{-3}$  kg/m<sup>2</sup>/s). The results of *Whelley and Greeley* [2006] (0.06 ddt/km<sup>2</sup>/a northern hemisphere, 0.6 ddt/km<sup>2</sup>/a southern hemisphere), *Balme et al.* [2003b] (0.81 ddt/km<sup>2</sup>/a Argyre Planitia, 0.47 ddt/km<sup>2</sup>/a Hellas Basin) and *Cantor et al.* [2006] (0.344 dd/km<sup>2</sup>/a estimated from Ama-

zonis Planitia, Figure 16 in *Cantor et al.* [2006]) were used for the frequency of dust devils (Table 8.3; dd: dust devils; ddt: dust devil tracks).

The computed dust lifting values range between  $1.99 \times 10^{-9}$  and  $6.34 \times 10^{-1}$  kg/m<sup>2</sup>/a. The lowest values are obtained when using the very low dust lifting rate provided by *Cantor et al.* [2006]. These results are at least two orders of magnitude smaller than the results calculated with the other dust lifting rates. *Cantor et al.* [2006] provide the largest dataset with four Mars years of data and a somewhat statistically significant dust devil distribution. The dust devil frequency of 0.344 dd/km<sup>2</sup>/a, however, is only an estimation of the Amazonis Planitia region, displayed in Figure 16 in *Cantor et al.* [2006]. Since most dust devils have been seen in this area, the frequency provides an upper limit, but is less than most of the frequency values of regions of the other publications. Results at the upper limit of dust lifting rates between  $1.99 \times 10^{-3}$  and  $6.34 \times 10^{-1}$  kg/m<sup>2</sup>/a are obtained when using the laboratory dust flux of  $1 \times 10^{-3}$  kg/m<sup>2</sup>/s. They are, however, in the range of the calculations using the dust flux from the MARS PATHFINDER site. Combining the dust flux derived from SPIRIT data with the different area calculations and number of dust devils, the dust lifting ranges between  $3.98 \times 10^{-5}$  to  $1.27 \times 10^{-2}$  kg/m<sup>2</sup>/a taking only the larger dust devils into account.

The frequencies of dust devils are obtained from analysing different regions and the dust lifting rates are therefore only significant for the respective region and for the used typical dust devil diameter and the travelled distance. Since the regions are known to show a higher dust devil activity, the dust lifting rates may provide an upper limit compared to other regions on Mars. The more frequent but smaller dust devils are not included, it is also no global estimation for Mars. Including these facts the amount of lifted dust would rise again.

A preference can be given to the dust lifting rates obtained with the dust fluxes derived from SPIRIT and MARS PATHFINDER data because these values can be regarded as field measurements. The travelled distance as the interaction area is more reliable than the dust devil area alone because dust devils are naturally always moving. The dust devil frequencies are obtained investigating certain regions, but the values of *Whelley and Greeley* [2006] are averaged from several regions for each hemisphere and seem to provide a more secure frequency. The preferred values are  $9.39 \times 10^{-4}$  (northern hemisphere) and  $9.39 \times 10^{-3}$  kg/m<sup>2</sup>/a (southern hemisphere), and  $2.35 \times 10^{-2}$  (northern hemisphere) and  $2.35 \times 10^{-1}$  kg/m<sup>2</sup>/a (southern hemisphere) for SPIRIT and MARS PATHFINDER dust fluxes, respectively (Table 8.3).

Obtained dust lifting values between  $1.99 \times 10^{-9}$  and  $6.34 \times 10^{-1}$  kg/m<sup>2</sup>/a are based on parameters of a typical dust devil seen by HRSC. These results suggest that large dust devils alone can contribute significantly to the atmospheric haze and provide their contribution to the global dust settling rate of  $2 \times 10^{-2}$  kg/m<sup>2</sup>/a [*Pollack et al.*, 1979]. Judging from the capability of dust devils to lift and move dust to a large extent, dust devils are definitely responsible for local redistributions of dust and sand, depending on their forward speed, direction of movement and lifetime. The Hadley circulation which is stronger and wider during southern summer than northern summer enforces dust devil activity where the ascending branch is located. This suggests a significant local dust transport from the 50° to 60°S latitude range where most dust devils have been seen on the southern hemisphere to westward directions as it is shown by General Circulation Models for this latitude range in southern summer. The same circumstances are expected to exist on the northern hemisphere in alleviated form.

## 8.6 Dust Storms and Dust Devils

Two dust storms have been seen by HRSC in two orbits, both covering Syria Planum and only 7.4 Mars days apart. The observation in orbit 2054 shows the larger storm, with a size of approximately 100 km by at least 60 km. The dust storm dimensions cover in fact the total image width (Figure 8.8a). The dust storm moved southwards. The onset in the north was identified by smaller dust swirls that are arranged like cloud streets. These smaller swirls spread, become larger in size and merge into a dust storm. The most surprising aspect is in front of the storm front, where five dust devils can be seen that move quite fast in the same direction as the storm at 23 m/s on average. The largest dust devil seen in all HRSC images so far (diameter of  $\sim 1650$  m; height of  $\sim 4440$  m) occurs in this storm and moves at about 30 m/s on average. It is difficult to determine the base of the dust devil because of its size and the large bright vortex, although the shadow was used where it intersects with the vortex [Stanzel *et al.*, 2006]. This may explain the difference between the two measured speeds of 43.9 m/s (S1-ND) and 16.7 m/s (ND-S2) for this dust devil (Table D.1). The computed speeds for the other dust devils are more consistent.

The smaller dust storm observed by HRSC in orbit 2032 (Figure 8.8b) is about 7 km by 7 km in dimension, and appears rather like a large dust cloud than a real dust storm. The storm cloud and the two dust devils also seen in this image are separated by 62 km, but all objects appear to be moving in the same direction. Both dust devils are quite small (diameters of 80 and 138 m). The smaller one of the two is only 109 m high, whereas the larger one has a height of about 2 km. The shadow shows a long slender dust column. Computed speeds are 17 and 24 m/s for the smaller and larger dust devil, respectively. Velocity measurements for the dust storms could not be done because there are no specific surface point that can be tracked in the three stereo images.

We checked if the images before and after the orbits 2032 and 2054 also show dust storms or dust devils. Only the image from orbit 2021, 3.7 sols before orbit 2032, contains another small dust storm but no dust devils (Figure 8.8c). That storm is approximately 8 km by 12 km in size. Cantor *et al.* [2001] defined dust storms as ‘local’ of size greater than  $100 \text{ km}^2$ , and as ‘regional’ of size greater than  $1.6 \times 10^6 \text{ km}^2$ . From this definition only the dust storm in orbit 2054 can be described as local; the other two storms are at the limit of the definition or even below ( $< 100 \text{ km}^2$ ). It is likely that Cantor *et al.* [2001] were not able to detect such small dust storms because their daily global maps of the Martian surface have a resolution of 7.5 km/pixel. However, they were able to monitor some of the local dust storms with high temporal resolution [Cantor and Malin, 2003]. These results show that dust storms expand rapidly and may cover a large area in a few hours. Using the HRSC stereo channels (S1, ND and S2) provides additional observation time to observe storm changes at short temporal resolution. The time between two image acquisitions for the orbits 2032/2054 and orbit 2021 was between 25 and 40 s respectively, not enough to see any important changes in evolution except the forward motion of the dust storms.

Global dust events are composed of a number of local and regional storms [Cantor and Malin, 2003]. So it cannot be excluded that the smaller dust storms observed some days before the larger dust storm in orbit 2054 have contributed to its onset or size. Especially, they appear

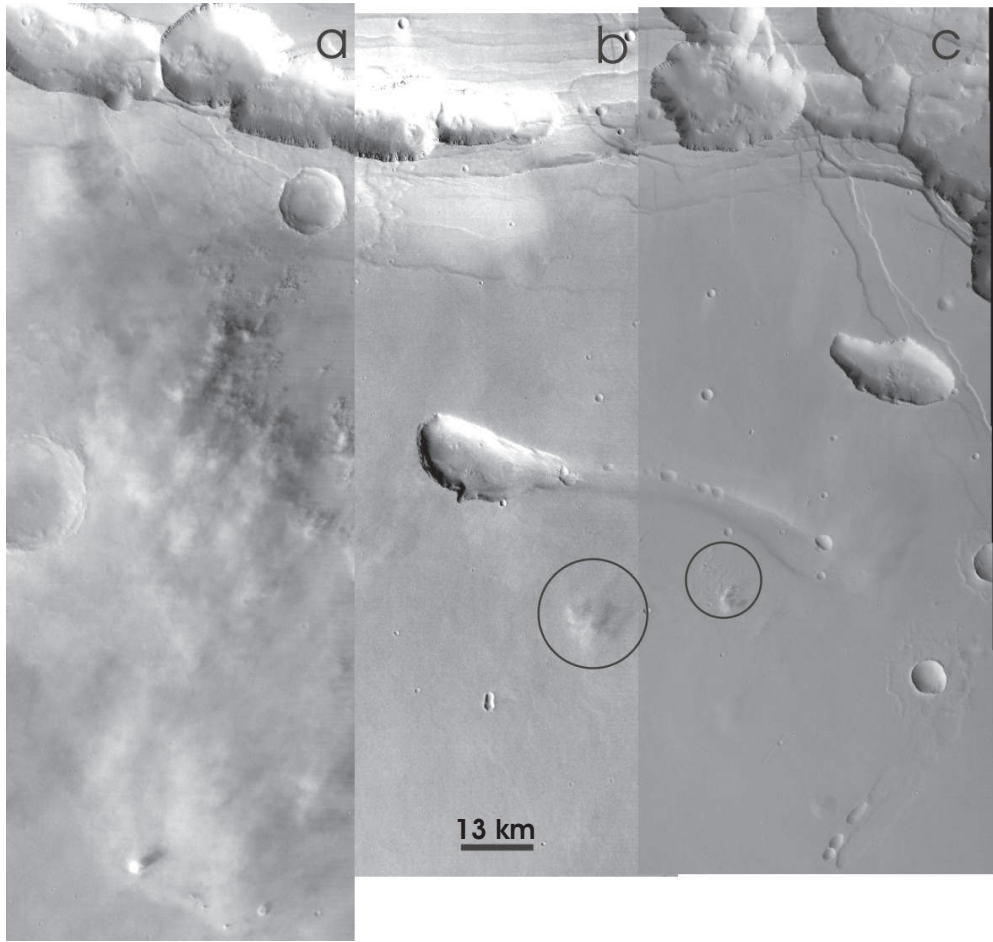


**Figure 8.8:** HRSC ND image mosaic covering parts of Syria Planum and containing dust storms. Small dust storms are encircled. North is to the top. a) Orbit 2054 taken on August 20, 2005, local time was 1513 hours,  $L_S = 273^\circ$ . At the bottom five dust devils are seen (see Figure 7.19, page 77). b) Orbit 2032 taken on August 14, 2005, local time was 1530 hours,  $L_S = 269^\circ$ . c) Orbit 2021 taken on August 11, 2005, local time was 1540 hours,  $L_S = 267^\circ$ .

at the same latitude but slightly shifted in longitude (Figure 8.8).

Although there is an annual dust storm cycle, *Cantor and Malin* [2003] note further that dust storms occur almost daily. Dust storms develop in specific regions during certain seasons. The solar longitude for the three HRSC orbits ranges from  $L_S = 267^\circ$  to  $273^\circ$  (close to Mars perihelion), which represents a period where it is very likely to detect dust storms in the southern hemisphere [*Greeley et al.*, 1992; *Barnes*, 1999]. Syria Planum is also a region well known for dust storms and dust devils [*Barnes*, 1999; *Cantor and Edgett*, 2002]. It is assumed and predicted [*Rennó et al.*, 1998; 2000; *Cantor and Malin*, 2003] that dust devils and dust storms have a higher probability to occur where sloping terrains together with large thermal gradients are located. The temperature gradients generate surface winds which may be responsible for dust lifting.

Particles of about  $100 \mu\text{m}$  size are most easily moved by a minimum wind speed of approximately  $40 \text{ m/s}$  [*Greeley et al.*, 1981]. Smaller particles of  $1 \mu\text{m}$  size seem to be most frequently transported into the atmosphere contributing to atmospheric dust loading. They require much higher wind speeds or alternative methods for lifting small particles. These

methods can include saltation cascading, outgassing volatiles, breaking down of larger particles into smaller ones by collision, or lifting by dust devils [Greeley *et al.*, 1981; 1992]. The pressure difference in a dust devil is a very efficient way to lift any kind of particles independently of the size or density. Therefore it was assumed in the past that dust devils are an important mechanism to initiate threshold and that they can trigger dust storms by injecting easily dust and sand particles into the atmosphere.

After a two Mars years survey of MOC images *Cantor and Edgett* [2002] stated that dust devils do not ‘cause, lead to, or have a systematic relationship with dust storms’. This is confirmed by the latest study covering now four Martian years analysing all images with respect to dust devils [Cantor *et al.*, 2006]. Dust devils are, however, observed near local storms as in the two HRSC orbits (Figure 8.8, a+b) presented here. *Cantor et al.* [2006] have seen several dust devils at the fronts of dust storms like terrestrial vortices accompanying storm fronts. The dust storm could therefore be responsible for the initiation of nearby dust devils. This explains why dust devils observed near storms have high forward speeds. The conclusion is drawn that similar conditions are responsible for the development of storms and dust devils, but they do not necessarily trigger each other. Required conditions seem to be strong winds caused by temperature gradients, sloping terrains and of course an unstable atmospheric stratification or convection due to insolation. The most supporting season to initiate both, storms and dust devils, is summer on the respective hemisphere. It is not clear, however, if these dust devils (orbit 2054) have developed before, after or simultaneously with the dust storm. One gets the impression from Figure 8.8a that the storm catches up with the dust devils in front due to its assumed higher traverse velocity.

## 8.7 Comparison with SPIRIT Dust Devils

During the first Martian year of operations, observations from the Mars Exploration Rover SPIRIT resulted in a comprehensive study of dust devil activity from the surface of Mars [Greeley *et al.*, 2006]. 533 active dust devils were observed between March 10, 2005 and December 12, 2005. On Mars this corresponds to  $L_s = 173.2^\circ$  to  $339.5^\circ$ , or southern hemisphere spring and summer. The dust devils ranged in diameter from 2 to 276 m, with most between 10 and 20 m. All occurred between 0930 and 1630 hours local time and were most frequent around 1300 hours. Dust devil height was difficult to determine due to limited viewing geometry and imaging. As a result the top of most images truncated the dust devils (Figure 8.9). Dust devils that were observed in full ranged from 9 to 361 m, while the tallest dust devil that was truncated by the top of the frame was at least 848 m high. Horizontal speed (or the traverse velocity) ranged from  $<1$  to 21 m/s while vertical speeds ranged from 0.2 to 8.8 m/s. *Greeley et al.* [2006] conclude that in the inferred dust devil zone in Gusev crater, there are 50 active dust devils/km<sup>2</sup>/sol resulting in  $\sim 19$  kg/km<sup>2</sup>/sol of material injected into the atmosphere from dust devils or one tenth of the estimate for dust storm loading by *Cantor et al.* [2001]. The lifetimes estimated for the dust devils in Gusev, ranged from 0.7 to 11.5 min for dust devils seen in full cycle. Other estimates from 0.3 to 32.3 min represent minimum lifetimes of dust devils already existing at the start or still active at the end of image sequences. The mean duration was 2.8 min.

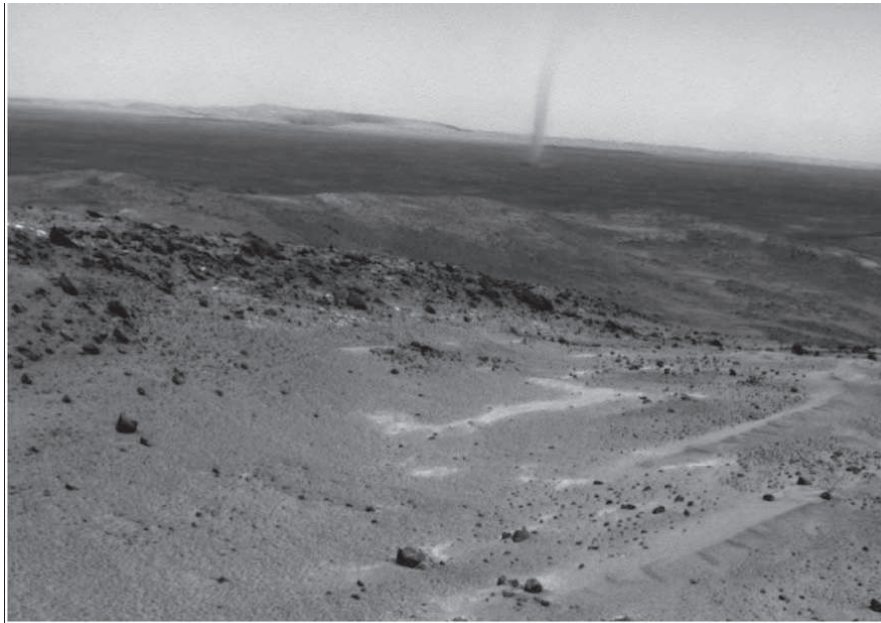


**Figure 8.9:** Dust devil on the floor of Gusev crater, imaged on sol 616 by the Spirit Navcam (image 2N181053592EFFAEOTP0607L0M1) from the Columbia Hills. This dust devil is about 1 km from the rover and is estimated to be at least 95 m high. The image was enhanced to increase contrast. Adapted from Greeley *et al.* [2006].

When HRSC and SPIRIT dust devil observations are compared to each other, it is most obvious that both observation methods complement each other (Table 8.4). The smallest dust devils observed in HRSC images have diameters of  $\sim 50$  m, which are four image pixels at the highest resolution of 12.5 m/pixel in the ND channel. This is at the edge of resolution and the calculated error is even higher than this value. Most dust devils seen by SPIRIT were 10 to 20 m in diameter, or roughly one third of the smallest HRSC diameters. The largest diameter from SPIRIT observations was 276 m which overlaps with most of the HRSC dust devils ( $< 400$  m in diameter).

Assumptions about dust devil frequency made by several authors who examined images from different Mars missions must be reassessed because the smaller dust devils are typically not seen from orbit. If the lifetime of dust devils is on the order of several minutes, it is a lucky circumstance to detect them at the right time by an orbiter camera. The difference in the total number of dust devils observed by HRSC and SPIRIT results from these considerations. SPIRIT has seen many more but much smaller dust devils.

These smaller dust devils are able to inject  $\sim 1.3 \times 10^{-2}$  kg/m<sup>2</sup>/a into the atmosphere according to the calculations of Greeley *et al.* [2006]. This corresponds almost to the global dust settling rate of  $2 \times 10^{-2}$  kg/m<sup>2</sup>/a obtained by Pollack *et al.* [1979] and would suggest that small dust devils alone are responsible for the bigger part of the airborne dust. However, the dust devils have been seen in this high quantity in the spring and summer season which favour dust devil formation and represent only the conditions at the Gusev crater landing site. The dust devil survey was maybe conducted when exceptionally good conditions for dust devil development prevailed. A dust devil monitoring in the next spring and summer season would be very helpful to evaluate the obtained dust devil frequency and dust lifting rates.

Our calculations of dust lifting rates using the typical HRSC dust devil resulted in the pre-

Dust Devil Feature	HRSC (205 dust devils)	Spirit (Gusev crater, 533 dust devils)
Location (Hemisphere)	12°-44°N; mostly 10°-20°N 1°-62°S; mostly 50°-60°S	14°S
Local Time/ Solar Longitude	1110-1630 hours 57°-337° L <sub>s</sub> (N) 77°-343° L <sub>s</sub> (S)	0930-1630 hours 173°-340° L <sub>s</sub> (S)
Height	75-4440 m mostly <1000 m	10-360 m (full range) up to 850 m (truncated)
Diameter	45-1650 m mostly <400 m	2-280 m mostly 10-20 m
Traverse speed	1-59 m/s mostly <15 m/s	<1-21 m/s
Lifetime	3.7-32.5 min (12 DD minimum lifetime) mean 13 min	0.7-11.5 min (59 DD full cycle) 0.3-32.3 min (290 DD minimum lifetime); mean 2.8 min
Dust Lifting Rate	$9.39 \times 10^{-4}$ - $2.35 \times 10^{-1}$ kg/m <sup>2</sup> /a (preferred values)	$1.3 \times 10^{-2}$ kg/m <sup>2</sup> /a

**Table 8.4:** Comparison between HRSC and SPIRIT dust devil observations. DD stands for dust devils.

ferred values of  $9.39 \times 10^{-4}$  to  $2.35 \times 10^{-1}$  kg/m<sup>2</sup>/a using SPIRIT and MARS PATHFINDER dust fluxes along with the dust devil frequencies of *Whelley and Greeley* [2006]. This overlaps with and exceeds the results of the SPIRIT calculations because the HRSC dust devil is at the upper limit of the dimensions of the dust devils seen with the rover and has a much longer lifetime. Combining these results leads to the conclusion that dust devils beside dust storms are the main causers for the airborne dust.

The time of occurrence using all HRSC dust devils is in good agreement with SPIRIT dust devils as well. That dust devil formation on Mars is coupled with the daily insolation and therefore the stratification of the atmosphere as it is on Earth, is now clearly proven using the HRSC and SPIRIT results. SPIRIT gave the details from one location whereas HRSC analyses obtained the same results from different regions. MARS GLOBAL SURVEYOR which provided the largest database of dust devil images so far has a sun-synchronous orbit. Dust devils can be only imaged between 1400-1500 hours.

Twelve dust devils from HRSC images were used to calculate their lifetimes for comparison with those derived from Gusev dust devils (Table 8.4). The range of lifetimes agreed very well with each other when the minimum lifetimes are considered. Only 59 dust devils were observed in full lifetime by SPIRIT with values between 0.7 and 11.5 min which overlaps with the minimum lifetimes from HRSC as well. The mean lifetime of SPIRIT dust devils, however, is less than one fourth of those observed with HRSC. This corresponds to the sizes of the dust devils. The larger the dust devils the longer is the duration (see Section 8.4). This is another reason why it is difficult to image such small dust devils with an orbiter when they are not as long-lasting as their larger counterparts.

Traverse speeds of <1 to 21 m/s obtained from SPIRIT dust devils confirm our results (mostly <15 m/s) by analysing HRSC stereo images and the movement of the dust devils. Most of the

time the forward speed is a few meters per second, but values up to 20 m/s are not extremely rare and even higher speeds can be seen if the dust devils are propelled for instance by a dust storm.

In summary, the observations of dust devils from orbit complement those seen from the surface. SPIRIT images smaller dust devils and provides insight into details such as formation, frequency, vertical velocity and dust flux. Statistics can be assembled for the daily and seasonal distribution of dust devils at the landing site. Directions of movement can be estimated to derive prevailing wind directions. The tracks of dust devils can be studied in order to examine the particles which have been removed and injected into the atmosphere.

Lander observations, however, are restricted to a single location and generally one viewing direction per sol [Greeley *et al.*, 2006]. HRSC provides after almost four years a nearly global coverage of the Martian surface. From its field of view, more and larger dust devils can be detected simultaneously in HRSC data. A reliable size of larger dust devils can only be retrieved by orbiter images. This includes the upper size limits of dust devils. Different regions can be compared with respect to the dust devil activity and the spatial distribution can be confirmed. The pattern recognition and classification software developed in this study enables now a comprehensive investigation of all images.

## 8.8 Joint MEX-MER Observations

In October 2005 it was first tried to image dust devils simultaneously with the orbiter MARS EXPRESS (MEX) and the Mars Exploration Rover (MER) SPIRIT. Orbit 2249 was imaged with the standard configuration, all nine channels working and with 12.5 and 25 m/pixel resolution for the nadir and the stereo channels, respectively. This was changed for orbit 2271 where no colour channels were used and the ND, S1 and S2 images had in addition the same resolution of 12.5 m/pixel for a better comparison. The two orbits were taken only 3 Mars days apart from each other at a local time of 1215 and 1230 hours in southern summer. Although the conditions are favourable for dust devil formation no active dust devil was seen in the HRSC images. During the first overpass (orbit 2249) SPIRIT was able to image some dust devils [Whelley, 2007], but they are not in the field of view of the HRSC images. Unfortunately SPIRIT was not able to take a dust devil image sequence during the second overflight [Whelley, 2007].

On April 3, 2007, the second attempt was conducted to image dust devils with the orbiter and the lander simultaneously. The orbit 4165 was a full-resolution stereo observation (ND, S1 and S2 at 12.5 m/pixel) and additionally an SRC strip was done over the Columbia Hills, where SPIRIT is still continuing to make studies. No dust devils were observed by SPIRIT nor HRSC. Although the SRC frames look quite good, there is also no evidence of active dust devils [Williams, 2007]. The conclusion was that because the observations occurred in the late afternoon ( $\sim$ 1630 hours local time), the tendency for dust devils to form at this time is much reduced compared to early afternoon. The season was southern spring.

What can be seen from the HRSC images is that there are changes in pre-existing dust devil tracks [Williams, 2007]. These features are useful for further understanding the time variation

of dust devil activity in Gusev crater.

These joint observations will likely be continued as long as both spacecraft are working.



---

## DISCUSSION AND OUTLOOK

---

A pattern recognition and classification software for Martian dust devils was developed to detect dust devils automatically in surface images taken by spacecraft orbiting Mars. The software is able to process image data from three different Mars missions, VIKING, MARS EXPRESS and MARS GLOBAL SURVEYOR. It can be applied to images of future missions without circumstance.

VIKING images containing dust devils were used as the database to extract features, which describe dust devils as uniquely as possible. Since dust devils are represented as bright spots (dust column reflecting the sunlight) and a corresponding shadow, a brightness maxima search was conducted in the images. Best-fit ellipses were adjusted to the resulting clusters. The features which describe the bright spot of a dust devil, are the eccentricity  $\epsilon$ , the quality parameter  $q$  (ratio of the cluster area within the ellipse to the area of the ellipse) and the size  $g$  of a bright cluster.

It is searched for a potential shadow in the vicinity of analysed bright spots filtering this time for brightness minima. The parameters which describe a dust devil shadow, are the size  $g$  and the barycentre coordinates  $x_s$  and  $y_s$  of the dark clusters. If the shadow coordinates are selected as parameters with respect to the dust column of the dust devils, knowledge must exist about the illumination conditions at the specific site. For this reason the required illumination angles were computed for the period when and where an image was taken. A total of eight shadow classifiers were designed covering different regions around a bright cluster.

After a comprehensive test phase with the VIKING images as training data, a multi-layer perceptron was chosen as classifier. A perceptron is a neural network classifier, which provides good adaptivity and generalisation with respect to new unknown features. The classification was separated for the bright spots and the shadows of dust devils to keep the dimensions of the feature vector (containing the extracted parameters) low. A classification rate of 51.08% for dust devils was achieved in VIKING images. Considering those dust devils not detectable

for various reasons, 85.15% of the dust devils were correctly classified. Roughly three of four objects (77.21%) positively assessed by the software to be dust devils, were indeed dust devils.

The verification of the performance of the software for HRSC images was done using 13 HRSC images with dust devils. A classification rate of 22.9% for dust devils was achieved. The high resolution and the resulting more detailed structures of the dust devils complicate correct classification. The size ranges now from still too small dust devils to larger ones which are not well represented anymore in the chosen standard configuration of the software (resolution of 25 m/pixel for HRSC images). The implemented checking of the angle  $\phi$  (orientation of a shadow cluster) overruled the decision of the classifier in some dust devil cases, but improved otherwise the total detection rate a lot by discarding many other features. The fraction of dust devils from total objects classified as dust devils is 16.9% or every sixth classified object is indeed a dust devil. Given the particularities of the HRSC images which complicate the recognition and classification process, and the multiple forms of appearances of dust devils, these results are very satisfying and solve the problem to filter the standard dust devil from the background of the image. The search for dust devils was then extended to several selected regions on Mars, analysing all available HRSC images for the specific areas.

The pattern recognition and classification software was applied to a selection of MARS GLOBAL SURVEYOR MOC images and the results were very good. 73.3% and 97.2% of the positively assessed objects for the narrow and wide angle images, respectively, are indeed dust devils. Similar to HRSC results 25.6% of the dust devils seen in narrow angle images are correctly classified. The high number of dust devils in wide angle images cannot be verified, neither visually nor by the pattern recognition software. The quality of these images constrains the ability of the software.

It was demonstrated that the typical dust devil is detected by the pattern recognition software and correctly classified, independently from which Mars mission the images come from. HRSC provides the most detailed images covering simultaneously a large area which stands out from the other mission images. Therefore the number of positive classifications was increased.

One idea to decrease the higher detection rate was to compare the filtered data from the nadir and the stereo channels. In principle, the filtered data should contain the same clusters with the same computed parameters since the adjusted resolution of the nadir image is the same as for the stereo channels and the images cover almost the same area. Only the clusters representing dust devils should change their appearances and coordinates because of the motion. The classification results overview of the single image cut-outs showed already discrepancies in the number of objects which were classified as possible dust devils. Analysing image cut-outs in detail which included dust devils, revealed different filtered clusters in large part although the cut-outs are almost identical. Prominent clusters like dust devils had slightly different values regarding the parameters size and eccentricity, but also the coordinates did not change as much as expected. Comparing the clusters derived from nadir and stereo images revealed therefore no clear changes which can be related to dust devils. This is probably due to the varying illumination conditions which change during the three image acquisitions and maybe due to the different imaging geometry as well.

Apart from our work, it is only known from one further study dealing with the automated detection of dust devils in MARS GLOBAL SURVEYOR MOC images [Gibbons *et al.*, 2005]. They search as well for bright clouds accompanied by a shadow. Many spurious features are detected when they tried to find all dust devils. They note that the software is adjusted so that only candidates which match the traits of dust devils at the best are selected. Crater rims and hills, however, are very often mistaken for dust devils as it was shown in our classification results of HRSC images. Gibbons *et al.* [2005] extract brightness profiles of the candidates and fit polynomial functions to them. The derived coefficients of the polynomials are then presented to a simple neural network which is trained to distinguish between dust devils and crater rims. According to Gibbons *et al.* [2005] this works quite well but it is not known how many crater rims are exactly discarded and how many dust devils they detect at all by this approach. However, extracting brightness profiles and analysing the adjusted polynomial fits could be another post-processing step extending our pattern recognition and classification software, leading to a reduced list of positively classified objects.

Gibbons *et al.* [2005] note that hills can be eliminated by analysing images of the same area taken at different times. This is always done from our site with ambiguous objects comparing the nadir and stereo channels. In contrast to the software of Gibbons *et al.* [2005] our software can handle Martian images from three different missions, and it can be adjusted to other future mission data as well. This is especially valuable, since MARS GLOBAL SURVEYOR stopped working and no new MOC images will be delivered any more. In addition, Cantor *et al.* [2006] already provided a comprehensive dust devil search in MOC images.

Another possible improvement of the results could be achieved if the filtered and computed bright spot and shadow parameters are evaluated together as a six-dimensional feature vector. If for example the bright spot is rejected because it is regarded as too small, an accompanying perfect shadow could influence the result in such a way that the object is classified as dust devil.

The database of HRSC dust devils is growing. When a sufficient number of dust devils is detected in the images and analysed/filtered by the software, this could provide a new training database for a classifier. This classifier could be more sensitive to the specific appearance of dust devils in HRSC images, such as accepting a larger size of dust devils. Since the appearance is more versatile, presenting all dust devils to the classifier (smaller and larger ones, with well-shaped and tilted columns, etc.), could complicate the training achieving no satisfying classification results. One possibility could be to create several classifiers which are for example only responsible to classify smaller or larger dust devils, respectively.

Dust devils in HRSC images were analysed with respect to their size (diameter and height), temporal and spatial distribution, lifetime, speeds and dust lifting rate. The computation of the forward speed was possible for the first time using the stereo channels of HRSC. Most surprising was the fact that dust devils move at high and sometimes very high speeds as well. The formation is not suppressed by high wind speeds. The traverse velocity derived from the motion of dust devils can be regarded as an indirect measurement of the wind speed near the surface and therefore it is now proven that dust devils indeed move with the ambient wind as it was formerly assumed. In addition, short-time changes in the structure of dust devils, as well as the formation and collapse could be followed.

The lifetimes could be estimated for the first time as well. This revealed minimum lifetimes

from a few minutes up to 30 minutes. It is likely that small-size dust devils have only a lifetime of a few minutes whereas larger dust devils will definitely exceed a lifetime of a half-hour duration. These results are important to estimate the dust lifting rate entrained by dust devils into the atmosphere.

Our calculations of dust which is transported by the typical HRSC dust devil suggest that larger dust devils alone make a significant contribution to the airborne dust. Taken the results of SPIRIT analyses into account it can be concluded that dust devils are in addition to dust storms the main causers of dust entrainment into the atmosphere of Mars. These results show that the amount of lifted dust is in the range of the global dust settling rate per year.

The time of day when dust devils occur is from forenoon to afternoon and coincides with SPIRIT results. It follows strictly the daily insolation. However, dust devils occur as well in local autumn and winter beside the dust devil 'season' in spring and summer.

Dust devils evolve wherever the atmospheric conditions are suitable and are not limited to certain latitudes or elevations. The thin atmosphere of Mars does not prevent dust devil formation even in the calderas of high volcanoes. There seems to be a preference for the latitude range between  $50^{\circ}$  and  $60^{\circ}$ S. The southern hemisphere is tilted to the Sun when Mars is closest to it. The higher insolation strengthens the conditions which are necessary for dust devil development. In contrast to the high occurrence in the southern hemisphere, the high frequency in Amazonis Planitia on the northern hemisphere could not be verified with HRSC data. The target area Chryse Planitia revealed a high dust devil activity in the southern parts, including Simud Vallis and Xanthe Terra crossing the equator. The valley system and the corresponding flow field could play a role in dust devil formation.

The average diameter is 230 m and the average height 660 m which corresponds to most of the terrestrial dust devils. Dust devils with  $\sim 50$  m of diameter were now possible to identify due to the high resolution images.

Applying the pattern recognition and classification software developed in this study to all HRSC images covering certain regions will help to constrain the distribution of dust devils, which is useful for validating models of dust devils themselves or General Circulation Models (GCMs) where the dust transport plays an important role. It is also possible to determine wind speeds and wind directions from the dust devil movement. There are still open questions regarding the dust and wind distributions on Mars which are important factors for the climate on Mars.

The potential of dust devils as hazards to robotic or future human exploration has not yet been investigated. Regions with a high occurrence could be excluded as landing sites. On the other hand more in situ measurements in dust devil-rich regions would help to further quantify the electrical and dust hazard potential and confirm the dust devil characteristics like size, height, speed, pressure and temperature perturbations. The developed software and the investigations included in this study provide the basis for time-saving new detections and further detailed studies of dust devils.

## IMAGE IDENTIFIERS

---

### A.1 VIKING

The image identifier for a VIKING Orbiter image is a six-character string, e.g. '034b01'. Throughout this work, images are identified with an 'f' in front of each VIKING filename. This was automatically added after decompressing the images. The first three characters represent the orbit number. The fourth character is either an 'a' for VIKING Orbiter 1, a 'b' for VIKING Orbiter 2, or an 's' for the VIKING Orbiter 1 Survey Mission. The letters 'c' and 'd' are used for images acquired by VIKING Orbiter 1 and 2, respectively, before orbit insertion. The letter 'x' is used for VIKING Orbiter 1 images when more than 100 images were taken in one orbit. The last two characters represent the sequence number of the image within one orbit.

### A.2 MARS GLOBAL SURVEYOR

The filename consists of an eight-character string, e.g. 'e0302304'. The first character identifies a subphase of the MARS GLOBAL SURVEYOR mission. 'm' stands for the first full Mars year of Mapping Observations, 'e' comes from the second full Mars year (Extended Mission), 'r' from the third Mars year (Relay Subphase), and 's' from the fourth (Support Subphase). The second and third character represent the month of a mission phase, and the last five characters build the sequence number of an image acquired that month.

It is not seen by the image filename if the image was acquired with the narrow or the wide angle camera, or if the red or blue filter was used with the wide angle camera. These informations are only available in the image label.

### A.3 MARS EXPRESS

A 17-character string identifies HRSC images, e.g. 'h2133\_0000.nd3.04'. The first character is the *camera\_id* 'h'. The next four characters represent the orbit number, whereas the four characters behind the underscore identify the image sequence number in one orbit. 'nd' is the *detector\_id* for the nadir channel. Other possibilities are 's1' (stereo 1), 's2' (stereo 2), 'p1' (photometric 1), 'p2' (photometric 2), re (red), ir (near-infrared), gr (green), bl (blue), and sr (SRC, the Super Resolution Channel). The figure behind the *detector\_id* states the data level. Level 2 means radiometrically corrected images, Level 3 are additionally geometrically corrected and projected to a MOLA DTM. Level 4 stands for higher science products like newly-created DTMs using only HRSC images. The last two characters represent the version number of the images.

In this work nadir, stereo 1 and 2, and SRC images were used, in Level 2 as well as in Level 3 format. Normally it is referred to the images just with the orbit number, e.g. '2133', and unless it is mentioned otherwise this refers to the nadir image, Level 3, with sequence number 0000.

The images were separated in several cut-outs before processing with the pattern recognition software. The cut-outs, e.g. 'h2133\_0000.nd3.04\_half\_y12x3.pgm', have the same name as the original image, plus '\_half' to identify that the images have only the half resolution now. The figures behind 'y' and 'x' identify the row and the column of the cut-outs, respectively. The suffix '.pgm' is added because the images are changed from the VICAR format into the pgm-format and are then processed.

---

## HOSHEN-KOPELMAN ALGORITHM

---

The input to the algorithm is the black and white image derived from filtering the original greyscale VIKING image (Figure 6.2, page 38). In the pgm-format white pixels have the value 0, black pixels the value 1. This is changed so that all former white pixels have a value of -1, and the black pixels have a value of 0, due to more comfortable computation reasons. The image is read line by line starting from the top left corner. Since the topmost image line and the first column have no neighbours which could have been previously checked, an additional line and column with value 0 are added to assure the function of the algorithm. If a site is occupied, i.e. pixel value is -1, the neighbours of the site are checked if they are also occupied and if a label is already given. The original Hoshen-Kopelman algorithm defines only the left and upper site as direct neighbours of an analysed site. This would lead to more smaller and single pixel clusters based on the black and white dust devil image since the bright spots representing the dust columns may become diffuse at the boundary. For this reason, also the upper left and upper right neighbour pixels are included in the comparison. This extends the algorithm because there are 16 possible combinations of neighbours to a occupied site.

If the occupied site has no neighbours, it gets a new number (Figure B.1). If there are neighbours the new site gets the same label as the previously detected cluster. The problem is, if two clusters merge which were first given different labels. The labels will be compared and the lower number is assigned to the new site. In a second loop through the image all sites of a cluster are corrected getting the same number. Figure B.1 shows as a result three clusters with labels 1, 3 and 7. In addition, the size of each cluster and the size distribution of clusters of one image are computed.

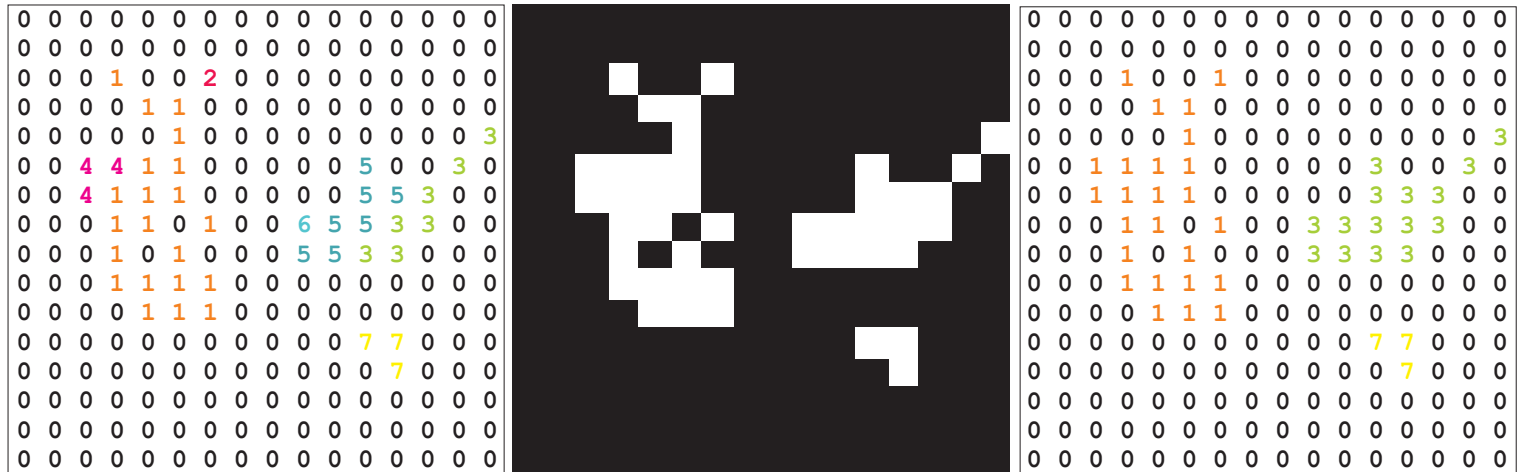


**Figure B.1:** On the left: Assigned numbers to the formerly with -1 marked pixels of a cluster. The algorithm reads line by line starting top left, increasing the number by one if a new site without neighbours (the left, upper left, upper and upper right pixel) is found. If there are two neighbours with different numbers, the lower number is assigned. In the middle: a possible cut-out of a black and white dust devil image with three clusters. On the right: The algorithm notes that sites despite their different numbers belong to one cluster and assigns the lowest number as the label for all sites of a cluster.

---

## CLASSIFICATION RESULTS

---

### **C.1 VIKING Image Analyses**

The Table C.1 shows the pattern recognition and classification results of each of the 38 VIKING images which were used as the database for training and testing the classifier. Classification was done with the later chosen classifier, the multi-layer perceptron.

<b>38 VIKING images</b>				
Image	Number dust devils	Correctly classified	Total objects (incl. dust devils)	Notes for misclassification
f034b01	26	22	23	image border, low q values
f034b02	8	7	8	too small
f034b03	4	3	4	low q value
f034b04	4	0	1	too small, all shadows detected
f034b13	1	1	2	crater
f034b15	5	4	11	crater
f035b11	3	1	1	image border, high eccentricity
f035b13	15	5	6	small dust devils, dark image
f035b14	19	10	10	small dust devils
f035b16	16	7	7	small dust devils, image border
f035b17	17	6	6	small dust devils, weak shadows
f035b18	16	8	9	small dust devils, hill
f035b19	16	8	9	image border, hill
f035b20	9	3	5	small dust devils, hills
f035b31	12	5	5	small dust devils, low q values
f035b32	13	7	7	small dust devils, all shadows detected
f035b33	1	0	1	no shadow seen, hill
f038b11	9	5	5	small dust devils, low q values
f038b12	36	14	15	small dust devils, all shadows detected
f038b13	1	1	1	
f038b14	3	1	1	small dust devil, low q value
f038b17	2	1	1	small dust devil
f038b22	8	4	4	small dust devils, no shadows
f038b23	10	6	6	small dust devils, all shadows detected
f038b25	24	15	18	small dust devils, hill, crater
f038b26	4	2	6	small dust devils, hills, craters
f038b27	15	11	13	small and one large dust devils
f040b11	4	2	4	small dust devils, low q value, craters
f119a73	2	0	0	small dust devils, image border
f119a75	3	0	0	small dust devils, all shadows detected
f439s03	1	0	0	too small
f659a06	1	0	2	low q value, hills
f670a06	2	0	6	hills
f670a08	4	2	9	craters, hills
f670a12	3	1	2	weak shadows, crater
f670a14	3	2	4	weak shadow, crater, hill
f670a15	3	0	1	weak shadows, crater
f670a21	2	2	2	

*Table C.1: Classification results of VIKING images building the database for the pattern recognition and classification software.*

## C.2 HRSC Image Analyses

The search for dust devils was started in Amazonis Planitia. Before the pattern recognition and classification software was finished, the orbits shown in Table C.2 were visually analysed. These images were chosen because of the spacious, but somewhat improper area definition of 0-30°N and 180-225°E of Amazonis Planitia. This definition was later more specified (1.2-48.4°N, 172.4-219.6°E) and the additional orbits were then analysed with the in the meantime finished pattern recognition software (Table C.3).

The Tables C.3 to C.5 display the results of each analysed image from different regions on Mars. Note that the images have been fully analysed although they may cover only a small part of the target area. Dust devils have therefore been found in neighbour regions (see Table D.1) close to the target areas as well. They appear in the tables C.3 to C.5 under the name of the target area. Not all images covering Chryse Planitia could be analysed up to July 2007.

---

### HRSC - Amazonis Planitia

---

0049, 0072, 0205, 0286, 0895, 0917, 0939, 0994, 1104, 1177\_0001,  
 1210\_0001, 1221, 1232, 1254, 1287\_0001, 1309, 1331, 1437\_0001,  
 1441, 1485\_0009, 1518\_0001, 1525\_0001, 1540\_0009, 1635, 1897,  
 1908, 1930, 1941, 1952, 1963, 1974, 1985, 1996, 2007, 2018, 2047,  
 2549\_0001, 2921, 2932, 2965, 2976, 2987, 2998, 3203, 3207

---

**Table C.2:** Visually analysed images covering Amazonis Planitia. No dust devils were found in any of these images.

<b>HRSC - Amazonis Planitia</b>				
Image	Number dust devils	Correctly classified	Total objects (incl. dust devils)	Notes
0143_0009	0	0	(443)	craters and hills
0335	0	0	4	crater rims
0987	0	0	1	crater
0998	0	0	2	crater rims
1009	0	0	3	hilly region
1258_0001	5	1	15	hills, crater rims
1313	0	0	2	crater rims
1404_0001	2	0	12	craters, rocky
1408	0	0	2	hills
1503	0	0	32	hills, crater rims, ejecta
1532	0	0	27	hills, crater rims
1562_0000	0	0	0	
1562_0008	0	0	40	rocky, craters
1580	0	0	28	hills
1591	0	0	58	ejecta
1595	0	0	3	hills, ejecta
1609_0009	0	0	61	craters
1624	0	0	46	hills, ejecta
1912	0	0	12	craters
2062	0	0	0	craters, hills
2073	0	0	10	craters, hills
2084	0	0	19	ejecta, hills
2117	0	0	42	hills
2124	0	0	22	ridges, hills
2128	0	0	72	hills, ridges
2135	0	0	5	hills
2146	0	0	10	hills
2205_0001	0	0	6	hills
2216_0001	0	0	7	hills
2238_0001	0	0	3	crater rims
2271_0000	0	0	2	crater rim, hill
2271_0009	0	0	0	
2866	0	0	1	hill
2969	0	0	7	hills
2980	0	0	1	hill
2991	0	0	3	hills
3024	0	0	6	hills
3035	0	0	1	hill
3042	1	0	8	crater rims
3046	0	0	4	hills
3086	0	0	1	hill
3119	0	0	13	craters
3185	0	0	8	hills, crater rims

**Table C.3:** Classification results of HRSC images covering Amazonis Planitia (Status of May 2007).

<b>HRSC - Syria Planum</b>				
Image	Number dust devils	Correctly classified	Total objects (incl. dust devils)	Notes
0068	1	0	(124)	hills, craters
0563	0	0	9	hills, craters
1988	0	0	21	rocky region
1999	0	0	14	crater rims, hills
2021	0	0	9	dust cloud classified
2032	2	1	14	dust storm
2054	5	1	5	dust storm
2087	0	0	12	crater rims, furrows
2109	0	0	24	hills, craters
2120	0	0	32	hills, craters
2131	0	0	19	furrows, craters
2153_0001	0	0	17	rocks, raters
2468	0	0	84	craters, crater rims
2479_0010	0	0	101	craters, coarse surface
2728_0001	0	0	0	resolution 100 m/pixel
3155	0	0	6	rocks, furrows
3221	0	0	11	craters, hills

*Table C.4: Classification results of HRSC images covering Syria Planum (Status of May 2007).*

<b>HRSC - Chryse Planitia</b>				
Image	Number dust devils	Correctly classified	Total objects (incl. dust devils)	Notes
1980	0	0	9	ridges
1991	0	0	9	ridges, hills
2002_0001	0	0	18	ridges, hills
2013_0001	0	0	12	craters, furrows
2024_0001	1	0	24	craters, rocky
2035	19	3	36	many dust devils weak
2046	11	3	7	crater rims
2057_0001	0	0	8	craters, ridges
2090	4	0	87	very hilly and rocky
2101	11	4	101	crater rims, ridges
2112	8	3	89	hills, ridges, crater rims
2123	27	9	125	hills, ridges, crater rims
2134	27	7	171	hills, ridges, crater rims
2145	4	1	226	hills, ridges, crater rims
2156	0	0	124	crater, hills, coarse surface
2244	0	0	0	
2277	0	0	8	crater rims, hills
2876	0	0	0	
2920	0	0	19	craters, hills
2942	0	0	14	craters, coarse surface
2964	0	0	13	craters, coarse surface
3059	0	0	6	craters, coarse surface
3081	0	0	1	crater
3103	0	0	35	craters, coarse surface
3114	0	0	13	craters, coarse surface
3147	0	0	2	crater rims
3202	5	1	40	border problem
3235	0	0	26	craters, coarse surface
3246	49	3	52	very small dust devils

**Table C.5:** Classification results of HRSC images covering Chryse Planitia (Status of July 2007).

---

## HRSC DUST DEVIL CHARACTERISTICS

---

The following Table D.1 shows the analysed dust devil characteristics forward speed, diameter and height. The data is chronologically presented with increasing orbit number. The diameter is measured between two points which enclose the dust devil vortex. A constant error of five image pixels ( $\sim 63$  m at a resolution of 12.5 m/pixel) is assumed for the determination of the diameter. The speed error depends on the measured distance and the time between two dust devil positions. The error of the height depends on the measured shadow length and the sun incidence angle.

The recently detected dust devils of the orbits 2123, 2134 and 2145 covering partly Chryse Planitia are not yet analysed and therefore not included in Table D.1.

Dust Devil Number	S1-ND, m/s	ND-S2, m/s	Diameter, m	Height, m
<i>Arcadia Dorsa / Arcadia Planitia, Image = h0037_0000,</i> <i>L<sub>s</sub> = 337°, LT = 14:15, Lat = 43°N, Lon = 230°E</i>				
dust devil 1	-	23.3 ± 1.3	168 ± 63	490 ± 96
dust devil 2	-	24.3 ± 1.4	265 ± 63	615 ± 98
dust devil 3	-	24.6 ± 1.3	361 ± 63	275 ± 97
<i>Icaria Planum, Image = h0068_0000,</i> <i>L<sub>s</sub> = 343°, LT = 13:25, Lat = 40°S, Lon = 255°E</i>				
dust devil 1	-	14.8 ± 3.8	159 ± 63	386 ± 234
<i>Syrtis Planum, Image = h1054_0000,</i> <i>L<sub>s</sub> = 115°, LT = 15:03, Lat = 1°S, Lon = 70°E</i>				
dust devil 1	26.8 ± 7.3	21.4 ± 7.1	313 ± 63	-
<i>Thaumasia Planum, Image = h1081_0000,</i> <i>L<sub>s</sub> = 118°, LT = 14:55, Lat = 23°S, Lon = 297°E</i>				
dust devil 1	-	20.8 ± 3.4	138 ± 63	649 ± 95
dust devil 2	22.7 ± 4.0	18.8 ± 3.4	205 ± 63	2474 ± 95
dust devil 3	20.0 ± 4.0	15.0 ± 3.3	654 ± 63	2956 ± 94
dust devil 4	21.4 ± 4.0	17.8 ± 3.3	230 ± 63	3371 ± 94
dust devil 5	16.8 ± 4.0	16.9 ± 3.3	158 ± 63	410 ± 94
<i>Amazonis Planitia, Image = h1258_0001,</i> <i>L<sub>s</sub> = 142°, LT = 12:44, Lat = 34°N, Lon = 182°E</i>				
dust devil 1	2.2 ± 6.3	6.0 ± 6.1	50 ± 63	1043 ± 444
dust devil 2	3.2 ± 6.3	1.8 ± 6.1	88 ± 63	984 ± 452
dust devil 3	1.6 ± 6.2	1.5 ± 6.0	73 ± 63	1277 ± 453
dust devil 4	5.8 ± 6.2	2.7 ± 5.9	50 ± 63	1399 ± 470
dust devil 5	5.6 ± 6.2	5.1 ± 6.0	100 ± 63	919 ± 471
<i>Arcadia Dorsa / Arcadia Planitia, Image = h1404_0001,</i> <i>L<sub>s</sub> = 163°, LT = 11:10, Lat = 44°N, Lon = 230°E</i>				
dust devil 1	18.0 ± 4.2	18.6 ± 4.7	95 ± 63	226 ± 226
dust devil 2	22.7 ± 4.1	21.9 ± 4.7	253 ± 63	2108 ± 230
<i>Hydraotes Chaos, Image = h2024_0001,</i> <i>L<sub>s</sub> = 267°, LT = 15:44, Lat = 0°S, Lon = 326°E</i>				
dust devil 1	13.1 ± 6.7	19.5 ± 6.6	278 ± 63	467 ± 105
<i>Syria Planum, Image = h2032_0000,</i> <i>L<sub>s</sub> = 269°, LT = 15:30, Lat = 10°S, Lon = 258°E</i>				
dust devil 1	24.6 ± 6.6	22.9 ± 6.2	138 ± 63	2059 ± 138
dust devil 2	16.8 ± 6.6	17.0 ± 6.2	80 ± 63	109 ± 138
<i>Simud Vallis, Image = h2035_0000,</i> <i>L<sub>s</sub> = 269°, LT = 15:34, Lat = 8°N, Lon = 324°E</i>				
dust devil 1	23.1 ± 6.0	24.5 ± 6.3	125 ± 63	327 ± 84
dust devil 2	25.2 ± 6.2	24.8 ± 6.5	115 ± 63	298 ± 90
dust devil 3	31.4 ± 6.3	18.7 ± 6.5	146 ± 63	216 ± 91
dust devil 4	30.9 ± 6.3	-	45 ± 63	75 ± 91
dust devil 5	-	-	372 ± 125	443 ± 191
dust devil 6	27.1 ± 6.4	25.5 ± 6.7	177 ± 63	289 ± 95
dust devil 7	24.6 ± 6.4	16.8 ± 6.6	188 ± 63	237 ± 95
dust devil 8	37.4 ± 6.5	34.8 ± 6.7	160 ± 63	521 ± 96
dust devil 9	22.8 ± 6.5	25.8 ± 6.7	229 ± 63	628 ± 97
dust devil 10	22.4 ± 6.6	26.1 ± 6.8	426 ± 63	-
dust devil 11	26.4 ± 6.9	21.4 ± 6.7	208 ± 63	282 ± 101
dust devil 12	20.1 ± 6.6	21.4 ± 7.0	185 ± 63	606 ± 101
dust devil 13	24.2 ± 6.6	16.8 ± 6.7	80 ± 63	195 ± 101
dust devil 14	17.3 ± 6.6	24.6 ± 6.8	180 ± 63	780 ± 101

Dust Devil Number	S1-ND, m/s	ND-S2, m/s	Diameter, m	Height, m
dust devil 15	26.8 ± 6.7	22.6 ± 6.8	226 ± 63	704 ± 102
dust devil 16	23.3 ± 6.7	25.3 ± 6.8	118 ± 63	384 ± 103
dust devil 17	31.8 ± 6.8	23.1 ± 6.8	80 ± 63	527 ± 103
dust devil 18	47.8 ± 6.8	54.0 ± 6.9	636 ± 63	-
dust devil 19	31.4 ± 6.8	36.3 ± 6.9	186 ± 63	526 ± 105
dust devil 20	41.7 ± 6.6	35.4 ± 6.6	80 ± 63	468 ± 125
<i>Xanthe Dorsa (Chryse Planitia) / Simud Vallis, Image = h2046_0000,</i> <i>L<sub>s</sub> = 271°, LT = 15:25, Lat = 14°N, Lon = 323°E</i>				
dust devil 1	-	59.1 ± 5.8	425 ± 63	-
dust devil 2	-	-	119 ± 63	136 ± 82
dust devil 3	-	31.2 ± 5.8	84 ± 63	147 ± 84
dust devil 4	-	23.9 ± 5.8	289 ± 63	-
dust devil 5	25.1 ± 5.6	27.8 ± 6.0	125 ± 63	369 ± 88
dust devil 6	21.9 ± 5.6	30.3 ± 6.0	106 ± 63	134 ± 89
dust devil 7	31.2 ± 5.6	30.6 ± 6.0	90 ± 63	87 ± 89
dust devil 8	20.9 ± 5.6	-	278 ± 63	729 ± 90
dust devil 9	24.1 ± 5.8	-	151 ± 63	264 ± 93
dust devil 10	21.6 ± 5.8	-	258 ± 63	1744 ± 93
dust devil 11	20.7 ± 5.8	-	113 ± 63	2835 ± 93
<i>Syria Planum, Image = h2054_0000,</i> <i>L<sub>s</sub> = 273°, LT = 15:13, Lat = 10°S, Lon = 258°E</i>				
dust devil 1	43.9 ± 7.2	16.7 ± 6.7	1648 ± 63	4437 ± 156
dust devil 2	19.4 ± 7.0	23.1 ± 6.7	361 ± 63	547 ± 157
dust devil 3	20.1 ± 7.0	16.7 ± 6.7	133 ± 63	1060 ± 157
dust devil 4	18.4 ± 7.0	22.0 ± 6.7	335 ± 63	694 ± 157
dust devil 5	24.0 ± 7.0	24.9 ± 6.7	1433 ± 63	1882 ± 157
<i>Xanthe Terra / Vallis Marineris, Image = h2090_0000,</i> <i>L<sub>s</sub> = 279°, LT = 14:41, Lat = 10°N / -13°S, Lon = 319°E</i>				
dust devil 1	10.8 ± 5.1	22.0 ± 5.6	133 ± 63	331 ± 134
dust devil 2	18.1 ± 5.2	22.1 ± 5.7	106 ± 63	615 ± 134
dust devil 3	15.3 ± 7.0	19.1 ± 6.9	221 ± 63	1503 ± 209
dust devil 4	22.7 ± 6.9	25.0 ± 6.7	186 ± 63	398 ± 224
<i>Peneus Patera, Image = h2100_0000,</i> <i>L<sub>s</sub> = 281°, LT = 14:15, Lat = 57°S, Lon = 56°E</i>				
dust devil 1	11.8 ± 4.4	11.2 ± 3.1	285 ± 125	2665 ± 396
dust devil 2	11.5 ± 5.4	12.1 ± 4.0	280 ± 125	476 ± 439
dust devil 3	13.0 ± 5.2	12.7 ± 3.9	309 ± 125	812 ± 435
dust devil 4	1.5 ± 4.9	2.5 ± 3.6	226 ± 125	122 ± 419
dust devil 5	11.5 ± 4.9	15.0 ± 3.6	351 ± 125	232 ± 421
dust devil 6	10.8 ± 5.6	8.0 ± 4.2	361 ± 125	605 ± 448
dust devil 7	13.6 ± 5.1	11.2 ± 3.8	430 ± 125	1473 ± 431
dust devil 8	14.7 ± 5.1	15.1 ± 3.8	426 ± 125	463 ± 429
dust devil 9	13.3 ± 5.1	12.6 ± 3.8	426 ± 125	497 ± 428
dust devil 10	10.2 ± 4.8	14.6 ± 3.5	354 ± 125	355 ± 416
dust devil 11	-	17.0 ± 3.6	302 ± 125	972 ± 415
dust devil 12	-	7.5 ± 2.8	382 ± 125	412 ± 375
dust devil 13	-	9.3 ± 2.9	301 ± 125	459 ± 382
dust devil 14	7.7 ± 5.3	10.4 ± 4.0	355 ± 125	433 ± 436
dust devil 15	15.3 ± 5.2	13.2 ± 3.9	407 ± 125	665 ± 435
dust devil 16	15.0 ± 5.2	8.4 ± 3.9	318 ± 125	1034 ± 432
dust devil 17	-	12.4 ± 3.8	266 ± 125	809 ± 430
dust devil 18	-	-	195 ± 125	327 ± 406

Dust Devil Number	S1-ND, m/s	ND-S2, m/s	Diameter, m	Height, m
dust devil 19	9.9 ± 4.6	-	305 ± 125	372 ± 405
dust devil 20	8.1 ± 4.1	9.3 ± 2.8	372 ± 125	387 ± 380
dust devil 21	-	-	472 ± 125	562 ± 374
dust devil 22	11.9 ± 4.1	9.8 ± 2.8	340 ± 125	511 ± 378
dust devil 23	14.5 ± 4.1	12.5 ± 2.8	391 ± 125	657 ± 378
dust devil 24	-	5.5 ± 2.8	301 ± 125	210 ± 380
dust devil 25	-	-	247 ± 125	639 ± 374
dust devil 26	11.0 ± 5.2	7.3 ± 3.9	401 ± 125	880 ± 432
<i>Xanthe Terra / Eos Mensa (Valles Marineris), Image = h2101_0000,</i> <i>L<sub>s</sub> = 281°, LT = 14:32, Lat = 8°N / 10°S, Lon = 319°E</i>				
dust devil 1	17.8 ± 4.6	18.9 ± 5.0	98 ± 63	315 ± 131
dust devil 2	12.5 ± 4.4	13.7 ± 5.0	125 ± 63	289 ± 132
dust devil 3	13.3 ± 4.4	16.4 ± 5.0	98 ± 63	563 ± 132
dust devil 4	14.4 ± 4.4	17.9 ± 5.0	157 ± 63	694 ± 132
dust devil 5	14.7 ± 4.4	17.1 ± 5.0	135 ± 63	255 ± 133
dust devil 6	18.9 ± 5.2	21.8 ± 5.7	195 ± 63	1686 ± 150
dust devil 7	19.0 ± 5.6	31.9 ± 6.1	256 ± 63	835 ± 160
dust devil 8	4.0 ± 6.8	2.1 ± 6.9	1008 ± 63	2208 ± 207
dust devil 9	19.1 ± 6.9	14.2 ± 7.1	143 ± 63	705 ± 208
dust devil 10	14.5 ± 7.0	26.2 ± 7.0	654 ± 63	1107 ± 220
dust devil 11	3.9 ± 6.6	6.7 ± 7.1	108 ± 63	383 ± 233
<i>Xanthe Terra / Noachis Terra, Image = h2112_0000,</i> <i>L<sub>s</sub> = 283°, LT = 14:22, Lat = 10°N / 20°S, Lon = 318°E</i>				
dust devil 1	19.3 ± 4.2	17.7 ± 4.8	67 ± 63	174 ± 141
dust devil 2	16.4 ± 4.4	19.5 ± 4.9	174 ± 63	543 ± 147
dust devil 3	18.0 ± 4.4	19.3 ± 5.0	124 ± 63	426 ± 147
dust devil 4	16.3 ± 5.4	19.9 ± 5.8	98 ± 63	183 ± 173
dust devil 5	17.1 ± 5.7	19.4 ± 6.1	138 ± 63	1071 ± 181
dust devil 6	16.4 ± 5.7	23.0 ± 6.2	246 ± 63	1523 ± 184
dust devil 7	13.1 ± 6.7	10.8 ± 6.1	141 ± 63	500 ± 224
dust devil 8	9.6 ± 7.0	14.5 ± 6.7	354 ± 63	1379 ± 279
<i>Peneus Patera, Image = h2133_0000,</i> <i>L<sub>s</sub> = 287°, LT = 13:40, Lat = 58°S, Lon = 53°E</i>				
dust devil 1	22.3 ± 5.8	13.0 ± 4.5	255 ± 125	1322 ± 447
dust devil 2	8.6 ± 5.6	8.7 ± 4.3	202 ± 125	571 ± 438
dust devil 3	12.1 ± 5.5	6.9 ± 4.2	90 ± 125	1352 ± 433
dust devil 4	-	-	250 ± 250	1293 ± 784
dust devil 5	8.8 ± 6.4	7.9 ± 5.1	283 ± 125	1043 ± 479
dust devil 6	19.2 ± 6.2	16.8 ± 4.8	305 ± 125	539 ± 468
<i>Noachis Terra, Image = h2225_0000,</i> <i>L<sub>s</sub> = 302°, LT = 12:30, Lat = 52°S, Lon = 14°E</i>				
dust devil 1	-	12.3 ± 5.1	138 ± 63	1242 ± 283
dust devil 2	-	4.7 ± 4.0	188 ± 63	479 ± 223
dust devil 3	-	5.1 ± 3.8	188 ± 63	263 ± 212
dust devil 4	-	7.0 ± 3.8	138 ± 63	-
dust devil 5	-	3.8 ± 3.8	126 ± 63	228 ± 211
dust devil 6	-	8.7 ± 3.8	175 ± 63	272 ± 212
dust devil 7	-	8.2 ± 4.1	234 ± 63	555 ± 229
dust devil 8	-	8.5 ± 4.1	289 ± 63	998 ± 229
<i>Terra Cimmeria, Image = h2242_0000,</i> <i>L<sub>s</sub> = 305°, LT = 12:20, Lat = 56°S, Lon = 143°E</i>				
dust devil 1	-	5.4 ± 5.6	388 ± 63	912 ± 286

Dust Devil Number	S1-ND, m/s	ND-S2, m/s	Diameter, m	Height, m
dust devil 2	3.9 ± 7.2	2.9 ± 5.7	313 ± 63	1508 ± 289
dust devil 3	6.6 ± 7.2	5.6 ± 5.7	113 ± 63	426 ± 288
dust devil 4	2.1 ± 6.1	3.1 ± 5.6	155 ± 63	383 ± 282
dust devil 5	-	4.5 ± 4.4	143 ± 63	335 ± 282
dust devil 6	-	5.0 ± 5.6	250 ± 63	395 ± 283
dust devil 7	6.4 ± 6.1	10.9 ± 5.5	138 ± 63	302 ± 281
dust devil 8	-	-	126 ± 63	242 ± 280
dust devil 9	-	-	258 ± 63	473 ± 242
dust devil 10	-	-	316 ± 63	1045 ± 241
dust devil 11	-	3.0 ± 4.5	213 ± 63	546 ± 224
dust devil 12	-	4.5 ± 4.3	200 ± 63	477 ± 213
dust devil 13	-	3.7 ± 4.2	127 ± 63	243 ± 210
dust devil 14	-	5.5 ± 4.1	200 ± 63	282 ± 202
dust devil 15	-	6.9 ± 4.1	151 ± 63	319 ± 202
dust devil 16	5.7 ± 4.7	5.6 ± 4.1	198 ± 63	222 ± 201
dust devil 17	-	10.7 ± 4.2	131 ± 63	256 ± 201
dust devil 18	-	5.5 ± 5.0	125 ± 63	322 ± 248
dust devil 19	-	5.1 ± 5.0	168 ± 63	322 ± 248
dust devil 20	-	3.2 ± 5.0	143 ± 63	374 ± 245
dust devil 21	-	5.7 ± 4.0	223 ± 63	267 ± 207
dust devil 22	-	-	195 ± 63	340 ± 244
dust devil 23	3.7 ± 5.5	3.8 ± 4.9	230 ± 63	981 ± 244
dust devil 24	-	2.0 ± 4.9	221 ± 63	301 ± 243
dust devil 25	5.1 ± 5.2	4.4 ± 4.6	170 ± 63	408 ± 226
dust devil 26	8.0 ± 4.8	6.7 ± 4.1	129 ± 63	147 ± 202
<i>Terra Cimmeria, Image = h2315_0000,</i> $L_s = 317^\circ, LT = 11:20, Lat = 57^\circ S, Lon = 170^\circ E$				
dust devil 1	5.4 ± 6.7	-	50 ± 63	145 ± 204
dust devil 2	8.3 ± 6.7	-	163 ± 63	284 ± 204
dust devil 3	8.1 ± 6.7	-	331 ± 63	746 ± 203
dust devil 4	12.7 ± 6.5	-	168 ± 63	295 ± 193
<i>Amazonis Planitia, Image = h3042_0000,</i> $L_s = 57^\circ, LT = 16:25, Lat = 23^\circ N, Lon = 206^\circ E$				
dust devil 1	-	-	151 ± 63	104 ± 101
<i>Xanthe Dorsa (Chryse Planitia), Image = h3202_0000,</i> $L_s = 76^\circ, LT = 14:47, Lat = 19^\circ N, Lon = 323^\circ E$				
dust devil 1	2.3 ± 6.2	2.2 ± 6.0	75 ± 63	580 ± 218
dust devil 2	4.3 ± 6.0	4.4 ± 5.7	118 ± 63	1210 ± 209
dust devil 3	5.1 ± 6.1	3.5 ± 5.8	416 ± 63	1187 ± 215
dust devil 4	2.5 ± 6.2	8.2 ± 6.0	416 ± 63	1324 ± 214
dust devil 5	4.8 ± 6.2	6.3 ± 5.9	319 ± 63	1103 ± 214
<i>Syria Planum, Image = h3210_0000,</i> $L_s = 77^\circ, LT = 14:50, Lat = 10^\circ S, Lon = 257^\circ E$				
dust devil 1	15.9 ± 3.3	16.9 ± 2.6	327 ± 63	1155 ± 129
<i>Xanthe Dorsa (Chryse Planitia), Image = h3246_0000,</i> $L_s = 82^\circ, LT = 14:20, Lat = 17^\circ N, Lon = 317^\circ E$				
dust devil 1	4.3 ± 5.6	3.7 ± 5.2	151 ± 63	993 ± 281
dust devil 2	9.7 ± 5.6	9.8 ± 5.2	146 ± 63	284 ± 280
dust devil 3	7.8 ± 5.6	8.3 ± 5.2	64 ± 63	160 ± 281
dust devil 4	4.7 ± 5.5	6.7 ± 5.1	91 ± 63	243 ± 278
dust devil 5	6.4 ± 5.5	2.3 ± 5.1	143 ± 63	591 ± 278
dust devil 6	7.9 ± 5.5	4.4 ± 5.1	125 ± 63	329 ± 278

Dust Devil Number	S1-ND, m/s	ND-S2, m/s	Diameter, m	Height, m
dust devil 7	15.1± 5.6	8.6± 5.1	222 ± 63	835 ± 277
dust devil 8	6.9± 5.5	2.2± 5.1	125 ± 63	670 ± 277
dust devil 9	6.4± 6.9	6.2± 4.3	302 ± 63	795 ± 280
dust devil 10	8.0± 5.5	8.9± 5.1	248 ± 63	644 ± 275
dust devil 11	2.4± 5.3	4.8± 5.0	108 ± 63	321 ± 275
dust devil 12	5.2± 5.4	8.2± 5.0	202 ± 63	737 ± 274
dust devil 13	7.2± 5.4	8.2± 5.0	219 ± 63	295 ± 274
dust devil 14	5.4± 5.5	7.5± 5.0	115 ± 63	258 ± 274
dust devil 15	6.9± 5.4	4.6± 5.0	135 ± 63	387 ± 273
dust devil 16	8.6± 5.4	7.3± 5.0	266 ± 63	384 ± 273
dust devil 17	3.9± 5.4	5.0± 5.0	178 ± 63	405 ± 273
dust devil 18	2.9± 5.5	6.0± 5.0	223 ± 63	469 ± 274
dust devil 19	2.7± 5.5	5.8± 5.0	146 ± 63	216 ± 274
dust devil 20	5.2± 5.5	5.3± 5.0	71 ± 63	156 ± 274
dust devil 21	3.9± 5.5	6.6± 5.0	101 ± 63	251 ± 273
dust devil 22	-	3.2± 4.9	205 ± 63	389 ± 272
dust devil 23	5.8± 5.4	4.0± 5.0	98 ± 63	219 ± 272
dust devil 24	9.2± 5.4	11.6± 4.9	168 ± 63	463 ± 270
dust devil 25	5.4± 5.4	8.7± 4.9	95 ± 63	135 ± 270
dust devil 26	6.5± 5.4	5.7± 4.9	118 ± 63	361 ± 270
dust devil 27	5.8± 5.4	9.5± 4.9	355 ± 63	666 ± 271
dust devil 28	6.1± 5.4	3.9± 4.9	141 ± 63	288 ± 271
dust devil 29	8.8± 5.4	11.1± 4.9	170 ± 63	302 ± 270
dust devil 30	8.2± 5.4	7.0± 4.9	178 ± 63	260 ± 270
dust devil 31	6.8± 5.2	13.0± 4.7	281 ± 63	889 ± 263
dust devil 32	10.7± 5.0	10.1± 4.5	153 ± 63	236 ± 254
dust devil 33	12.2± 5.0	13.5± 4.4	135 ± 63	238 ± 252
dust devil 34	10.4± 4.9	13.8± 4.4	115 ± 63	176 ± 251
dust devil 35	11.3± 5.7	6.9± 5.3	531 ± 63	2228 ± 283
dust devil 36	0.9± 5.7	4.7± 5.3	203 ± 63	422 ± 283
dust devil 37	5.7± 5.6	5.8± 5.2	141 ± 63	457 ± 280
dust devil 38	8.9± 5.5	5.9± 4.9	143 ± 63	244 ± 276
dust devil 39	1.9± 5.5	4.3± 5.1	141 ± 63	552 ± 276
dust devil 40	6.9± 5.5	4.3± 5.1	186 ± 63	345 ± 276
dust devil 41	13.3± 5.4	7.4± 4.9	125 ± 63	238 ± 267
dust devil 42	7.6± 5.4	3.7± 4.9	106 ± 63	229 ± 269
dust devil 43	8.2± 5.3	6.6± 4.8	186 ± 63	729 ± 267
dust devil 44	10.3± 5.3	7.9± 4.8	221 ± 63	574 ± 266
dust devil 45	9.8± 5.3	10.3± 4.8	168 ± 63	187 ± 265
dust devil 46	9.0± 5.1	10.5± 4.6	141 ± 63	112 ± 260
dust devil 47	9.9± 5.1	12.4± 4.6	160 ± 63	256 ± 260
dust devil 48	10.9± 5.1	11.1± 4.6	151 ± 63	370 ± 259
dust devil 49	6.3± 5.0	6.0± 4.5	292 ± 63	742 ± 256

**Table D.1:** S1 represents the forward looking channel, ND the nadir, and S2 the backward looking channel. LT stands for the local time.

---

## Bibliography

---

- Babalievski, F.**, Cluster counting: The Hoshen-Kopelman algorithm vs. Spanning Tree approaches, *Intern. J. Modern Phys. C*, 9, 43–60, 1998.
- Balme, M. and R. Greeley**, Dust devils on Earth and Mars, *Rev. Geophys.*, 44, RG3003, doi:10.1029/2005RG000188, 2006.
- Balme, M. and A. Hagermann**, Particle lifting at the soil-air interface by atmospheric pressure excursions in dust devils, *Geophys. Res. Lett.*, 33, 2006.
- Balme, M., S. Metzger, M. Towner, T. Ringrose, R. Greeley and J. Iversen**, Friction wind speeds in dust devils: A field study, *Geophys. Res. Lett.*, 30, 1830, doi:10.1029/2003GL017493, 2003a.
- Balme, M. R., P. L. Whelley and R. Greeley**, Mars: Dust devil track survey in Argyre Planitia and Hellas Basin, *J. Geophys. Res.*, 108, 5086, doi:10.1029/2003JE002096, 2003b.
- Barnes, J. R.**, Initiation and spread of Martian dust storms, in *The fifth International Conference on Mars*, abstract #6011, Pasadena, 1999.
- Biener, K. K., P. E. Geissler, A. S. McEwen and C. Leovy**, Observations of dust devils in MOC wide angle camera images, *Lunar. Planet. Sci.*, XXXIII, abstract #2004, 2002.
- Callan, R.**, *Neuronale Netze im Klartext*, Pearson Education Deutschland GmbH, München, 2003.
- Cantor, B. A. and K. S. Edgett**, Martian dust devils: 2 Mars years of MGS MOC observations, *Eos Trans. AGU*, 83(47), Fall Meet. Suppl., F804, 2002.
- Cantor, B. A. and M. Malin**, Mars Orbiter Camera meteorological observations, in *First Workshop on Mars Atmosphere Modelling and Observations*, Granada, Spain, 2003.
- Cantor, B. A., P. B. James, M. Caplinger and M. J. Wolff**, Martian dust storms: 1999 Mars Orbiter Camera observations, *J. Geophys. Res.*, 106(E10), 23653–23688, 2001.

- Cantor, B. A., K. M. Kanak and K. S. Edgett**, Mars Orbiter Camera observations of Martian dust devils and their tracks (September 1997 to January 2006) and evaluation of theoretical vortex models, *J. Geophys. Res.*, *111*, E12002, doi:10.1029/2006JE002700, 2006.
- Carroll, J. J. and J. A. Ryan**, Atmospheric vorticity and dust devil rotation, *J. Geophys. Res.*, *75*, 5179–5184, 1970.
- Chicarro, A., P. Martin and R. Trautner**, The Mars Express Mission: An Overview, in *Mars Express: The Scientific Payload*, edited by A. Wilson, vol. ESA-SP-1240, 3–13, ESA Publications Division, ESTEC, Noordwijk, The Netherlands, 2004.
- Duda, R. O., P. E. Hart and D. G. Stork**, *Pattern Classification (Second Edition)*, John Wiley & Sons, New York, 2001.
- Duxbury, E. and D. Jensen**, VICAR USER'S GUIDE, (<http://www-mipl.jpl.nasa.gov/PAG/public/vug/vugfinal.html>), technical report, Jet Propulsion Laboratory, California Institute of Technology, Pasadena, California, 1994.
- Farrell, W. M. et al.**, Electric and magnetic signatures of dust devils from the 2000-2001 MATADOR desert tests, *J. Geophys. Res.*, *109*, E03004, doi:10.1029/2003JE002088, 2004.
- Farrell, W. M., J. R. Marshall, S. A. Cummer, G. T. Delory and M. D. Desch**, A model of the ULF magnetic and electric field generated from a dust devil, *J. Geophys. Res.*, *111*, E11004, doi:10.1029/2006JE002689, 2006a.
- Farrell, W. M., N. Renno, G. T. Delory, S. A. Cummer and J. R. Marshall**, Integration of electrostatic and fluid dynamics within a dust devil, *J. Geophys. Res.*, *111*, E01006, doi:10.1029/2005JE002527, 2006b.
- Ferri, F., P. H. Smith, M. Lemmon and N. Rennó**, Dust devils as observed by Mars Pathfinder, *J. Geophys. Res.*, *108*, 5133, doi:10.1029/2000JE001421, 2003.
- Fiedler, B. H. and K. M. Kanak**, Rayleigh-Bénard convection as a tool for studying dust devil formation, *Atmos. Sci. Lett.*, doi:10.1006/asle.2001.0043, 2001.
- Fisher, J. A., M. I. Richardson, C. E. Newman, M. A. Szwast, C. Graf, S. Basu, S. P. Ewald, A. D. Toigo and R. J. Wilson**, A survey of Martian dust devil activity using Mars Global Surveyor Mars Orbiter Camera images, *J. Geophys. Res.*, *110*, E03004, doi:10.1029/2003JE002165, 2005.
- Gibbons, A., F. Yang, P. Mlsna and P. Geissler**, Automated Procedures for Detecting Martian Dust Devils, *Lunar Planet. Sci.*, XXXVI, abstract #2005, 2005.
- Gierasch, P. and R. M. Goody**, A model of a Martian great dust storm, *J. Atmosph. Sci.*, *30*, 749–762, 1973.
- Golombek, M. P. et al.**, Overview of the Mars Pathfinder Mission: Launch through Landing, Surface Operations, Data Sets, and Science Results, *J. Geophys. Res.*, *104*, 8523–8553, 1999.

- Greeley, R. and J. D. Iversen** (Eds.), *Wind as a Geologic Process on Earth, Mars, Venus and Titan*, Cambridge Univ. Press, Cambridge, UK, 1985.
- Greeley, R., B. White, J. B. Pollack, J. Iversen and R. N. Leach**, Dust storms on Mars: Considerations and simulations, in *Desert Dust: Origin, Characteristics, and Effect on Man*, edited by T. Péwé, 101–121, Spec. Paper Geol. Soc. Am., 186, 1981.
- Greeley, R., N. Lancaster, S. Lee and P. Thomas**, Martian aeolian processes, sediments, and features, in *Mars*, edited by H. H. Kieffer, B. M. Jakosky, C. W. Snyder, and M. S. Matthews, 730–766, Univ. of Arizona Press, Tucson, 1992.
- Greeley, R., M. R. Balme, J. D. Iversen, S. Metzger, R. Mickelson, J. Phoreman and B. White**, Martian dust devils: Laboratory simulations of particle threshold, *J. Geophys. Res.*, 108, 5041, doi:10.1029/2002JE001987, 2003.
- Greeley, R., P. L. Whelley and L. D. V. Neakrase**, Martian dust devils: Directions of movement inferred from their tracks, *Geophys. Res. Lett.*, 31, L24702, doi:10.1029/2004GL021599, 2004.
- Greeley, R. et al.**, Active dust devils in Gusev Crater, Mars: Observations from the Mars Exploration Rover, Spirit, *J. Geophys. Res.*, 111, E12S09, doi:10.1029/2006JE002743, 2006.
- Hoshen, J. and R. Kopelman**, Percolation and cluster distribution. I. Cluster multiple labeling technique and critical concentration algorithm, *Phys. Rev. B*, 14, 3438–3445, 1976.
- Hoshen, J., M. W. Berry and K. S. Minser**, Percolation and cluster structure parameters: The enhanced Hoshen-Kopelman algorithm, *Phys. Rev. E*, 56, 1455–1460, 1976.
- Ives, R. L.**, Behavior of Dust Devils, *Bull. Am. Meteorol. Soc.*, 28, 1947.
- Kanak, K. M.**, Numerical simulation of dust devil-scale vortices, *Q. J. R. Meteorol. Soc.*, 131, 1271–1292, 2005a.
- Kanak, K. M.**, Numerical simulation of dust devil-like vortices in the terrestrial and Martian convective boundary layers, in *Workshop on Dust Devils: Earth and Mars*, Ariz. State Univ., Planet. Geol. Group, Flagstaff, 2005b.
- Kanak, K. M.**, On the numerical simulation of dust devil-like vortices in terrestrial and Martian convective boundary layers, *Geophys. Res. Lett.*, 33, L19S05, doi:10.1029/2006GL026207, 2006.
- Kanak, K. M., D. K. Lilly and J. T. Snow**, The formation of vertical vortices in the convective boundary layer, *Q. J. R. Meteorol. Soc.*, 126, 2789–2810, 2000.
- Kieffer, H. H., B. M. Jakosky, C. W. Snyder and M. S. Matthews** (Eds.), *Mars*, Univ. of Arizona Press, Tucson, 1992.
- Kukulich, L. and R. P. Lippmann**, LNKnet User's Guide, *MIT Lincoln Laboratory*, 2004.

- Larsen, S. E., H. E. Jørgensen, L. Landberg and J. E. Tillman**, Aspects of the atmospheric surface layers on Mars and Earth, *Boundary-Layer Meteorol.*, *105*, 451–470, 2002.
- Lee, Y.**, Classifiers: Adaptive Modules in Pattern Recognition Systems, Master's Thesis, Massachusetts Institute of Technology, Lexington, 1989.
- Lewis, S. R., M. Collins, P. L. Read, F. Forget, F. Hourdin, R. Fournier, C. Hourdin, O. Talagrand and J. Huot**, A climate database for Mars, *J. Geophys. Res.*, *104*, 24177–24194, 1999.
- Lippmann, R. P., L. Kukolich and E. Singer**, LNKnet: Neural Network, Machine Learning, and Statistical Software for Pattern Classification, *Lincoln Laboratory Journal*, *6*, 249–268, 1993.
- Malin, M. C. and K. S. Edgett**, Mars Global Surveyor Mars Orbiter Camera: Interplanetary cruise through primary mission, *J. Geophys. Res.*, *106*, 23429–23570, 2001.
- Malin, M. C., K. S. Edgett, S. D. Davis, M. A. Caplinger, E. Jensen, K. D. Supulver, J. Sandoval, L. Posiolova and R. Zimdar**, Image ID E14-00318, Malin Space Science Systems Mars Orbiter Camera Image Gallery ([http://www.msss.com/moc\\_gallery/](http://www.msss.com/moc_gallery/)), 4. April 2003, 2003.
- McGinnigle, J. B.**, Dust whirls in north-west Libya, *Weather*, *21*, 272–276, 1966.
- Metzger, S. M.**, Dust devils as aeolian transport mechanisms in southern Nevada and in the Mars Pathfinder landing site, Ph.D. Thesis, Univ. of Nev., Reno, 1999.
- Metzger, S. M.**, Promoting a well-established study site for Mars analog and desert process studies, *Lunar Planet. Sci.*, *XXXIV*, abstract #2048, 2003.
- Metzger, S. M., J. R. Carr, J. R. Johnson, T. J. Parker and M. T. Lemmon**, Dust devil vortices seen by the Mars Pathfinder camera, *Geophys. Res. Lett.*, *26*, 2781–2784, 1999.
- Michaels, T. I. and S. C. R. Rafkin**, Large eddy simulation of atmospheric convection on Mars, *Q. J. R. Meteorol. Soc.*, *130*, 1251–1275, 2004.
- Monin, A. S. and A. M. Obukhov**, Basic laws of turbulent mixing in the atmosphere near the ground, *Trudy Akademii Nauk SSSR*, *24*, 1963–1987, 1954.
- Määttänen, A. and H. Savijärvi**, Sensitivity tests with a one-dimensional boundary-layer Mars model, *Boundary-Layer Meteorol.*, *113*, 305–320, 2004.
- Neakrase, L. D. V., R. Greeley, J. D. Iversen, M. R. Balme and E. E. Eddlemon**, Dust flux within dust devils: Preliminary laboratory simulations, *Geophys. Res. Lett.*, *33*, L19S09, doi:10.1029/2006GL026810, 2006.
- Neubauer, F. M.**, Thermal convection in the Martian atmosphere, *J. Geophys. Res.*, *71*, 2419–2426, 1966.

- Neukum, G., R. Jaumann and the HRSC Co-Investigator and Experiment Team**, HRSC on the Mars Express Orbiter, Part I, Scientific and Technical Plan, *Proposal in Response to ESA Announcement of Opportunity ESA/SCI(97)3*, 1998.
- Neukum, G., R. Jaumann and the HRSC Co-Investigator and Experiment Team**, HRSC: the High Resolution Stereo Camera of Mars Express, in *Mars Express: The Scientific Payload*, edited by A. Wilson, vol. ESA-SP-1240, 17–35, ESA Publications Division, ESTEC, Noordwijk, The Netherlands, 2004.
- Pollack, J. B., D. S. Colburn, F. M. Flasar, R. Kahn, C. E. Carlston and D. Pidek**, Properties and effects of dust particles suspended in the Martian atmosphere, *J. Geophys. Res.*, *84*, 2929–2945, 1979.
- Rafkin, S. C. R., R. M. Haberle and T. I. Michaels**, The Mars regional atmospheric modeling system: Model description and selected simulations, *Icarus*, *151*, 228–256, 2001.
- Rennó, N. O. and H. B. Bluestein**, A simple theory for waterspouts, *J. Atmosph. Sci.*, *58*, 927–932, 2001.
- Rennó, N. O., M. L. Burkett and M. P. Larkin**, A simple thermodynamical theory for dust devils, *J. Atmosph. Sci.*, *55*, 3244–3252, 1998.
- Rennó, N. O., A. A. Nash, J. Lunine and J. Murphy**, Martian and terrestrial dust devils: Test of a scaling theory using Pathfinder data, *J. Geophys. Res.*, *105*, 1859–1865, 2000.
- Ringrose, T. J., M. C. Towner and J. C. Zarnecki**, Convective vortices on Mars: A reanalysis of Viking Lander 2 meteorological data, sols 1-60, *Icarus*, *163*, 78–87, 2003.
- Rossi, A. P. and L. Marinangeli**, The first terrestrial analogue to martian dust devil tracks found in Ténéré Desert, Niger, *Geophys. Res. Lett.*, *31*, L06702, doi:10.1029/2004GL019428, 2004.
- Rover Team**, Characterization of the Martian surface deposits by the Mars Pathfinder rover, Sojourner, *Science*, *278*, 1765–1767, 1997.
- Ryan, J. A.**, Notes on the Martian yellow clouds, *J. Geophys. Res.*, *69*, 3759–3770, 1964.
- Ryan, J. A.**, Relation of Dust Devil Frequency and Diameter to Atmospheric Temperature, *J. Geophys. Res.*, *77*, 7133–7137, 1972.
- Ryan, J. A. and J. J. Carroll**, Dust devil wind velocities: Mature state, *J. Geophys. Res.*, *75*, 531–541, 1970.
- Ryan, J. A. and R. D. Lucich**, Possible dust devils, vortices on Mars, *J. Geophys. Res.*, *88*, 11005–11011, 1983.
- Ryan, J. A., R. D. Sharman and R. D. Lucich**, Local Mars dust storm generation mechanism, *Geophys. Res. Lett.*, *8*, 899, 1981.

- Schofield, J. T., J. R. Barnes, D. Crisp, R. M. Haberle, S. Larsen, J. A. Magalhães, J. R. Murphy, A. Seiff and G. Wilson**, The Mars pathfinder Atmospheric Structure Investigation/Meteorology (ASI/MET) Experiment, *Science*, 278, 1752–1758, 1997.
- Sinclair, P. C.**, General Characteristics of Dust Devils, *J. Appl. Meteorol.*, 8, 32–45, 1969.
- Sinclair, P. C.**, The lower structure of dust devils, *J. Atmosph. Sci.*, 30, 1599–1619, 1973.
- Snow, J. T. and T. M. McClelland**, Dust devils at White Sands Missile Range, New Mexico: 1. Temporal and Spatial Distributions, *J. Geophys. Res.*, 95, 13707–13721, 1990.
- Stanzel, C., M. Pätzold, R. Greeley, E. Hauber and G. Neukum**, Dust devils on Mars observed by the High Resolution Stereo Camera, *Geophys. Res. Lett.*, 33, L11202, doi:10.1029/2006GL025816, 2006.
- Stanzel, C., M. Pätzold, D. A. Williams, P. L. Whelley, R. Greeley and G. Neukum**, Comparison of Martian dust devils characteristics observed by the Mars Express High Resolution Stereo Camera and the Mars Exploration Rover Spirit, *Icarus*, submitted, 2007.
- Thomas, P. C. and P. J. Gierasch**, Dust devils on Mars, *Science*, 230, 175–177, 1985.
- Tillman, J. E., L. Landberg and S. E. Larsen**, The boundary layer of Mars: Fluxes, stability, turbulent spectra, and growth of the mixed layer, *J. Atmosph. Sci.*, 51, 1709–1727, 1994.
- Toigo, A. D., M. I. Richardson, S. P. Ewald and P. J. Gierasch**, Numerical simulation of Martian dust devils, *J. Geophys. Res.*, 108, 5047, doi:10.1029/2002JE002002, 2003.
- Wennmacher, A., F. M. Neubauer, M. Pätzold, J. Schmitt and K. Schulte**, A search for dust devils on Mars, *Lunar Planet. Sci.*, 27, 1417, 1996.
- Whelley, P. L.**, Personal communication, 2007.
- Whelley, P. L. and R. Greeley**, Latitudinal dependency in dust devil activity on Mars, *J. Geophys. Res.*, 111, E10003, doi:10.1029/2006JE002677, 2006.
- Williams, D. A.**, Personal communication, 2007.
- Zabel, T.**, Klassifikation mit Neuronalen Netzen, in *Advances in Information Systems and Management Science*, edited by J. Becker, H. L. Grob, S. Klein, H. Kuchen, U. Müller-Funk, and G. Vossen, vol. 16, Logos Verlag, Berlin, 2005.
- Zurek, R. W., J. R. Barnes, R. M. Haberle, J. B. Pollack, J. E. Tillman and C. B. Leovy**, Dynamics of the atmosphere of Mars, in *Mars*, edited by H. H. Kieffer, B. M. Jakosky, C. W. Snyder, and M. S. Matthews, 835–933, Univ. of Arizona Press, Tucson, 1992.

# Acknowledgements

First of all, I would like to thank PD Dr. Martin Pätzold who gave me the opportunity to work 'on Mars'. Analysing atmospheric features by studying 'brand-new' images from Mars and presenting the results at international conferences was very exciting and I learnt a lot through the last years.

Furthermore, I want to thank Prof. Dr. Michael Kerschgens who kindly agreed to be a reviewer for this work.

The team 'Radio Science', formerly at the Institute of Geophysics and Meteorology, now at the Rhenish Institute of Environmental Research, contributed to this work in fruitful discussions, fair comments, and an easy working ambience where now and then a keg of 'Kölsch' supported all this. This includes also people who left the team in the mean time.

Gratitude has to be expressed to all colleagues at the Institute of Geophysics and Meteorology who helped either on the technical or on the scientific side to prepare this work.

Special thanks to Thomas Roatsch, Frank Scholten, Klaus-Dieter Matz and Ernst Hauber from DLR Berlin. Without their help it would have taken much longer to get to know to HRSC images and to answer arising questions during image processing and analysing. Thanks to all members of the HRSC Team as well, in particular to David Williams and Ronald Greeley, for discussions and support of my work. Thanks are given to Boris Semenov for preparing the VIKING kernels.

I acknowledge the funding of the DFG, Deutsche Forschungsgemeinschaft, Bonn, under grant PA 525/4-1, PA 525/4-2 and PA 525/4-3, within the scope of the priority program SPP 1115 'Mars and the Terrestrial Planets'.

I want to thank Silvia Tellmann, Tetsuya Tokano and Alexandra Helbing for proof-reading the draft of this work.

Thanks to the multi-purpose work out possibilities at the University of Cologne which prevented me to get rusty and keep a level head. I am grateful to Katrin Koch and Karin Kobecke for encouraging talks before, during and after the exercises.

My deepest gratitude is directed to all my friends and family: especially to my parents Hannelore and Hans Stanzel, my sister Carolin, Markus Reck and Kaori Miura who helped and supported me during all the years.



# Erklärung

Ich versichere, dass ich die von mir vorgelegte Dissertation selbständig angefertigt, die benutzten Quellen und Hilfsmittel vollständig angegeben und die Stellen der Arbeit - einschließlich Tabellen, Karten und Abbildungen -, die anderen Werken im Wortlaut oder dem Sinn nach entnommen sind, in jedem Einzelfall als Entlehnung kenntlich gemacht habe; dass diese Dissertation noch keiner anderen Fakultät oder Universität zur Prüfung vorgelegen hat; dass sie - abgesehen von unten angegebenen Teilpublikationen - noch nicht veröffentlicht worden ist sowie, dass ich eine solche Veröffentlichung vor Abschluss des Promotionsverfahrens nicht vornehmen werde. Die Bestimmungen der Promotionsordnung sind mir bekannt. Die von mir vorgelegte Dissertation ist von Priv.-Doz. Dr. Martin Pätzold betreut worden.

## Teilpublikationen

**Stanzel, C., M. Pätzold, R. Greeley, E. Hauber and G. Neukum**, Dust devils on Mars observed by the High Resolution Stereo Camera, *Geophys. Res. Lett.*, 33, L11202, doi:10.1029/2006GL025816, 2006.

**Stanzel, C., M. Pätzold, D. A. Williams, P. L. Whelley, R. Greeley and G. Neukum**, Comparison of Martian dust devils characteristics observed by the Mars Express High Resolution Stereo Camera and the Mars Exploration Rover Spirit, submitted to *Icarus*, 2007.

